NTNU – Trondheim
Norwegian University of
Science and Technology

Interplay of Mass Detrainment and the Braking Effect of Forests on Small-to-Medium Size Avalanches

An Experimental Study

Christopher Wear

MASTER'S THESIS

January 2018

Supervisor: Steinar Nordal
Co-supervisor: Dieter Issler, NGI

Department of Civil and Environmental Engineering
Norwegian University of Science and Technology (NTNU)

Preface

This master's thesis is part of the *MSc Geotechnics and Geohazards*, hosted by the department of *Civil and Environmental Engineering* at the *Norwegian University of Science and Technology*. It was written in the fall semester 2017 following the literature review 'The Braking Effect of Trees on Snow Avalanches', which was a prequal to this master's thesis. The project was proposed by Dieter Issler, NGI, and published in NTNU's database of project proposals.

Christopher Wear Trondheim, 2018-01-25

Acknowledgment

I would like to thank the Steinar Nordal for his great help and recommendation throughout the literature review. Steinar has become NTNU's official supervisor where his role as of thus far is mainly administrative components. Also, Dieter Issler deserves a thanks for taking time out of his schedule to provide informative correspondence. I would also like to thank the NTNU staff at the library for their help in retrieving important documents that proved to be very useful for this literature review. Many of the technicians within the Geotechnical department provided me with the necessary tools to fabricate the model. With their knowledge and carpentry background, I was able to complete building the model with minimal setbacks. I would also like to thank NTNU for financing this project in full.

(C.W.)

Summary and Conclusions

Small-scale testing was conducted on a laboratory avalanche model built to quantify the deceleration of avalanches flowing through alpine forests. The inclination of the chute is given as 35°, the inclination of the runout section as 10°. Two materials were tested with regard to avalanche representativity: alumina powder and ballotini. Four parameters were varied: relative humidity, material type, tree density, and front/surface velocity. A total amount of 62 experiment runs were executed, of which 48 were successful. The latter include 28 test runs with forest and 20 reference test runs without forest. Avalanches modeled with both materials showed deceleration when traveling through the forest. The most significant cause of this deceleration was determined to be the loss of mass. It was observed that the ballotini move approximately twice as fast as alumina powder, during both reference trials and forested trails. Avalanches modeled with ballotini reached a farther run out distances - approximately 45cm for reference trials and 10-15cm for forested trials- then the avalanches modeled with alumina powder. Humidity was found as the major control factor for avalanche behavior. A relative humidity of approximately 65% was determined as recommended for this experimental set-up. Grouping of trees had the largest effect on the avalanche volume release, producing the largest deceleration effect within this experimental study. Avalanche rheology was found to be greatly influenced by alternating forest densities. It can be concluded that alumina powder does best represent wet avalanches, whereas ballotini are more representative for dry avalanches.

List of Figures

List of Tables

Contents

Chapter 1

Introduction

In order to determine the influence trees have on resisting avalanche flow, one must be aware of the altering characteristics of snow, specifically the rheology of snow avalanches since an avalanche is essentially the sudden descent of a large mass of material; snow, ice, rock or soil, down the slope of a mountain. The trigger of such ice particles gliding down-slope is generally due to a rapid change in temperature, earthen vibrations or the most commonly observed is via heavy snowfall with extreme wind creating uneven distribution of snowpack. The rapid accumulation overloads the underlying snowpack activating the weaker layer beneath the slab to fracture.

It is relevant to view these layers as an archive of altering winter weather: Massive accumulation, drought, rain, a hard freeze, thaw and more snow. The way in which these layers bond often determines snow mass quality and probability of a slide. Within these characteristics, material will eventually break loose from its surroundings and cause crowning propagation to occur. After the initial trigger, material quickly collects and accretes greater snow mass over time. Such occurrences become more frequent when multiple weakness zones are prevalent. The triggering mechanisms of snow avalanches are sporadic at times but understanding such characteristics can provide insight into the magnitude and severity of certain avalanches and thereby performance of protection forests.

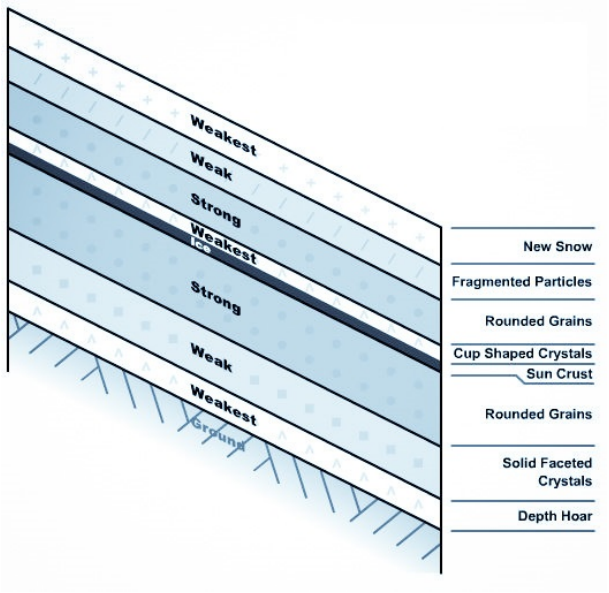

Figure 1.1: Relationship between layers of various strengths and snowpack characteristics. National Avalanche Center (nd)

In the last 10 years alone, 2006 – 2016, 362 fatalities have been counted in the United States alone, that is an average of 33 per year (Colorado Avalanche Information Center, 2016). Although primarily human caused, they can still induce road and railway closure, destruction to infrastructures such as power lines and irreparable damage to the natural environment. In some mountain communities, excavation of avalanche deposition is of up-most importance since road closure can isolate the community from transport of essential resources. Though snow avalanches pummeling into structures are infrequent, they have killed 5 people in Norway over the last 10 years nonetheless.

Table 1.1: Canadian Snow Avalanche Size-Classification System((McClung and Schweizer, 2006)

Size	Description	Mass	Length	Impact pressure
1	Relatively harmless to humans	$< 10_t$	10m	1kPa
2	Could bury, injure or kill a person	10_t^2	100m	10kPa
3	Could bury a car, destroy a small building, break trees	10_t^3	1000m	100kPa
4	Could destroy a railroad buildings, or forest area up to 4 hectares	10_t^4	2000m0	500kPa
5	Could destroy a village or forest area of 40 hectares	10_t^5	30000m	1000kPa

1.1 Background

The illusive braking effect of trees on avalanches appear numerous times without undeniable resolve. The question remains: is the braking action of forest determined by a given forest density or governed by the magnitude of the slide. And conversely, predicted damage to the forest with respect to altering slide characteristics? Previous simulations at NTNU emphasized numerical model of avalanches sliding through forest with altering density. Is it necessary to change the models to simulate the effects of forest, or is it enough to modify friction parameters? If so, is it necessary to change such parameters depending on the number of trees per unit area, average tree diameter or both? If the trees are widely spaced, one can find the answer from the opposition of a single tree and number of trees per unit area, but this is of little practical significance. If the forest is dense, affecting the disturbance of the flow from a tree also flow around neighboring trees and the effect cannot be calculated in a simple way.

The first part of this project is characterized by an in-depth literature study of the snow detrainment method compared with the classic Voellmy friction parameters. The second part focuses on simple laboratory experiments of a fine-grained material sliding down a glide path, about the scale of $1:50-1:200$. This model will have multiple simulations: Forest density and tree width are simulated for instance by attaching poles onto the slide path at increasing density and thickness. These poles are inserted over a certain length at one-half of the slide path while the other model will have no obstacles down the slide path. An in depth analysis between the change in velocity will ascertain the sought after braking effect of trees on avalanches. However, another aspect is to change the material type from Ballotini to a dry powder in effort of simulating actual snow conditions and deposition rates. Reason being, Ballotini is non-cohesive relating only to dry-snow avalanches. In dry-snow avalanches, the deposited snow may also be somewhat damp, either because of energy dissipation through friction and collisions or because humid snow was entrained in the lower part of the path Issler (2003).

In addition, energy loss or the force exerted by a single tree is approximated if one can find a suitable definition of the Reynolds number for granular and viscoplastic media. Provided with a reliable friction coefficient (or detrainment rate), it would then be possible to acquire comparative results when up-scaling the model to natural avalanches. The project model in its entirety can use these experimental results to customize the parameters of one or a few selected dynamic models.

1.2 Protection Forests

This section is mainly based on The role of forests in reducing hydrogeomorphic hazards by providing insightful information of real world situations proceeding with the impact forested terrain has on snow avalanche mitigation. “Forests offer protection from hydrogeomorphic hazards in two broad ways Motta and Haudemand (2000): Indirect protection refers to the general role of forests in improving watershed condition and direct protection specifically protect people, buildings, or utility corridors. For episodic hydrogeomorphic hazards, protection forests of both varieties are an attractive measure due to their risk reduction services and relatively low costs Schönenberger and Brang (2004). Designation of thinning the forest in order to make room for new growth is a cheaper method than other direct protection methods. Appropriate management of protection forests protect residents by reducing potential release areas and/or decelerate an avalanche’s momentum.

1.2.1 Protection Forest Management

Land managers using protection forests may accumulate substantial savings compared to engineered structures, even if intensive forest management is required (Brang, 2001). Protection forests may not prevent hydrogeomorphic events from occurring, but possibly decrease their effects even for very large events (Sakals et al., 2006). Forest managers underestimate tree grouping being a positive attribute to overall braking effect of avalanches.

There are two main factors that prove to be problematic for maintaining a robust protection forest. First, if the forest is even-aged, i.e. the size and strength of the trees are analogous, the protective capacity may be reaching a maximum; however, the resilience will be nearing a minimum. Such a narrow distribution should be expected to result in a temporally fluctuating level of protection similar to that of solitary trees. Second, as trees get old they begin to perish. Although decaying trees have both protective and ecological functions, the protectiveness is abridged relative to healthy trees, particularly over time (Schönenberger et al., 2005).

Figure 1.2: Protection forest support in effort to limit avalanche initiating within the trigger zone. Fences such as this are installed to enhance forest ecology through avalanche prone terrain. (Schild, 2006),(Jan, 2010)

Forests can reduce hydrogeomorphic hazards by retaining material in up-slope positions along with limiting the extent of such disturbances (Sakals et al., 2006), Figure 1.2. In order to analyze the braking effect of trees on avalanches, one must acknowledge the protective functions affecting both surface and subsurface processes. The above-ground hydrogeomorphic functions relate to the physical structure of the forest include: an augmented surface roughness can undoubtedly decrease the initiation and momentum of snow avalanches through a variety of processes. Tree trunks, both upright and downed, reduce the areas disturbed by snow avalanches, rockfalls, floods, debris floods and debris flows (Sakals et al., 2006).

The most important aspect of the protection function is undoubtedly the actual physical structure of the timberland above ground, although groundwater hydrogeology interacting with the root system does plays a large role in forest rigidity by; allowing for rapid subsurface drainage in order to avoid high pore water pressures along with increasing stability by vegetation roots binding the cohesive soil mass and anchoring the soil to the bedrock. If the protection service is desired for the long-term, the management of the forest must be sensitive to the age distribution of the forest as it affects the rapidity of protective function recovery after disturbance. Given the expected magnitude-frequency relations of many hydrogeomorphic hazards, protection forests are an attractive solution for aesthetics, economics, safety and sustainability (Sakals et al., 2006)).

1.2.2 Active Mitigation

Particularly where climates tend to generate wet snow avalanches. recurrent avalanches are often and become the primary hazard for roads, railways and ski-runs (Gruber and Bartelt, 2007). Local authorities must deal with the risk of small-to-medium avalanches striking infrastructure numerous times during a winter season making forests an important protective measure (Teich et al., 2012). Henceforth, the grave desire to quantify the braking effect of forests on small-to-medium avalanches (Teich et al., 2012). In this case, trees remain upright after avalanche impact and have the strength to withstand overbearing dynamic stresses and thus work as effective obstacles to decelerate the flow. The effect is similar to avalanche dams (Naaim et al., 2004); however, the working mechanism differs because the forest is not a single, rigid man-made defense structure, but a natural and inhomogeneous array of slender obstacles (trees, tree groups). If the trees are not broken or uprooted, forest structure (stem density, gaps, crown coverage, age and low-lying vegetation) is of crucial importance (Feistl

et al., 2014). Below are a variations of active measures taken by communities that are subject to extreme snow avalanches with an environment that cannot sustain alpine timberland:

Figure 1.3: Conical earth mounds forming a barracade around Flateyri, a fishing vilage in the north-west of Iceland that suffered from a tragic avalanche event in October 1995 that resulted in twenty fatalities.

(SATSIE, 2003)

Figure 1.4: In 1974, Neskaupstadur damaged by a catastrophic avalanche so the settlement is now protected by a huge catching dam and cones. The maximum height is around 17 m. The photo shows the cones and catching dam below Drangagil. (Photo: The Icelandic Meteorological Office, IMO). Due to the height, most large dams in Iceland are made from "reinforcement material" on the impact side so that they can stand at a very steep angle.

(Hestnes, nd)

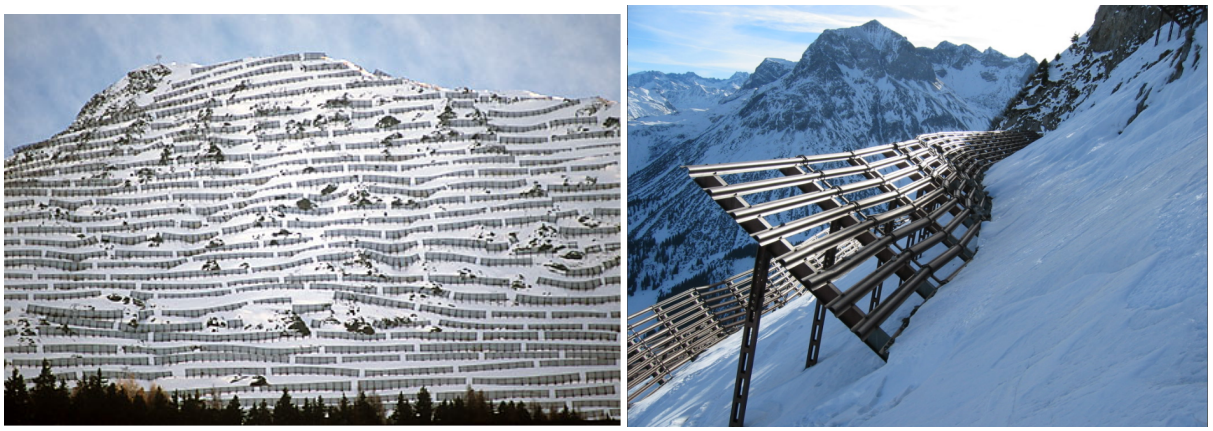

Figure 1.5: Fencing support is built in Austria determined to limit avalanche establishing within the trigger zone.

(Relweger, 2005)

1.3 Deterministic Evaluation of Braking Effect of Trees

There is an abundance of prevailing forest avalanche data that encompass material with esteemed observational content, particularly concerning the effect of dissimilar forest structures inhibiting avalanche development Viglietti et al. (2010). In spite of this, evidence on forest structure and avalanche rheology, such as avalanche magnitude and deposition patterns, is limited and normally centered around the extreme avalanche case Takeuchi et al. (2011). With this in mind, the primary goal of this research was to simulate observed real world events. In order to properly model snow avalanche flow through timberland, comprehension of the manner in which trees halt avalanches is the first obstacle. The focus of Feistl's data assortment was to document characteristics of release areas and fracture depths, snow conditions, forest structure, flow perimeter and deposition patterns Feistl et al. (2014).

Based on Christen's observations, a detrainment function was established that represents interactions of an avalanche flowing through forest which is to be utilized within the framework of a depth-averaged avalanche dynamics model Christen et al. (2001). In this study, snow characteristics are classified according to qualitative criteria, such as dry, moist and wet, based on input from meteorological data of nearest weather station. The meteorological conditions prior to the event, and therefore the causes of the avalanches, differed, resulting in wet snow avalanches as well as dry snow avalanches. Through a combination of observed snow behavior, it is possible to infer that trees do in fact stop flowing snow by the following processes: "impact followed by jamming, resulting in a sudden and local dissipation of flow energy behind trees or tree groups. We address avalanche/forest interactions by specifying snow detrainment rates, rather than using higher friction values to represent the highly nonlinear braking effect of trees" Feistl et al. (2014).

Numerous authors have used the friction approach with respect to Voellmy-type models, but this context seems to be representative for just extreme avalanches where the braking effects are minor and occur over longer flow distances. "For the small-avalanche case, Voellmy-type relations represent the avalanche/forest interaction poorly" Teich et al. (2012). In principle, the detrainment approach is parametrized by a single coefficient which represents the braking power of the forest. It is undeniable that both the friction and detrainment approach have the same desired result of explicating snow mass deceleration along with quantifying the mass stopped by trees; however, the detrainment approach is more straight

forward in the sense that mass is removed from the avalanche volume and thereby momentum directly from the flow instead of indirectly by friction coefficients. This method is more practical for smaller scale avalanches since detrainment principle provides a before-and-after scenario based on the total mass per unit area immobilized by the forest. In order to demonstrate the detrainment approach's reliability as well as its limitations, Feistl and his team applied this approach on seven case studies where they calculated deposition volumes and then compared them with field observations.

Literature Survey

Understanding exactly how forests decelerate avalanches has been an enduring problem since the 1930s.The contents of the Theory chapter is based primarily on (Feistl et al., 2014) for it goes into depth on 'Observations and modeling of the braking effect of forests on small and medium avalanches'. As mentioned before, the detrainment approach, which is grounded on momentum extraction, seemed to be more reliable in comparison to the friction approach, which is functions on modified friction coefficients. A large majority of gathered material was pulled from Annals of Glaciology archive, for that provided the most in depth and up to date literature. However, "The Technical Avalanche Protection Handbook" was very beneficial with its in depth knowledge on avalanche mitigation. Christen also provided outstanding material on numerical methods from his literature on 'RAMMS: Numerical simulation of dense snow avalanches in three-dimensional terrain' which is from "gold Regions Science and Technology" (Brang, 2001) define a protection forest to be "a forest that has as its primary function the protection of people or assets against the impacts of natural hazards or adverse climate" and explains the benefit of managing such structues as protective measures. In a field campaign in northern Sweden, Breien and Høydal (2014) study how birch forests stabilize the snow pack in avalanche starting zones. They find that in the forested area, there are no persistent weak layers, homogeneous layers are undulating, bent, or broken, and the surrounding snow is anchored to tree stems and low-lying branches by ice. (Teich et al., 2012) provided insightful information on "Snow Avalanches in Forested Terrain: Influence of Forest Parameters, Topography, and Avalanche Characteristics on Runout Distance." for which was published in Arctic Antarctic and Alpine Research.

What Remains to be Done?

First, it is unfortunate that the detrainment approach is only legitimate for small-to-medium avalanches where trees are not destroyed and instead act as rigid obstacles; therefore, the model is restricted to certain cases where no entangled mass is stopped, does not account for momentum gains or increased destruction throughout the forest. The application of the model is therefore restricted to a specific flow case. Second, it is apparent that the models outcomes are sensitive to the range of initial avalanche mass and snow characteristics, so back-calculating is problematic. Further field investigation and attainment of data sets is the only viable way to characterize the K value with up-most confidence. To support the fieldwork previously carried out, small-scale granular chute experiments should be carried out to explore how detrainment in forest-like structures modifies momentum and energy fluxes of avalanches. (Feistl et al., 2014).

1.4 Objectives

The main objectives of this project are:

1. Include an in depth literature review of snow avalanche dynamics and link correlation between avalanche types, numerical models, and small-scale chute experiments.
2. Provide a brief overview of designing a small scale model to replicate avalanche deposition and overall braking effect of trees on avalanches.
3. Carry out a sequence of small-scale chute experiments in which the front/surface velocity, runout distance, flow height, stem wedge height, mean deposition height/mass and width of the avalanche are measured. Forest density, relative humidity and material types will be varied.
4. Provide a phenomenological characteristics of the avalanche flow through the forest.
5. Quantify the mass extraction coefficient (K-value), front/surface velocity, runout distance, flow height, stem wedge height, mean deposition height/mass and width of the avalanche as functions of the forest density, relative humidity and material types will be varied.

1.5 Limitations

Environmental conditions proved to be a major limitation to producing reliable data. Initially, the room where the chute was placed had a major draft so there was a large discrepancy in humidity from day to day. Creating a dry room dampened the loss or increase in humidity, however, these issues persisted throughout the study. This limits the repeatability of the experiment. Also, by measuring the values by hand limited experiment accuracy.

Ballotini is incompressible and cohesionless, so finding a replacement medium is of particular importance in order to quantify real world mass deposition behind trees. Since there really is nothing similar to snow, the author will have to try a powder based material since densities and compatibility are similar.

Table 1.2: Mass per unit volume of a snow mass can compose of highly varied snow densities (Paterson, 2009)

Typical densities of snow and ice	
Snow Quality	**Density** $[kg/m^3]$
Very light new snow	~ 30 - 70
Damp new snow	100 - 200
Faceted snow	250 - 400
Depth hoar	100 - 300
Wind packed snow	350 - 400
Firn	400 - 830
Very wet snow and firn	700 - 800
Glacial ice	830 - 917

In general, a slab avalanche consists of three main components: a dense core of rounded particles with a diameter of the order of centimetres to metres, a saltation layer or fluidized layer of particles up to 50 cm in diameter, and a suspension layer or powder cloud of particles 0.1 mm to 1-2 mm in diameter. As a rule of thumb, the densities of the three layers are about $300kgm^{-3}$, $30kgm^{-3}$, and $3kgm^{-3}$ (Issler, 2004). Please refer to Tables 4.4 and 4.3 for material specifications to compare these three substances. Moreover, the ballotini ($1583kgm^{-3}$) and alumina ($955kgm^{-3}$) density is nearly twice the amount of the average snow density.

1.6 Approach

A chute experiment will be carried out in the pile laboratory at NTNU's Department of Civil and Transport Engineering. The chute design was originally proposed by Kahrs (2015) and adapted throughout the authors work. A few modification are exposed in Chapter 6.2, Recommendations for Further Work. Both two-dimensional and three-dimensional laterally spreading flow configurations on inclined planes and curved surfaces have been studied with video footage. In this way, the evolution of the edge of the spreading avalanche and the flow depth could be obtained with good precision and resolution (Issler, 2003). However, the optimal way to approach fluid flow is to obtain a particle-image velocimetry device however it might prove tricky; therefore, the experiment will initially be filmed by two cameras with 60fps orthogonal to the sliding plane and also from the side. The resulting videos will be reviewed frame by frame in order to determine the surface velocity and deposition height of the avalanche with help of a distance scale at the bottom the the run-out vs time. The run-out distance will be measured after each trial. Then, by observing the flow of the avalanche frame by frame as it flows through the timberland, overall flow height and deposition height can be attained. Profiles will be plotted and parameters characterized.

1.7 Thesis Structure

The first sections gives an overview of the reason for hazard mitigation regarding small-to-medium avalanches. The second chapter provides insight into the fundamentals of avalanche movement. In Chapter 3, an in depth analysis into snow avalanche flow dynamics and a field study synopsis of the difference between the detrainment approach and Voellmy-Salm friction parameters. Chapter 4 explains the experimental setup and leads into Chapter 5, where the experimental study was performed and raw data analyzed. Chapter 6 is composed of the summary, discussion and recommendations for further work.

Chapter 2

Phenomena of Snow Avalanches

2.1 Terminology

By definition, an avalanche is a mass of snow that flows down-slope an inclined plane. Such movement is directed in the direction of least resistance, which leaves an avalanche path behind. The start zone, otherwise knows as the release zone, is the region where an avalanche is initially triggered. This location could be a single point(crown face) or a bed surface for slap avalanches. At the time of failure, the dense mass accelerates down-slope and along the track at which point terminal velocity is reached. Generally the track is a region with minimal volume release of depositing snow. Provided this phenomena, an avalanche is known to entrain snow upwards of ten times its initial mass which range from 10 to 100000 t. In the deposition zone, which is generally called the runout zone, the avalanche will eventually decelerates and come to a standstill at the toe of the avalanche. As seen in Figure 2.1, the runout zone is essentially the horizontal distance from the top of the release zone to the endpoint of the runout zone.

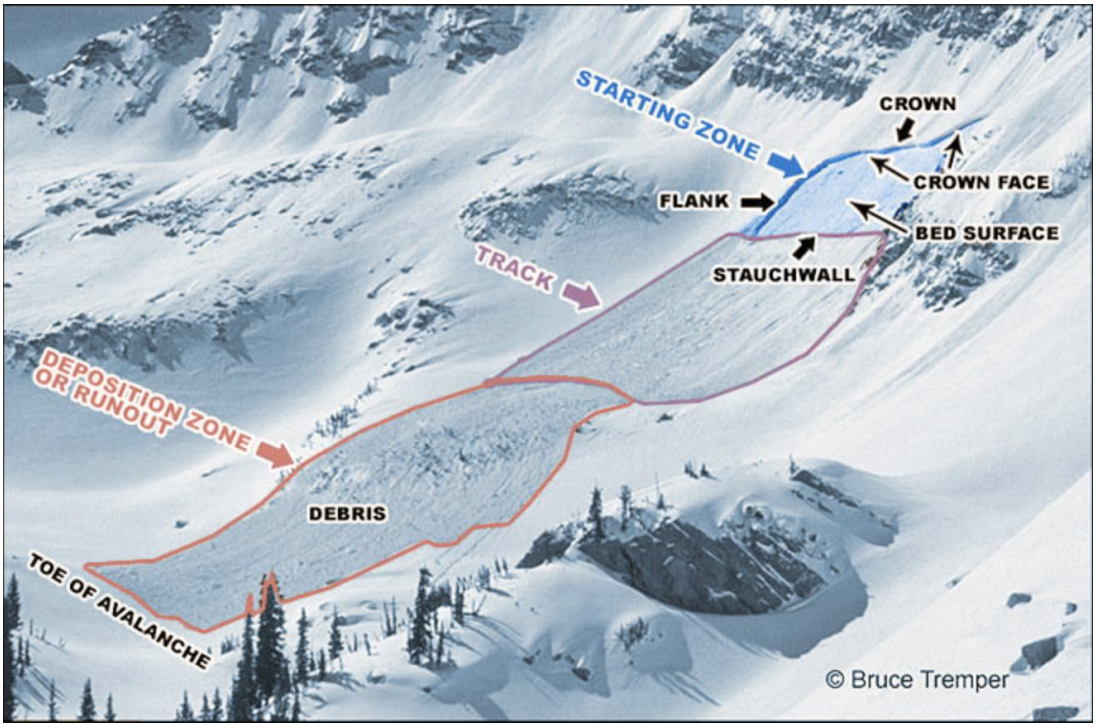

Figure 2.1: Typical layout of a snow avalanche path. (Temper, 2014)

2.2 Snow Avalanche Categories

There are many categories avalanches could fit into, however in this study we will consider the classifications most used. A loose snow avalanche, also known as a point release avalanche, involves unconsolidated snow initiating failure from single point and gradually fans out while moving downhill. The shape is often referred to as a teardrop for which is often triggered on the surface layer (weakest layer) where new snow accumulates, presented in Figure 1.1. Typical examples are loose dry and loose wet point release. Loose dry avalanches are typically small, but have potential to gain significant mass on long steep slopes. Loose wet avalanches are ordinarily triggered during the warmest part of the day on slopes that are sun-baked. This category is more powerful than loose dry avalanches due to their higher density. The second main category is classified as slab avalanches. A slab avalanche is associated with a cohesive block of snow mass that fractures within the snowpack. This fracture spreads laterally across the slope leaving a crown wall. This large block will break up into smaller sections as it slides downhill. The weakest layer is the point of failure since slab avalanches are associated with having a strong layer overlaying a relatively weak layer. When overbearing forces become too large, the weakest layer give and the slab is initiated. Table 2.1 is a good representation of avalanche categories with accompanying slopes which they are generally triggered.

Table 2.1: Typical slope inclinations for different types of avalanches. (Schaerer and McClung, 2006)

Slope gradient	Avalanche type
60°–90°	Avalanches rare, snow glide common in small portions
30°–60°	Dry loose-snow avalanches
45°–55°	Frequent slab avalanches
35°–45°	Slab avalanches of all sizes
25°–35°	Rare (often large) slab avalanches, wet-snow avalanches
10°–25°	Rare wet-snow avalanches and slush flows

2.3 Avalanche Development

2.3.1 Snowpack

As fresh snow falls on a slope, the density approximately $\leq 50 kg m^{-3}$. Although, when wind breaks off the edges snowflakes, it rounds the particles and packs them into denser layers. Once snow accumulates, it initiates a state of physical alteration called metamorphism which continues until melting is exhausted. Through this process, the bulk density of the snowpack develops into common mid-winter values of $200-300 kg m^{-3}$ to form values found in spring $400-500 kg m^{-3}$

Moreover, the snowpack metamorphoses in contrasting methods which is entirely reliant on the exposition and height position within a mountain range. On a micro scale, snowpack structure could be quite distinct and dissimilar. Conversely, if the meteorological conditions are similar within the same exposition and elevation, a very similar snowpack structure is found in large scale (Rudolf-Miklau et al., 2015). In steep terrain where the sun radiation procures a compact snowpack formation, one can find characteristics of a melting hard crust; in retrospect, an accident-sensitive snowpack can be found behind a ridge in very steep shady areas.

2.3.2 Avalanche Movement and Terrain

In principle, every snowpack embedded on a sloped area moves down the valley due to gravity (Rudolf-Miklau et al., 2015). This action is a result of snowpack settlement without an observable fracture formation. As the anchored snowpack sticks to the soil, the snow layers embedded above it constantly creeps down-slope. "The steeper the area, the thicker the snowpack, and the closer to the snow surface, the more intensive is the so-called creeping motion and hence the larger is the ensuing tension" (Rudolf-Miklau et al., 2015).

Although slow, creep forces can decrease or increase in tension within the snowpack. Both active and passive tensions, pressure and shear stress are affected by this movement. Tensile stress typically occurs in extraction areas, that is slope increase, compressive stress in hollow areas, and also at slope decreases (Rudolf-Miklau et al., 2015). The tension component that is decisive for the formation of avalanches, however, is the shear stress, which becomes increasingly larger proportional to how poorly the layers are connected with each other (Rudolf-Miklau et al., 2015).

A general rule of thumb is, the lower the crown of dry avalanches, the longer the runout distances where the opposite are found for wet avalanches. The surface roughness of the underlying terrain is a decisive factor in snow-pack stabilization (Leitinger et al., 2008). While grassy, abandoned meadows and low flexible dwarf shrubs are especially prone to snow gliding (Newesely et al., 2000), fallen logs, remnant stumps of logged or snapped trees, root plates of upturned trees and large rocks all can prevent the formation of small avalanches (Schönenberger et al., 2005). Branch lopping is often linked to tree fracture and low energy consumption which increases avalanche mass and, therefore, flow energy Bartelt and Stockli (2001). It is common to observe dry snow avalanches occur in less dense coniferous forests near timberline. Another observation is that wet snow avalanches are regularly triggered in deciduous forests with crowns starting higher above the ground, where trees are less vulnerable and have a positive decelerating effect on wet snow avalanche runout (Rudolf-Miklau et al., 2015).

2.3.3 Forest Coverage Acting as Avalanche Mitigation

"Because of the processes in forests that stabilize the snow cover, crown cover, size of forest gaps and occurrence of deciduous tree species are often regarded as the chief forest structural parameters that influence avalanche formation in forested areas" Schneebeli and Meyer-Grass (1993). Other than the topographical and meteorological conditions, it is essentially the crown density of the forest stand, the size of the forest cleanings, as well as the existence of winter-bare tree species that are decisive when it comes to avalanches being triggered on forested slopes (Rudolf-Miklau et al., 2015). Furthermore, the evergreen forest climate creates a light warming of the snowpack during the day and a smaller radiation of the snowpack during the night, and thereby impacts the metamorphism of the snow. Due to the microclimate in the forest, surface hoar and depth hoar occur more rarely than on free surfaces, and the warmer temperatures result in a more compact and stable snowpack (Rudolf-Miklau et al., 2015). As a rule of thumb, trees must be at least twice the size of the snow depth in order to contribute to avalanche control (Frehner et al., 2005). For this reason, the uppermost areas in the forest stand, along with the timberline region, take on a fundamental role with regard to the stability of the entire forest below (Rudolf-Miklau et al., 2015).

Chapter 3

Theory

3.1 Antecedental Theory of Avalanche Rheology

3.1.1 Detrainment Approach

Understanding exactly how forests decelerate avalanches has been an enduring problem since the 1930s. Unless otherwise cited, the contents of this section is based primarily on Feistl et al. (2014). Their publication, Observations and modeling of the braking effect of forests on small and medium avalanches, is centered around triggering seven avalanches and observing the deceleration effect trees have on run-out length. His goal was to collect information on release zone location and dimensions, deposition patterns and heights, run-out distance and forest structure since these characteristics directly influence avalanche dynamics.

Dendrogeomorphic processes were quite significant since no trees were completely destroyed in the study but acted as rigid obstacles obstructing avalanche flow. It was observed that wedge-like depositions formed up-slope of individual tree stems, dense tree groups and young trees with low-lying branches. By employing these observations as a guide, Feistl and his team developed a one-parameter function that takes into account the loss of momentum corresponding to the loss of mass stricken by trees. "The function was implemented in a depth-averaged avalanche dynamics model and used to predict the observed run-out distances and mean deposition heights for the seven case studies. The approach differs from existing forest interaction models, which modify avalanche friction to account for tree breakage and debris entrainment. Our results underscore the importance of forests in mitigating the danger from small-to-medium avalanches" (Feistl et al., 2014).

If trees maintain rigidity, the detrainment rate is respectively similar in comparison for extreme avalanches as to smaller scale avalanches. However, this approach is not representative for extreme cases since the energy exerted by trees resisting the avalanche is far less than the overall flow energy and therefore insignificant. The detrainment model properly represents small-to-medium sized avalanches because the percent of overall detrained snow mass is greater, thereby decelerating avalanche momentum at a greater rate.

Observations

Field Campaign Method

Seven avalanches were triggered in the German and Swiss Alps in effort to investigate the amount of mass detrained by timberland. The immobilized mass was estimated by measuring the difference between avalanche volume of initial impact and deposition zone via calculating the volume of wedge-shaped deposits behind the trees. Assuming the forest structure has vital influence on the mass balance and length of run-out distance, vegetation cover and

stem density were carefully measured. The critical point for the deposition model was distinguishing between a canopy density of > 50% for dense forests and < 50% for open forests. Canopy density was determined by investigating orthoimages, 2011, with 25 cm grid resolution, of each event (Bebi et al., 2001).

Table 3.1: Characteristics of forest avalanches documented during the 2008/09 and 2011/12 winters. (Feistl et al., 2014)

	Switzerland					Germany	
	Junkerboden	Filisur south	Filisur north	Dischma	Monstein	Hagenberg	Brecherspitz
Internal ID	ID-I	ID-II	ID-III	ID-IV	ID-V	ID-VI	ID-VII
Date	1 Jan. 2012	~23 Feb. 2012	~23 Feb. 2012	~27 Feb. 2012	1 Mar. 2012	24 Feb. 2009	14 Feb. 2012
Temperature (dry, moist, wet)	moist	wet	wet	wet	wet	dry	dry
Terrain features (upper part/ track/runout)	unchanneled/ unchanneled/ flat	channeled/ unchanneled/ unchanneled	channeled/ unchanneled/ unchanneled	unchanneled/ channeled/ unchanneled	channeled/ unchanneled/ unchanneled	channeled/ unchanneled/ unchanneled	unchanneled/ unchanneled/ unchanneled
Forest structure (upper part/ track/runout)	dense/open/ no forest	no forest/open/ dense	no forest/open/ dense	open/no forest/ dense	open/no forest/ dense	open/dense/ dense	open/dense/ dense
Tree age	mixed	mixed	mixed	mixed	mixed	mixed	mixed
GPS measurements of deposits	✓	✓	✓	✓	✓	–	✓
GPS measurements of release area	✓	–	–	✓	–	–	✓
Image of release	✓	–	–	✓	✓	✓	✓
Altitude (m a.s.l.)	1540–1500	1320–1080	1360–1058	2093–1642	2070–1640	1419–1027	1472–1327
Slope angle, release to runout (°)	39–0	50–25	50–20	42–15	50–10	50–25	45–23
Release volume (m^3)	320	1080	1390	3690	5190	3460	690

Topographical features such as gorges, ridges, and angle of repose were taken into account to identify plausible starting zones. “It was essential to document the exact shapes of the release and deposition areas, to allow comparison with simulation results via use of dGNSS device since it is in the range of a few centimeters” (Feistl et al., 2014). In relation to lateral displacement, the foremost deposition zone within the forest were concentrated along the outer tracks of the avalanche path where flow velocities were the lowest. Also, it was noted that altering snow conditions deposited snow at different quantities due to slope angle, snow temperature, density and age of trees.

Volumetric Deposition Behind Trees

Each case study pertaining to ’Observations and modeling of the braking effect of forests on small and medium avalanches’ resulted in wedge-shaped depositions compacted around the up-slope portion of trees. Wedge-shaped depositions have been measured behind obstacles in chute experiments with granular materials (Gray et al., 2003) along with observed wedge-shaped deposition behind pressure-measurement pylons at the Swiss Vallée de la Sionne (Sovilla et al., 2010) and Italian Seehore avalanche test sites (Bovet et al., 2011). Undesirably the depositional shapes comprised of different dimensions but this was due to differential snow properties and tree stump dimensions.

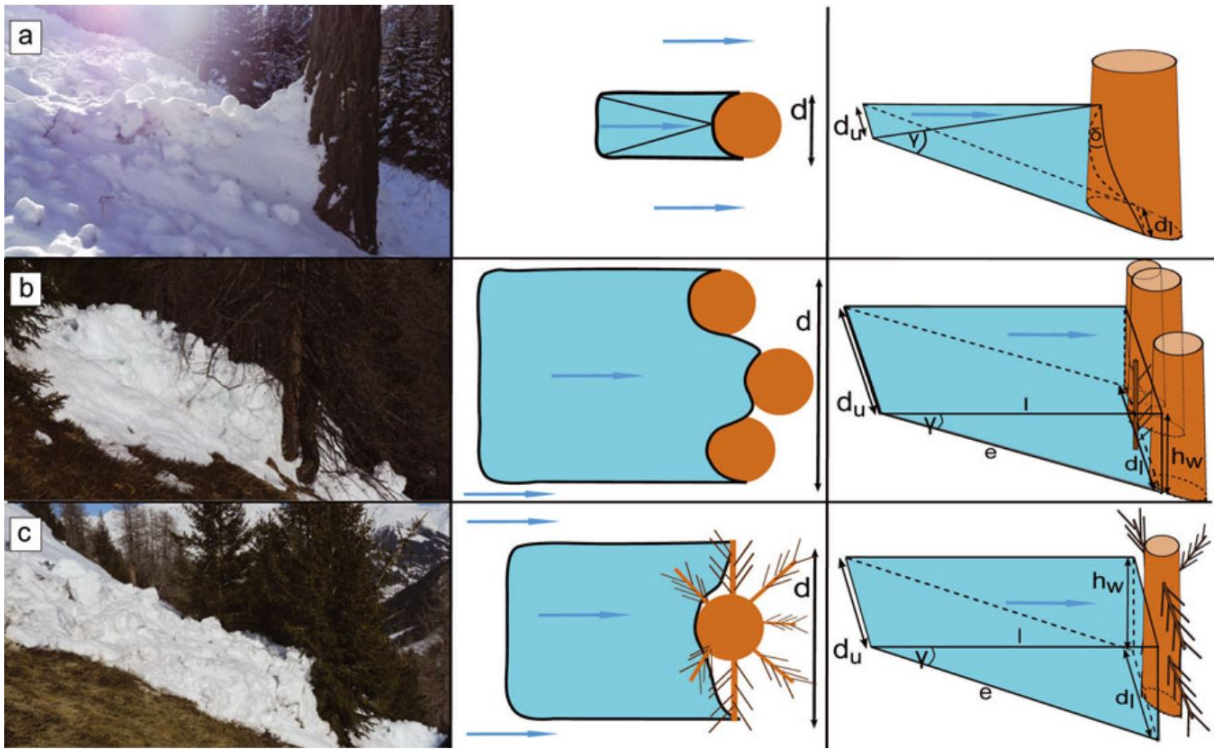

Figure 3.1: Representative wedge-shaped deposition structure of snow avalanches behind trees. The First column are images taken in the field study, (a), of deposited snow behind a single trunk of 100cm diameter in relatively flat terrain (20°). The second column depicts the deposition in plan view, (b), of deposited snow behind a group of trees. The third column provides insight into the dimensions of, (c), plugged snow deposits behind a small tree (4 m high) in steep terrain (34°); note the outcome of branches close to the ground maintains vertical side-walls. The horizontal wedge length, l, and the slope-parallel wedge length, e, depend on the wedge height, h_w, and on angle γ. (Feistl et al., 2014)

Observations proved that the upper and lower base width of the wedge are approximately the same extent, $d_u = d_l = d$, and the base width, d, is equal to the width of the obstacle (stem or tree group). Trees with low-lying branches that droop into the understory have base width much greater than just the stem diameter since there is more surface area obstructing avalanche flow. As presented in Figure 3.1, the dimensions after collision results in a pyramid-shaped wedge deposition where in b and c the dimensions are clearly represented in a wedge form.
The field campaign provided for quantitative values of the volume, W, of snow captured behind one tree or group of trees. The wedge volume for the single-stem case 3.1 a can be calculated by:

$$W = \frac{d^3}{12\tan(\gamma)\tan^2(\delta/2)} \tag{3.1}$$

$$W = \frac{d\,h_w\,I}{2} = \frac{d\,h_w^2}{2\tan\gamma} \tag{3.2}$$

where h_w is the height wedge deposit and l is the horizontal wedge length to the surface. Calculated volumes of the wedges are portrayed in Figure 3.1 and the dimensions are provided in 3.2. In situation b (tree groups) and c (low-lying branches) the detrained volumes are far greater than for the single-tree case.

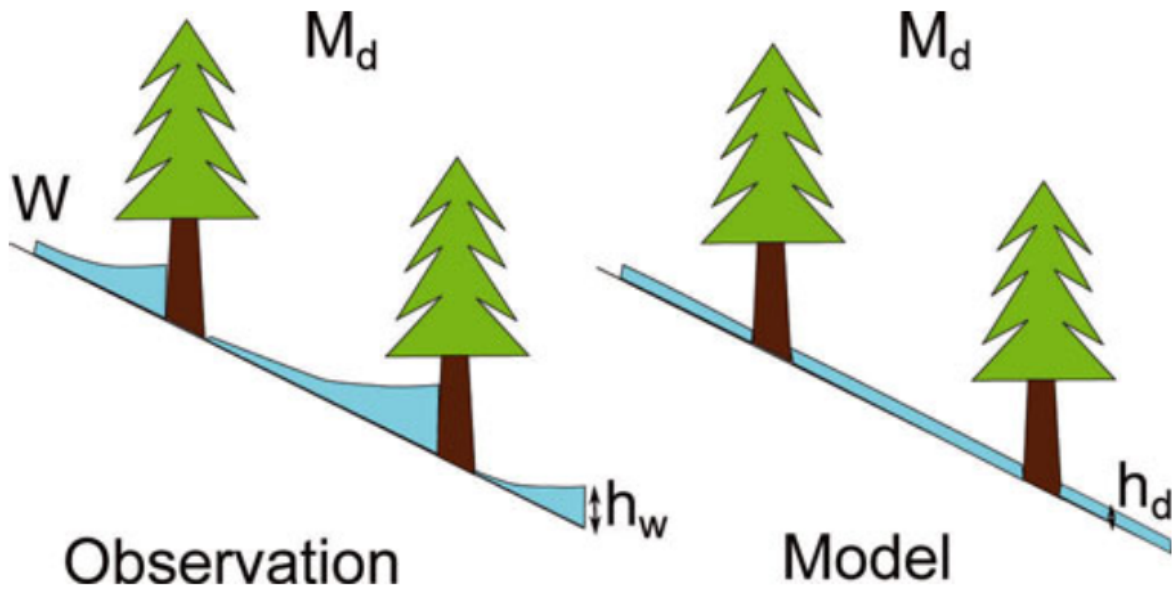

Figure 3.2: The reason for the forest model is to calculate the mean deposition height, h_d. Wedge development behind isolated trees are not predicted. The total deposited mass, M_d, should, however, be equivalent to the observations. W is the volume of snow immobilized behind a single tree or tree group. (Feistl et al., 2014)

By utilizing the volumetric deposition (Eqn. 3.1 and 3.2), it is possible to derive mean deposition height values for different stem densities. The mean deposition height for the entire protection forest, h_d, is intrinsically dependent on the forest structure such as tree density and deposition width. Table Table 3.2 evaluates the forest structure via correlation of tree (stem) density and the rate of mass extraction coefficient, K. For the first case: 400 trees per hectare with average stem diameter at $d = 1m$, angle of repose at 30° and top wedge angle $\delta = 60°$, a surprisingly small average deposition height, $h_w = 0.2cm$, was observed throughout the entire forested area stricken by an avalanche.

Table 3.2: Contains wedge dimensions and calculated volumetric depositions based on Figure 3.1. Case b (group of trees) and case c (trees with underlying branches) catch more mass than case a (single trunk) (Feistl et al., 2014)

Observation	**Slope angle** °	**Width, d** m	**Wedge height,** h_w m	**Top wedge angle,** δ °	**Volume, W** m^3
a	23	1	0.8	68	0.43
b	33	4	2	-	12.3
c	34	2	2	-	5.9

Table 3.3: Deposited snow and equivalent mean deposition height, h_d, for angle $\gamma = 30°$ which is approximately equal to the slope angle of the terrain, wedge height $h_w = 2m$, top wedge angle, $\delta = 60°$. The tree diameter, d, is 1m for a single tree, 2m for a tree with branches extending to the ground and 4m for a group of three trees. We assume a snow density of $\rho = 300kg/m^3$, an avalanche length of 50m and a velocity of 10m/s to calculate K according to Eqn. (14)

Forest structure	**Stem density** h_a^-1	**Deposition volume** m^3	h_d m	**K-value** Pa
Single trees	400	173	0.02	10
Group of trees	400	1842	0.18	110
Trees with branches	400	2771	0.28	166
Single trees	200	87	0.01	5
Group of trees	200	921	0.09	55
Trees with branches	200	1386	0.14	83

To rid any uncertainties, the values calculated in Table 3.3 are dependent on the values listed in the caption and not the observed values in Table 3.2 As presented in the table above and Table 3.1.4, settled snow stopped by the forest can increase by a factor of >10 when wide, wedge-shaped deposits are formed behind groups of trees. When $d = 4m$ for a forest with the same stem density but trees are grouped together, which contain three trees (3.1b), then the mean deposition height is 18cm. This outcome exposes the paramount importance of not only the stem diameter, but the forest structure as well. In general, mean deposition heights up to 50cm is a realistic amount of immobilized snow by forests, $1cm < h_d < 50cm$ (Feistl et al., 2014).

3.1.2 Avalanche Modeling

Currently, there are numerous avalanche models that require very specific input for desired qualitative avalanche outcomes. An overview of the development of modeling snow avalanche simulations is provided in Figure 3.3 Calculation models are generalized into two different categories: statistical-topographic and physical-dynamic models (Rudolf-Miklau et al., 2015). Forrest effects on avalanche dynamics have utilized the numerical calculation programs RAMMS with a brief introduction to Alpha-Beta and Voellmy-Salm methods also.

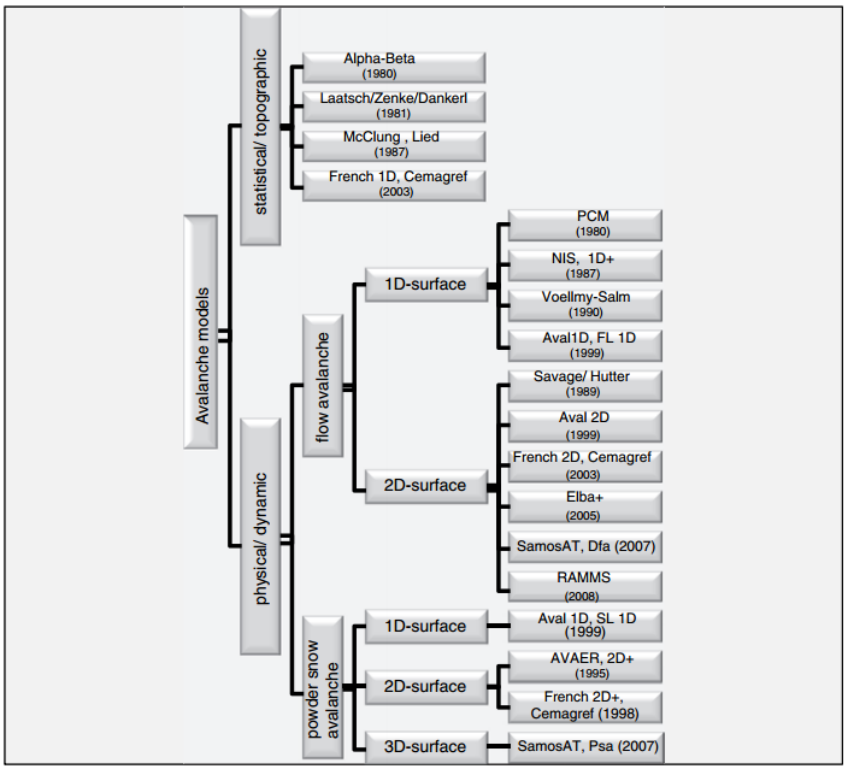

Figure 3.3: Overview and classification of common avalanche models (classification and dimensioning relative to the corresponding calculation platform)(From: Granig, Margreth)(Rudolf-Miklau et al., 2015)

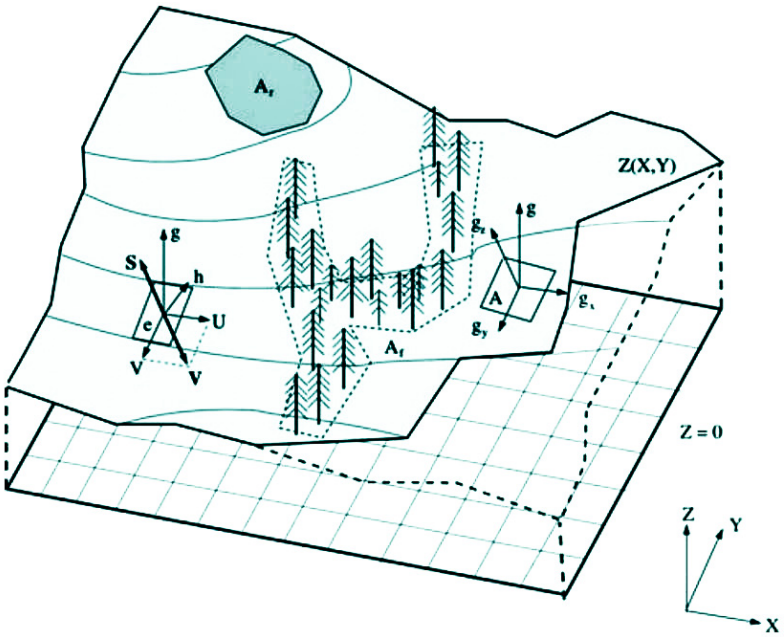

Figure 3.4: Overview of the model orientation and definition of primary variables: A_r is the release area. A_f is the forest area. U and V are the velocities in x- and y-direction, respectively. The gravitational acceleration in the x-, y- and z-directions is denoted $g_x, g_y and g_z$. S is the resistance opposing the direction of velocity, V. (Feistl et al., 2014)

The applied numerical simulation used to phenomenologically describe avalanche behavior flowing through protection forest for cases a, b, and c (3.2) is Rapid Mass Movements

(RAMMS). This software was employed to simulate the several observed snow avalanche events and to perform simulations on an ideal parabola-shaped avalanche track (Christen et al., 2001). The mountain profile is oriented via X,Y coordinate system. The elevation profile defined for each coordinate pair (X,Y) is represented as, Z(X,Y). Snow avalanche modeling parameters include: Local surface based coordinate system (x,y,z). Avalanche flow height, h(x,y,t). Mean avalanche velocities, U(x,y,t)and V(x,y,t), in the x- and y-directions, V = (U,V)T (Figure 3.4). By using depth averaged mass and momentum balance, avalanche flow can be simulated with the equations (Christen et al., 2001):

$$\frac{\partial h}{\partial t} + (\mathbf{V} \cdot \nabla) h = Q \tag{3.3}$$

$$\frac{\partial (h\mathbf{V})}{\partial t} + (\mathbf{V} \cdot \nabla)(h\mathbf{V}) = \mathbf{G} - \mathbf{S} - \frac{1}{2}\nabla(g_z h^2) \tag{3.4}$$

Resistance is designated as $S = (S_x, S_y)^T$ and gravitational acceleration, g, is $G = (G_x, G_y)^T$ are given by:

$$G_x = g_x h \tag{3.5}$$

$$G_y = g_y h \tag{3.6}$$

$$g = g_x \mathbf{i} + g_y \mathbf{j} + g_z \mathbf{k} \tag{3.7}$$

The unknown field variables h(x,y,t) are a function of time, t, thereby providing enough information to back-calculate from initial release from (t=0) to avalanche termination in the deposition zone. Further parameters described in Figure 3.4, which are included in the calculation based model are: A(x,y) is denoted the position of the avalanche release zone such as a forest opening or a region located above natural vegetation line. The region A_f is defined as the forest area. Mass entrainment from the fresh snow cover along with snow detrainment is specified by the volumetric mass flux, Q(x,y,t), and is defined per unit area. "However, as we assume no mass uptake in forested areas, we did not account for entrainment in this study. We therefore define $Q = -h_d$ as the detrainment rate. This provides the mean deposition height, h_d, of stopped snow mass in the forested area, A_f" (Feistl et al., 2014). A supplementary depth-averaged energy balance equation integrating kinetic energy, R(x,y,t), associated with particle velocity fluctuations, is included in the RAMMS model (Bartelt et al., 2012).

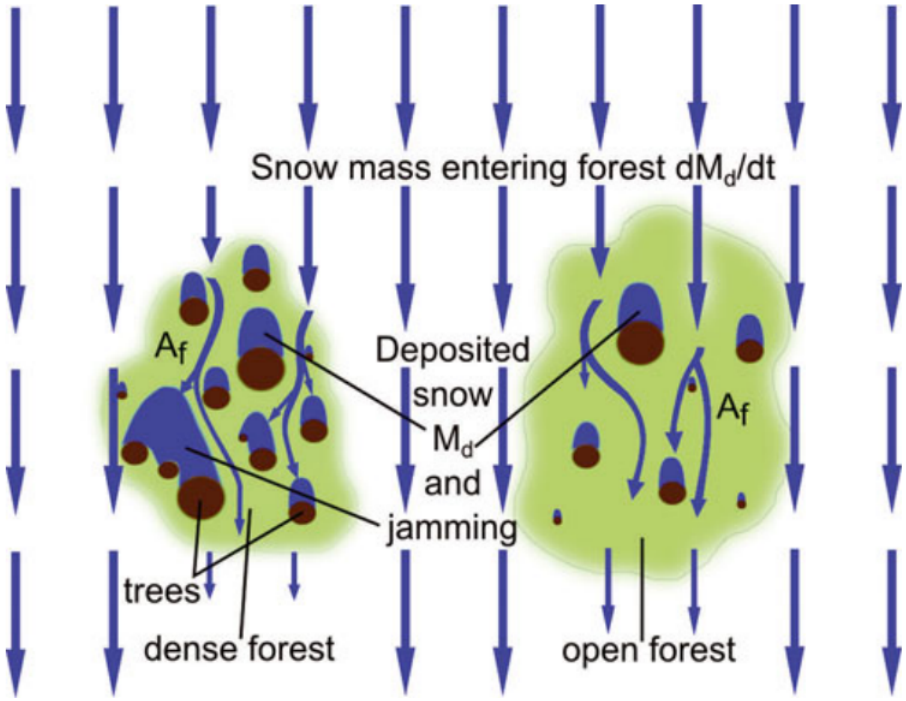

Figure 3.5: Diagram of the mass flux before and after the collision with variable forest densities between single stems and groups of trees. This illustration provided insight into the method of which deposited snow is jammed behind trees most effectively if groups of trees are present. Larger detrainment K-values are applied for the denser forest. (Feistl et al., 2014)

Fluctuation Energy: α- and β-Method

$$\frac{\partial(hR)}{\partial t} + \mathbf{V}\cdot\nabla(hR) = \alpha(\mathbf{S}\cdot\mathbf{V}) - \beta(hR) \tag{3.8}$$

Parameter α is an extraneous factor that determines the behavior of random fluctuation energy, R, from the frictional work rate of the mean flow, $W_f = S \cdot V$. Therefore, when $\alpha > 0$, we have more scattered flows via particle collision; α_S corresponds to the granular stresses caused by fluctuating particle motion for which heat generation is not relevant but considered as a turbulent Reynolds stress, such as for conventional fluids. The dissipation of fluctuation energy i.e. collisions, plastic deformation, abrasion, and fragmentation are characterized by parameter β. In order to represent real world scenarios, random kinetic energy variables are vital to the model formulation when calculating the distribution of cold, dry avalanche deposits as well as small avalanche rheology (Bartelt et al., 2012).

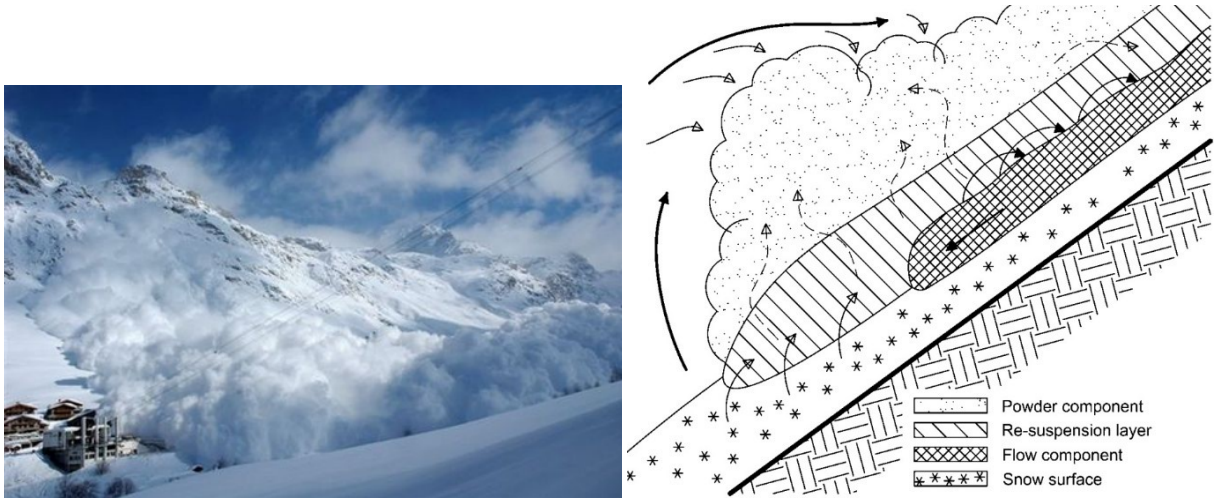

Figure 3.6: Schematic motion of a mixed avalanche relating flow and powder components. (n.a., 2010),(National Avalanche Center, nd)

3.1.3 Friction Approach: Voellmy Friction Parameters μ, ξ

$$S_x = \frac{U}{\|\mathbf{V}\|}\left[\mu(R)g_z' h + \frac{g\|\mathbf{V}^2\|}{\xi(R)}\right] \tag{3.9}$$

$$S_y = \frac{V}{\|\mathbf{V}\|}\left[\mu(R)g_z' h + \frac{g\|\mathbf{V}^2\|}{\xi(R)}\right] \tag{3.10}$$

Voellmy friction parameters, μ and ξ, are functions of the mean fluctuation energy, $R_h(J/m^2)$. $R_0(J/m^2)$ is the activation energy per unit area controlling the inception of the fluidized regime (Bartelt et al., 2012) and is entirely dependent on avalanche size and the overburden properties tied to breaking the bonds of cohesive snow. The relationship is described via equations:

$$\mu = \mu_0 \ \exp(-\frac{Rh}{R_0}) \tag{3.11}$$

$$\xi = \xi_0 \ \exp(-\frac{Rh}{R_0}) \tag{3.12}$$

By summing the mean overburden pressure and cohesion, a guesstimate for the required activation energy, R_0, is possible. Exact calculations of required activation energy, R_0, is carried out via back calculations based on field observations for which is depicted in further detail via equation 15 below. The static Coulomb friction parameter, μ_0, and the speed-dependent friction parameter, ξ_0, are characteristics of avalanche flow before fluidization. For more in depth material regarding the numerical implementation of standard Voellmy–Salm (VS) model ($\alpha = 0$) with constant friction parameters, μ and ξ, see (Christen et al., 2001), and for the role of fluctuations in avalanche flow refer to (Bartelt et al., 2012).

3.1.4 Avalanche Regime Through Timberland

The model simulates flow through forests by the mean deposition height, h_d and then multiplied by the element area, which is clearly represented by Figure 3.4, and previews the total deposited volume observed in the case studies. Isolated trees are not considered to be part of A_f due to the fact that they stop too little snow mass to have a consequence on the overall

flow behavior of the avalanche. Over-all, there are two conceivable methods to model the braking effect of forests: (1) the friction approach and (2) the detrainment approach Figure (3.7).

Friction Approach

This approach modifies friction parameters, μ_f and ξ_f, which are allocated to the forest domain, A_f, to model the enhanced braking effect. For instance, in the current version of RAMMS, coefficient ξ_f is presumed to be 400 m/s^2, being significantly smaller than the open-terrain coefficient of 2000 m/s^2, and coefficient μ is only slightly increased (Gruber and Bartelt, 2007). These standards are grounded on energy arguments in which different failure modes; i.e. tree overturning, trunk fracture, and entrainment of woody debris extract flow energy from the avalanche (Bartelt and Stockli, 2001). "The fundamental assumption in this approach is that the avalanche is both large enough and fast enough to induce tree failure. This approach is presently employed to model all avalanche flows in forests, independent of the avalanche size" (Feistl et al., 2014). The modified μ and ξ values are derived from mechanical processes, i.e. tree overturning or trunk fracturing. Although, for small-to-medium avalanches, it is assumed that the trees do not break so the friction parameters, μ_f and ξ_f, are regarded as non-destructive processes, such as jamming.

Detrainment Approach

This method goes in depth into the mechanics of the extraction of mass that is pinned behind tree trunks as the avalanche flows through timberland. This approach is an alternative method to model the forest/avalanche interaction that was previously characterized by friction parameters. Since this method is upcoming, it has been deemed the detrainment approach and postulates that when mass is stopped behind dense tree trunks, it is instantly withdrawn from the avalanches momentum. The stopping is abrupt and mainly caused by material jamming, which is accumulated behind dense grouping of trees. This approach is particularly interesting because the momentum of the stopped mass is directly removed from the total momentum of the avalanche flow Figure 3.7 (Naaim et al., 2004).

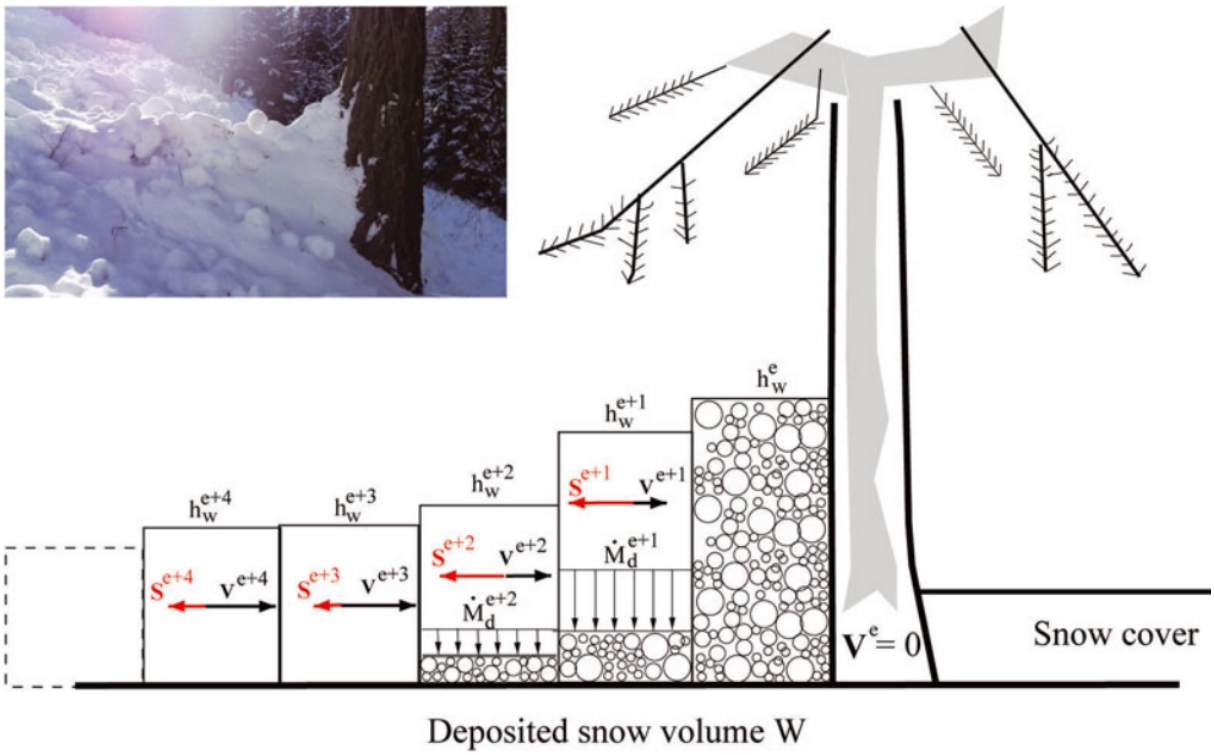

Figure 3.7: Two approaches can be used to model tree interaction with avalanches. The friction approach attempts to find values for S to stop the mass. The detrainment approach determines M_d and extracts the corresponding momentum from the flow (Feistl et al., 2014).

Since it is assumed that the trees do not snap and act as rigid obstacles instigating mass deposition, modeling with Voellmy-type parameters becomes problematic for the reason that the friction coefficients, particularly ξ, are designed for avalanche flow in open terrain where the dissipative processes are slow and constant and is not designed to model tree impact. "Instead of attempting to define friction values that slow the avalanche, and therefore allow the avalanche to naturally detrain material (Naaim et al., 2003), we impose a stress, K (Pa), which instantly detrains mass from the flow. This stress must be in balance with the change in momentum associated with the detrained mass per unit area, M_d" (Feistl et al., 2014):

$$\frac{dM_d}{dt}\|\mathbf{V}\| = -K \tag{3.13}$$

V is denoted as the avalanche velocity with respect to average depth. Although the deposit height can vary from tree to tree, the average mass per unit area, M_d, is important for the momentum balance equations where stress, K, is devoted to the forest structure and density but also properties of flowing snow:

$$\frac{dM_d}{dt} = -\frac{K}{\|\mathbf{V}\|} \tag{3.14}$$

This equation can also be restructured with respect to mean deposition height.

$$\rho\frac{dh_d}{dt} = \frac{K}{\|\mathbf{V}\|} \tag{3.15}$$

Where ρ is the overall flow density and K is representative of granular jamming behind

trees. Since this postulation is only valid for small to medium size avalanches, detrainment parameter, K, is determined to simulate non-destructive processes.

3.2 Results of Forest Effects on Avalanche Dynamics

3.2.1 Numerical Simulation

This numerical experiment was carried out in effort to distinguish the differences between the friction and detrainment approach. The numerical analysis enables multiple simulations with equal initial conditions and varying forest characterizations to model real world scenarios. The ideal avalanche track has been determined as an unchanneled parabola-shaped formation which essentially simplifies complex terrain features (3.8). The average vertical exaggeration between the release zone and deposition zone is 380 m and the snow avalanche (represented as a parabola) has a run out area of 300 m length.

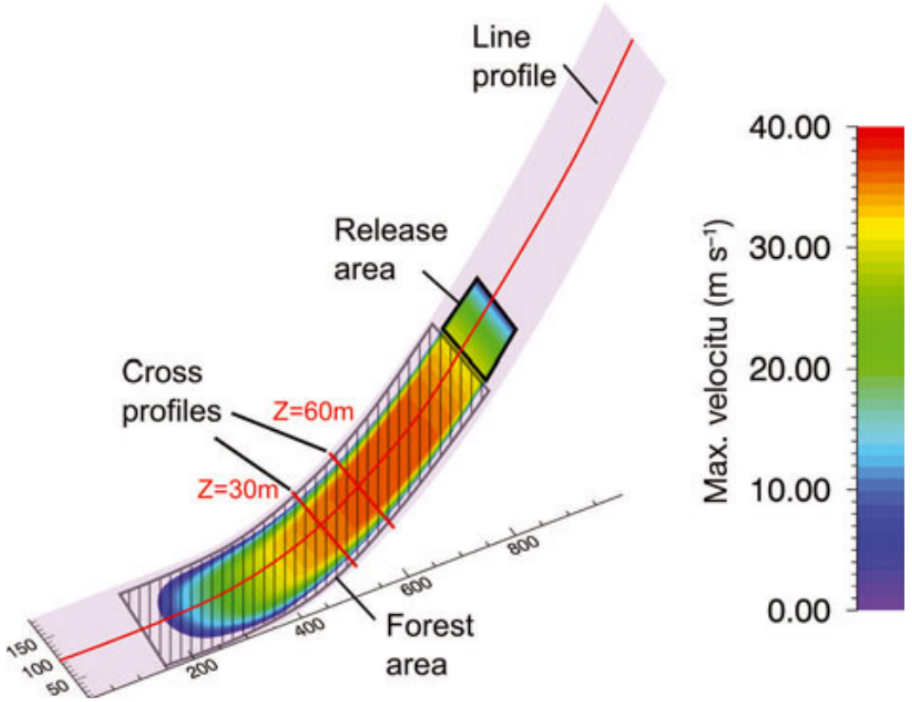

Figure 3.8: Parabola-shaped avalanche track simulation for which the maximum calculated velocity for a release volume of 20,000 m^3 is presented. (Feistl et al., 2014)

Feistl and his team were particularly fixated around the influence of forests on different size avalanches. The simulation introduced three numerical avalanche simulations with varying initial volume and a fracture depth of 1m and then alternated between the standard Voellmy model, $\alpha = 0$, and $\alpha \neq 0$ for increased fluctuating particle motion. Also, the model incorporates the rheology of an avalanche moving through a forest ($A_f \neq 0$) and without a forest ($A_f = 0$) over a specified grid size of 1m. In order to successfully simulate the effects of forests on avalanches, the starting zone, fracture depth, snow density ($\rho = 300 kg/m^3$) and friction parameters, $\mu = \mu_0 = 0.26$ and $\xi = \xi_0 = 2000 m/s^2$, have to be well-defined for in-situ accuracy. The resultant volumes, V_0, are as follows: (a) 1000 m^3, (b) 5000 m^3, and (c) 20,000 m^3.

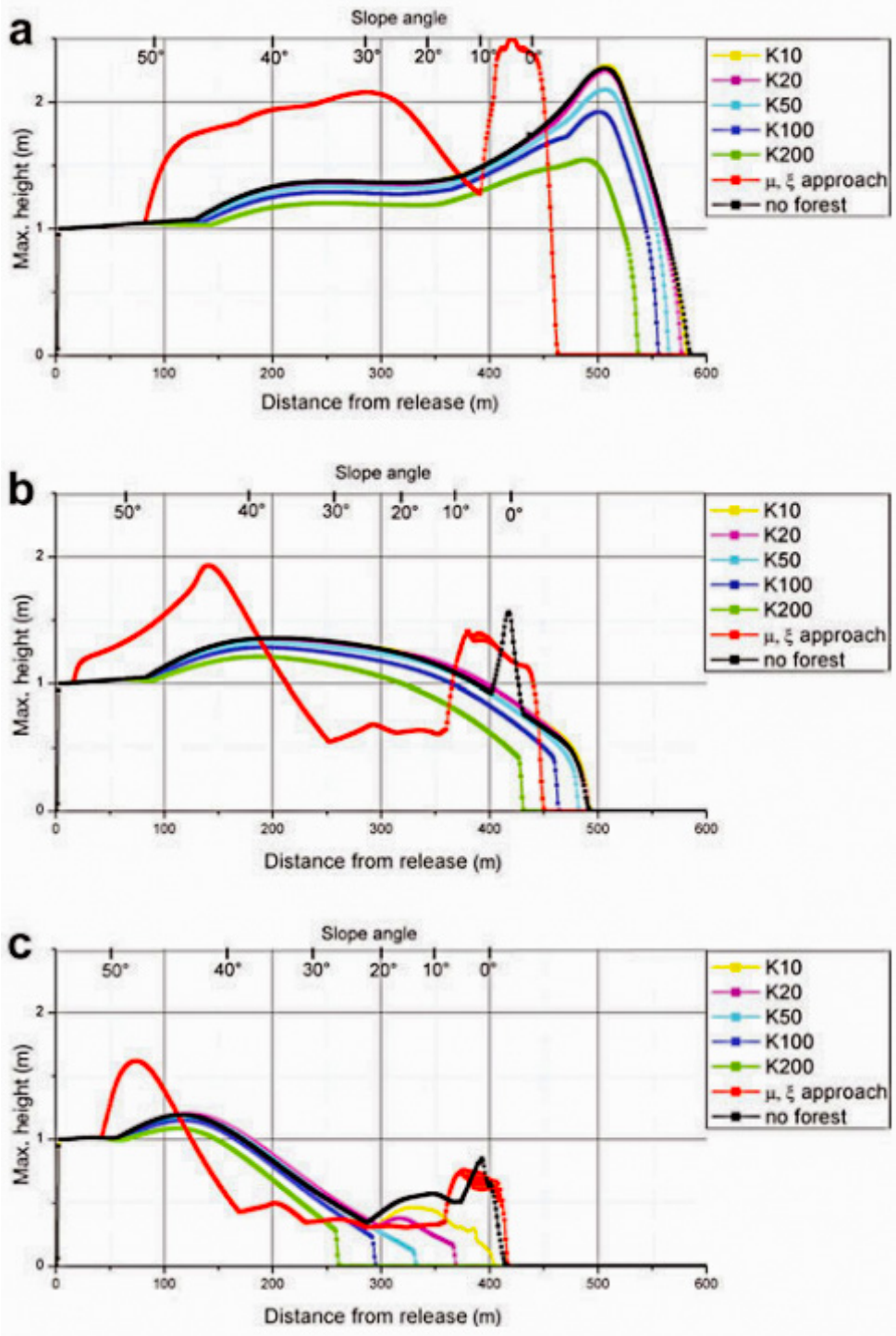

Figure 3.9: Fig 9. Maximum flow height profiles for simulations of snow avalanches with dissimilar release volumes: (a) 20 000 m^3; (b) 5000 m^3; (c) 1000 m^3 and calculated via VS model of RAMMS on a parabolic slope using both the friction and detrainment approaches. Five different values for the detrainment coefficient, K (Pa), were tested (K10, K20, K50, K100, K200). (Feistl et al., 2014)

Although both friction and detrainment methods have the same aspiration of bringing flowing mass to a standstill, the results expose vital differences. As portrayed in Figure 3.9 above, there consists a significant run-out shortening for smaller avalanches using the detrainment approach compared to larger avalanches using the friction approach. “The spikes in height at 400 m distance from release, when simulating with the friction approach and

without forest for 5000 m^3 and 1000 m^3, originate from the pile-up of snow at the transition between sloped and flat (0°) terrain. This spike is missing when using the detrainment approach because the snow is already deposited on the track" (Feistl et al., 2014).

An open forest is represented by K-value of 10 Pa, and dense forest with tree clusters and low-lying vegetation is relative to K-value of 200 Pa. These detrainment Voellmy simulations were specified with specific guideline friction parameters of μ =0.26 and $\xi = 2000 m/s^2$ for frequent avalanches. "This finding suggests that the immediate stopping and removal of flow mass because of trees has a greater influence on small avalanches than on larger avalanches" (Feistl et al., 2014).

Simulation of Observed Avalanches for Dissipation of Fluctuation Energy, α = 0

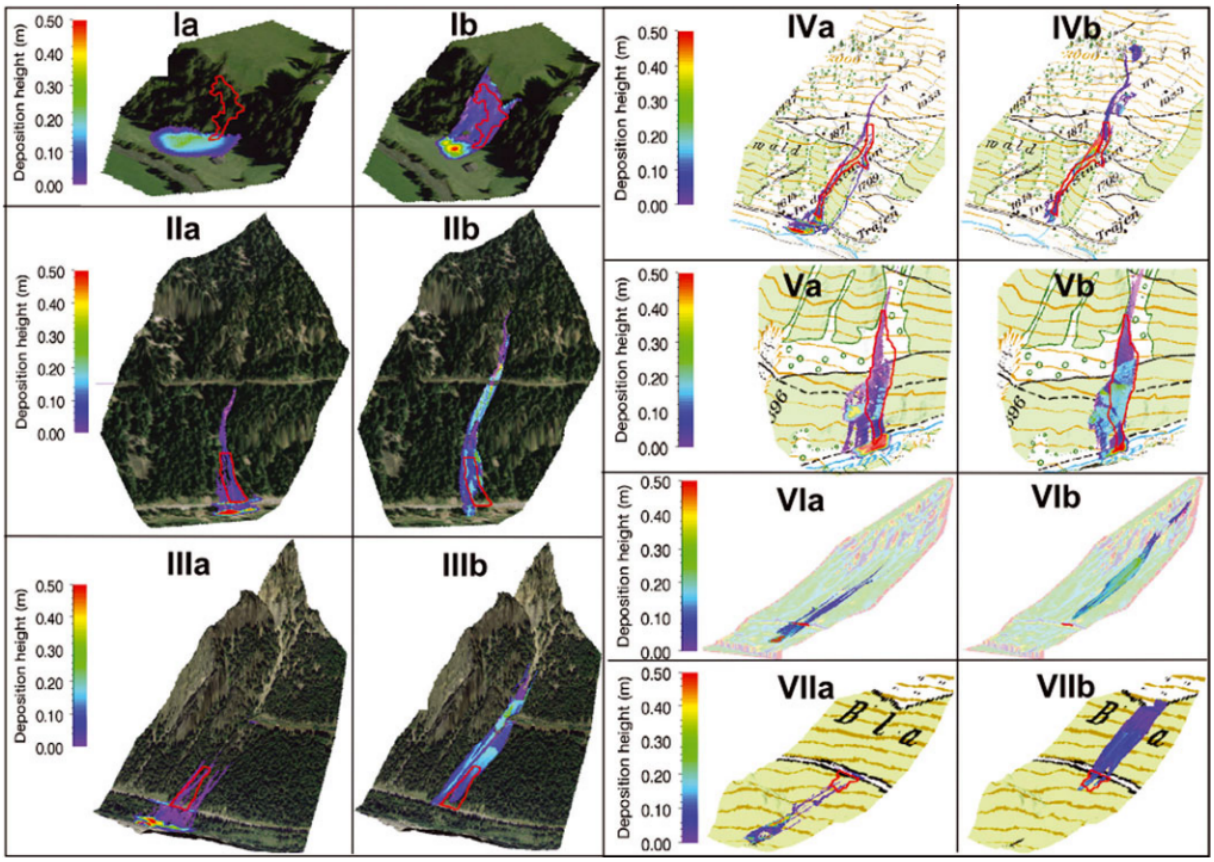

Figure 3.10: Simulation results comparing the seven observed snow avalanches (ID-I to ID-VII). Deposition heights, 50 cm are shown for (a) the friction μ, ξ approach and (b) the detrainment, K, approach. With help of differential GPS imagery, runout areas were carefully measured for cases (ID-IV and ID-VII) and photographs (ID-VI) are outlined in red.(Feistl et al., 2014)

It is apparent in Figure 3.10 that the run-out distance for each case study is overestimated when using the friction approach where the detrainment approach overestimates; two cases significantly (ID-I, ID-V), slight overestimation of two cases (ID-II, ID-IV), and matches the run-out length in two cases (ID-III, ID-VII) and slightly underestimates one case (ID-VI).Input parameters remained identical for all simulations, however, only the forest friction parameters and detrainment coefficients, K, were varied according to dense and open forest structure. "Release areas and fracture heights were specified according to the observations of the field studies or, when it was impossible to enter the release zone, by applying a terrain analysis. The open-terrain and values were defined by the automatic procedure within RAMMS"

(Feistl et al., 2014).The following values were designated according observations taken in the field:

- K = 30 Pa (K30) for dense forest with single tree trunks, some structures of trees groups, and few low-lying branches that bring rise to jamming;
- K = 10 Pa (K10) for forest structures considered to be wide open or possibly older forests. (Feistl et al., 2014)

It is important to note that the run-out for the simulations using the friction approach continuously surpassed the run-out distance of the detrainment approach. This simulation made it apparent that the avalanches reached the valley bottom when using the friction approach and is therefore unimpeded by timberland. This is conceivable, because the friction parameters are well founded for extreme cases, nevertheless emphasizes the complications of calibrating forest friction parameters for avalanche of all magnitudes. Additionally, it is observed that more snow was deposited on the avalanche tracks when the detrainment approach is employed, thereby forced avalanches to stop on steep slopes in several cases (ID-II, ID-III, ID-VI, ID-VII).

When the Hagenberg (ID-VI)3.12 avalanche was released during extremely frigid conditions composed of dry, cohesionless snow, the granules merely flowed around the trees and ended up surpassing the road and predetermined run-out length. This under-prediction can be ascribed to the lack of jamming of snow on trees. Consequently, this avalanche was simulated assuming $\alpha \neq 0$ in order to account for the fluidization of the flow for which more accurate results were achieved.

Simulation of Observed Avalanches for Fluctuation Energy, $\alpha \neq 0$

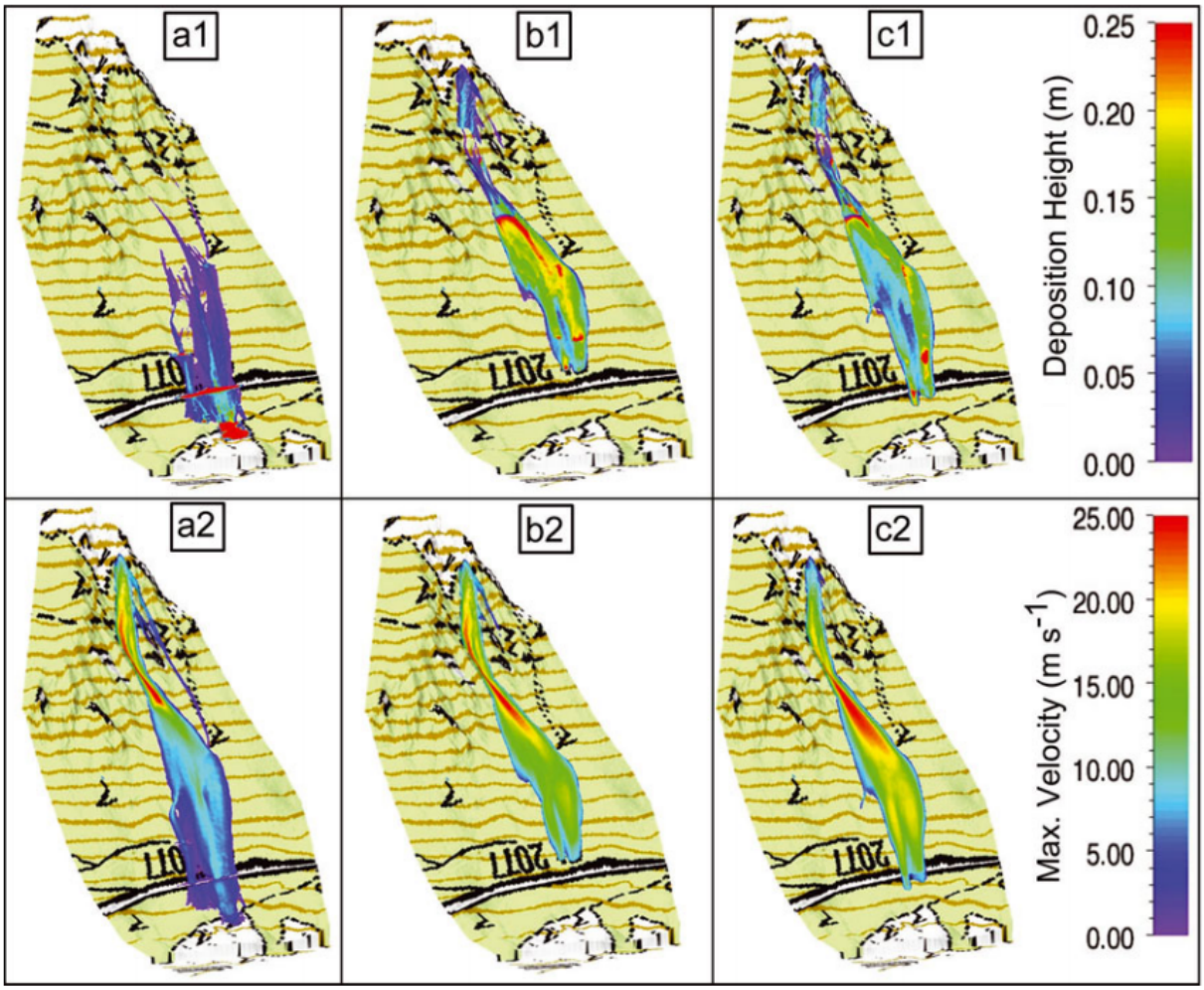

Figure 3.11: Comparison of the Hagenberg (ID-VI) avalanche that demonstrates the variations between the friction approach in the first column (a1, a2), the detrainment approach with VS ($\alpha = 0$) in the second column (b1, b2), and the detrainment approach when $\alpha \neq$ in the third column (c1, c2). The heights of snow deposition comprise the upper row while the maximum velocities denote the lower row. (Feistl et al., 2014)

The similarity between the deposition shapes are remarkably similar in regards to the detrainment approach. The "The real avalanche reached the road and covered it with several meters of snow, but did not flow further into the forest below" (Feistl et al., 2014). For the reason that the avalanche flow was dry and cold, the following parameters were used to replicate in-situ conditions: Flow density of 250 kg/m3, mean flow height of h = 0.8 m 3.12, and cohesionless, c = 0. Also assumed soft snow being $\alpha = 0.05$ for the generation of random kinetic energy, which is fewer than (Bartelt et al., 2012) used for their calculations. Based off snow quality, the energy decay, $\beta = 0.7$ (Buser and Bartelt, 2009). Lastly, depending on the forest structure, K-values were between 10 and 30 Pa.

By summing the mean normal stress, N, and cohesion, c, the activation energy of avalanche initiation can be calculated:

$$R_0 \approx N + c = \rho g h + c \approx 2.0 \tag{3.16}$$

	Avalanche ID						
	ID-I	ID-II	ID-III	ID-IV	ID-V	ID-VI	ID-VII
Calculated mean velocity ($m\,s^{-1}$)	10	17	14	15	12	20	16
Calculated mean flow height (m)	0.4	0.8	0.5	1.3	1	0.8	0.6
Observed forest characteristics	trees with branches, 400 stems ha^{-1}	groups of trees, 300 stems ha^{-1}	groups of trees, 500 stems ha^{-1}	groups of trees, 300 stems ha^{-1}	groups of trees, 300 stems ha^{-1}	groups of trees, 400 stems ha^{-1}	groups of trees, 400 stems ha^{-1}
Calculated de-trained volume (m^3)	110	880	1160	2750	3180	2980	590
Calculated h_d (m)	0.06	0.09	0.09	0.21	0.25	0.11	0.05
Calculated range for d (m) 1.1–1.5	0.6–1.7	1.1–2.7	0.4–2.1	0.9–2.8	0.5–1.5	0.5–1.3	
Observed d (m)	<2.0	<3.0	<3.2	<5	<3.0	<1.5	<1.5
Picture						–	

Figure 3.12: Measured characteristics of the seven avalanche include: mean velocity, mean flow height, detrained volume and mean deposition height, h_d. Deposition widths, d, and wedge height, h_w, which is roughly three times as high as the flow depths. Forest densities are taken from observations; though, we assume tree-stand clusters comprising of three trees. The photographs display distinctive deposition patterns of the six avalanches documented in winter 2011/12. (Feistl et al., 2014)

Chapter 4

Experiments

This section will contain an overview of methods used throughout the experimental study. Including but not limited to reasons for materials types, modifications to chute design, and controlling the environment within the lab. Particularly, which parameters are varied, which parameters are measured, and equipment used for measuring and recording data within the experimental study. The collection of macroscopic solid grains such as ballotini are practical in replicating avalanche rheology due to inherent properties that exhibits both liquid and solid characteristics.

4.1 Objectives

This thesis focuses on the effects certain forest densities have on rheological properties of a flowing mass. The friction approach along with the approach centered around the change in mass/momentum are studied in detail. Variables not considered throughout this study is forest in the release zone and trees braking or overturning due to overbearing avalanche flow.

Four phenomena that may be considered when studying the flow of a snow avalanche through a forest are: (1) the hydrodynamic effect of a group of rigid obstacles in the flow path, (2) reinforcement of the snow by broken trees, (3) energy loss due to entrainment of broken trees in the flow, and (4) energy loss due to breaking and overturning of trees Kahrs (2015). For simplicity reasons, only phenomena one is considered in this study since there are too many variables to consider when physically modeling broken trees effecting flow. This problem would have to be tackled via computer simulation.

The main objectives of this experimental study is to answer:

1. Which observed hydrodynamic effects are present during avalanche flow through a given forest density?
2. In comparison with reference trials, which parameters influence avalanche rheology?
3. Which material type is applicable to replicate dry/wet snow conditions?
4. What occurs when the surface is previously coated in media. Is more material entrained or detrained?
5. What is the optimal relative humidity?

4.2 Experiment Design

4.2.1 Chute Orientation and Composition

The frame of the chute is composed of wood 2x4 beams which are situated in a fashion to prevent dynamic forces acting on the model Figure 4.2. To initiate the avalanche I had to pull on a tab to open the gate so the cross beams prevented swaying motion during trials and especially when dismounting the model. The baseboard of the acceleration zone is also composed of wood but sidewalls are made of plexiglas, Poly(methyl methacrylate). The baseboards for the forest zone is an aluminum compound and the sidewalls are also plexiglas. The smooth transition between the forest and runout zone is aluminum and leads into the wooden runout zone. The smooth transition from the forest zone to the runout zone resembles real world scenarios and prevents turbulent flows leading to runout. Essentially the model is of wooden, aluminum, and plexiglas composition. These materials were chosen specifically because they are positively charged at ambient conditions. The entire surface was covered with a urethane modified alkyd paint.

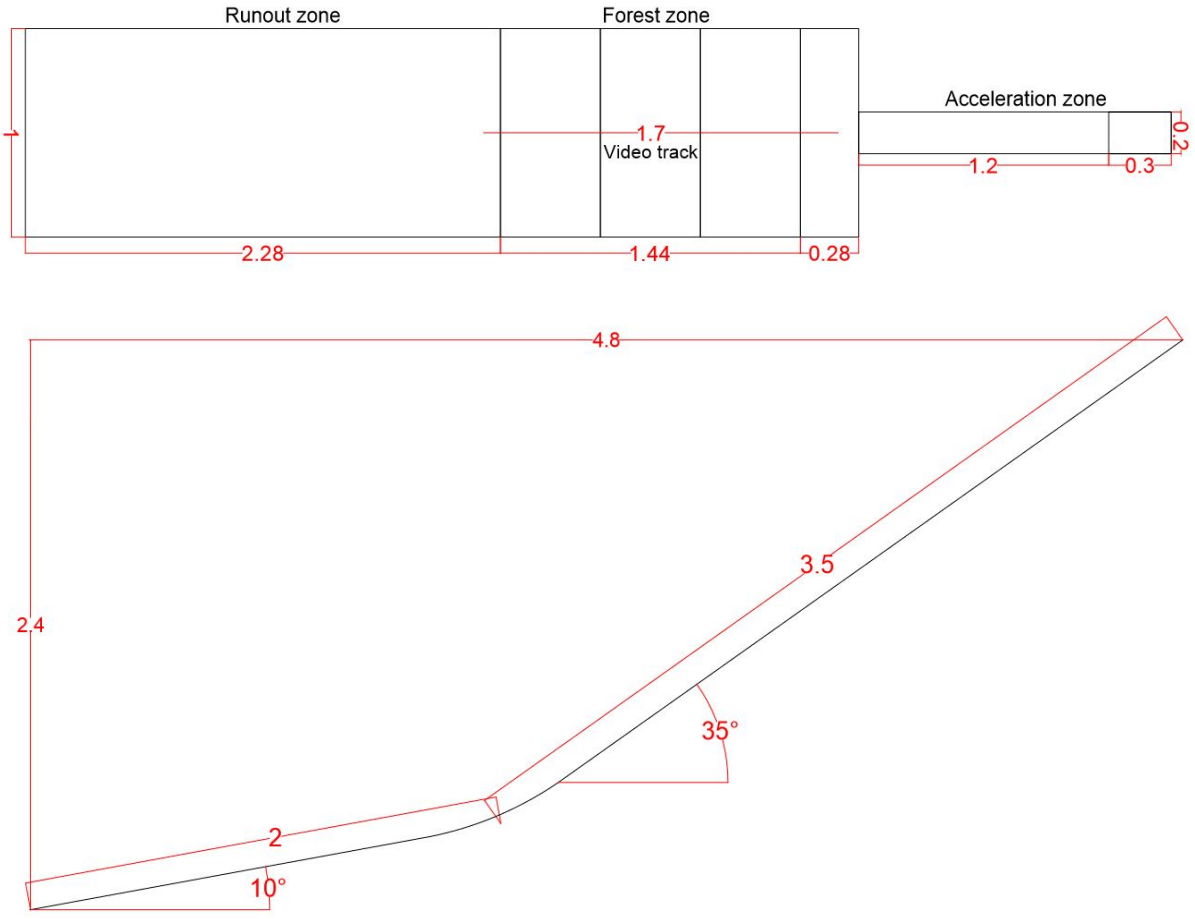

Figure 4.1: Chute design

4.2.2 Triboelectric Series

"Water flowing through tubes of different materials acquires positive charge whose magnitude is correlated with the materials' position in the triboelectric series. However, water acquires negative charge when flowing through air but its charge is modified by applying

an external electric field. Water is thus located at the top of the TS, between air and glass," Figure 4.1. Thereby, ballotini beads are suitable in representing water in this study since they are situated so close together on the Triboelectric table; furthermore, alumina is mostly composed of aluminum, by molar mass, which is also positioned just below glass.

Table 4.1: "Charge per mass acquired by flow electrification of water contacting with various materials, and charge per mass normalized by dividing by tubing internal area. Combined standard deviations are results from five independent experiments" (Burgo et al., 2016).

Material	Q/M (nC g^{-1})	(Q/M)/internal area (nC g^{-1} cm^{-2})	Sign
Air (50 mL min^{-1})	−0.0159 ± 0.0009	N/A	−
Air (5 mL min^{-1})	−0.0131 ± 0.0004	N/A	−
Glass	+0.0034 ± 0.0002	+0.0010	+
Aluminum	+0.0057 ± 0.0007	+0.0016	+
Stainless steel	+0.0279 ± 0.0017	+0.0079	+
Copper	+0.0261 ± 0.0011	+0.0074	+
Polystyrene	+0.0503 ± 0.0099	+0.0093	+
Silicone	+0.0645 ± 0.0018	+0.0099	+
PTFE (φ_i = 0.813 mm)	+0.1364 ± 0.0036	+0.0411	+
PTFE (φ_i = 1.321 mm)	+0.1988 ± 0.0098	+0.0369	+

In experiments centered around flowing powders, individual particles procure static charge during collision with boundaries. Thereby understanding this process is quite important with acquiring reliable data and being able to replicate experiments. Several studies have been reported, in which a single particle collides with a metal object then measuring the transferred charge (Matsusaka et al., 2015). An experiment by (Matsusaka and Masuda, 2003) and his team, of which is closely related to this study, utilizes a spherical single particle 100-300μm in diameter. The charge is quantified via Faraday cage after impact and a relationship was found between the impact charge and initial charge having a linear trend. The equilibrium charge is independent of the impact velocity but dependent on the material used. However, the impact charge is a characteristic charge, and it increases linearly with the impact velocity (Matsusaka et al., 2015). As a way to circumvent this from happening to my experiment, I wired the aluminum plates on the model to a grounding rod as shown in Figure 4.2. Each aluminum plate has four wires screwed into place which will relay the generated charge into one grounding rod. By incorporating this feature into the model, static charge generation was successfully dissipated. The charging process is well understood for metals and is attributed to the transfer of electrons from the metal to the accompanying material, or vice versa. With media flowing trough a total of 5185 aluminum 'trees', static dissipation was a key factor to reproducing experiments auspiciously.

Figure 4.2: Static discharge from 12 points of contact to the grounding rod.

In the triboelectric series, Appendix F, the higher positioned materials will acquire a positive charge when contacted with a material at a lower position along the series. Thus, the triboelectric series can be used to estimate the relative charge polarity of the materials (Diaz and Felix-Navarro, 2004). Ambient surroundings the material is subject to influences the overall charge in a manner where a higher charge is often found in vacuum compared to the atmosphere where static charge is reduced considerably when the humidity is high. For this reason the experiment is held in a clean room with relative humidity ranging from 50-70%. "The manner in which the collision occurs also influences the magnitude of the static charge. The contact can be a single (or multiple) contacts at a designated site on the surface of the material with no translational motion along the surface, or there can be translational motion, such as, rubbing or sliding. In the latter case, contact area is greater and other complications such as friction and physical or chemical damage may accompany the charge transfer" (Diaz and Felix-Navarro, 2004).

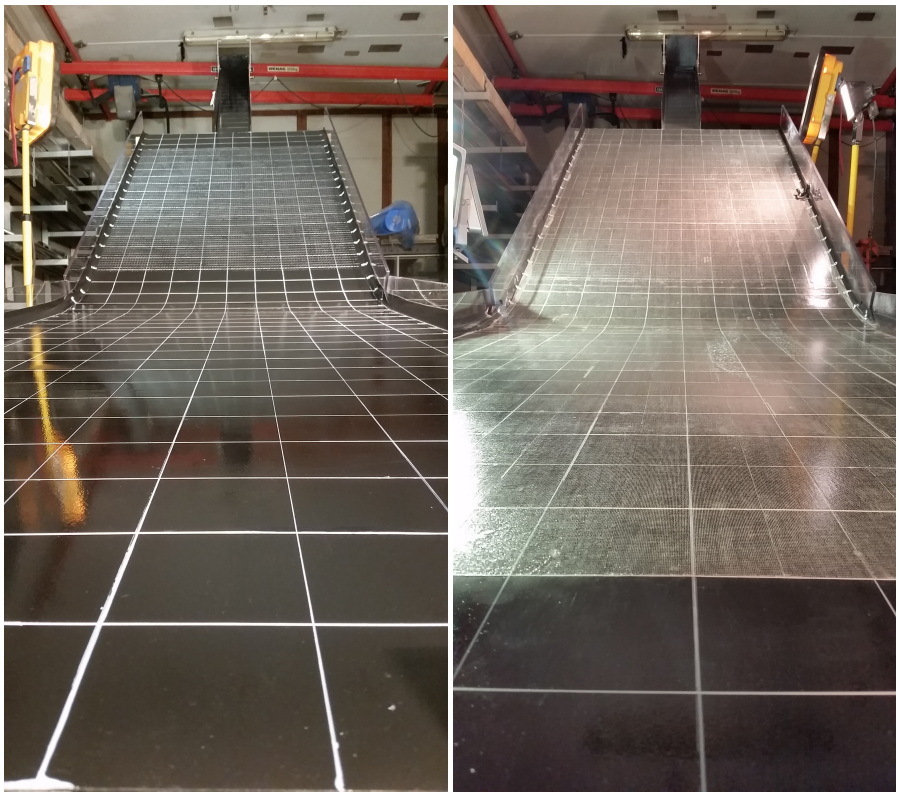

Figure 4.3: Polyethylene paint (left), Double-sided tape (right)

Since the charge transfer is an interfacial phenomenon, the chemical composition and surface roughness affect the charge (Diaz and Felix-Navarro, 2004). As a matter of caution, everything within the model is on the positive scale on the triboelectric series, Table 4.2 and Appendix H.1, H.2 and H.3. I have therefore painted the entire surface of the model in a urethane modified alkyd coating to resist opposite attraction and static electric generation. The applied paint is solvent based so having hydrocarbons within the solution, in theory almost no static charge should develop. Another measure in hindering static charge generation on the plexiglass was to cover the base with black electrical insulation tape (see Appendix I.1).

Table 4.2: Triboelectric series of material affecting experimental study. (Lee, 2009)

Insulator	**Charge affinity**	**Charge effect if rubbed by metal**	**Comments**
Solid polyurethane	+40	+Normal	Slightly conductive
Glass (soda) beads	+25	+Normal	Slightly conductive
Aluminum	+7 to +10	+Normal	Conductive
Wood	+7	-Weak	-
Polymethyl methacrylate	-10	-Normal	-

Another measure to decrease static charge potential is to cover the surface with double-sided tape (see Appendix I.2), Figure 4.3. In doing so, a thin layer (approximately one grain diameter film) of powder is stuck to the surface and enables the flowing avalanche to glide on top of itself thus maintaining the same electron affinity.

4.2.3 Equipment

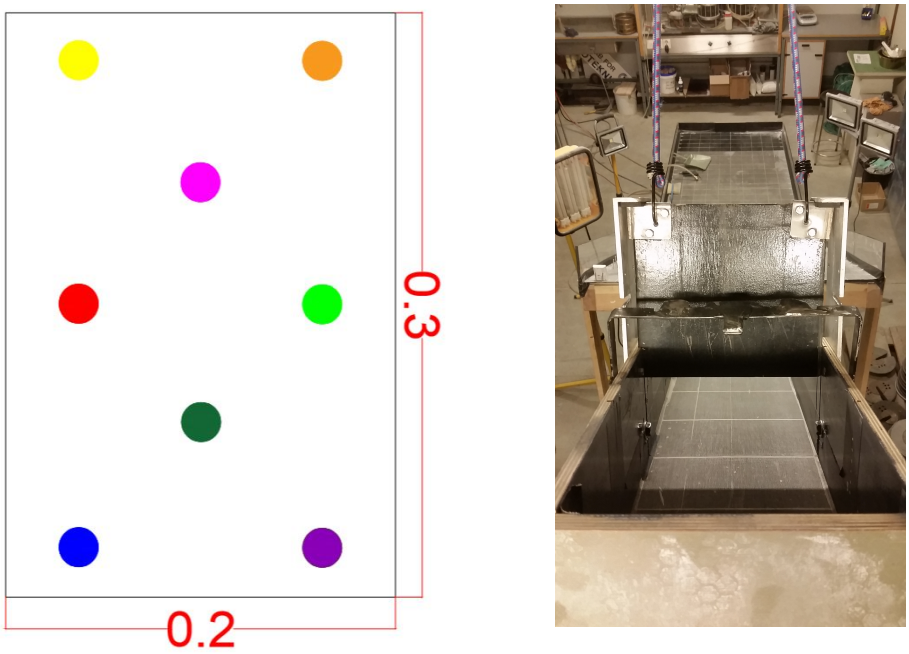

Figure 4.4: Bead orientation (left) and release mechanism (right).

Filming equipment consist of three GoPro cameras: One camera situated orthogonal to flow, the second situated parallel to flow and the third is located at the bottom of the acceleration zone to capture the initial flow height. GoPro's smart remote was utilized to control all three cameras simultaneously with a resolution of 1920x1080. The colored beads oriented as shown in Figure 4.4 were tracked at 120fps via an open source program Tracker. An average of two three beads actually make it through the forest into the runout zone, therefore a total of 8 beads are placed in the start zone. The release mechanism is triggered by a bungee system which initiates the failure at the same rate and same height of 10cm.

4.3 Forest Ratio and Density

Assuming trees naturally grow in a random fashion, the forest pattern is randomly generated via MATLAB code which initiated at 50% forest density and then worked backwards, removing a specified density from the 'r-vector' to reach 25% density. This random pattern, which is found in Appendix A generates points within a 144x97cm grid. Since the front velocity in previous experiments remained unaltered, spatial separation from tree to tree might have been too large. A study published by (Hákonardóttir and Jóhannesson, 2001) determined that increasing the number of narrow obstacles leads to greater reduction in runout distance than fewer, broader obstacles with the same surface area. Therefore, the ratio between the forest-stem area and overall flow area was not to the proper magnitude.

Figure 4.5: Cross section view of stems bent to vertical (left) and orthogonal view of 50% tree density (right).

In this experiment the ratio between stem area vs flow area was increased to 2% at 25% tree density and 4% at 50% tree density. The maximum ratio, 100% tree density, is equal to 8% of the total area. This equates to one tree stem (0.32cm diameter) per $1cm^2$ square since the maximum possible spatial separation from tree to tree is 1cm. Ecosystem responses to avalanches on the level of single trees are closely related to the size and flexibility of the tree and the spatial position of the avalanche origin relative to the tree (Bebi et al., 2009). Each tree stem in this experiment is aluminum and therefore considered perfectly rigid with no possibility of bending or breaking. At 50% tree density, total of 5185 aluminum stems were bent vertical to recreate actual tree growth and promote wedging of powder up-slope. Another positive attribute to bending the stems vertical was the degradation of particles deflecting to the suspension layer.

4.3.1 Material Types

In previous experimental studies on dry avalanche flow; powder, granular materials or a mixture of both have been used to replicate dry snow avalanches. Generally low density powders are used to model dry avalanche flow with an aerosol cloud (Bozhinskiy and Sukhanov, 1998). A multitude of other relevant experiments including a wide range of materials from 3mm glass bead to sucrose, (Lavoie et al., 2002; Gray et al., 2003), quartz, sand (Wieland et al., 1999; Iverson et al., 2004), gelatin (Van Riemsdijk et al., 2010) and 0.1mm diameter spherical glass beads (Hákonardóttir and Jóhannesson, 2001; Brateng, 2005; Hauksson et al., 2007; Kahrs, 2015). The experiment carried out in 2017 at NTNU laboratory utilized ballotini beads (SiLibeads) with a diameter $\leq 0.1mm$. Material properties of ballotini are provided in the table below along with an in depth material specification found in Appendix G. Since ballotini is considered non-cohesive, the internal friction angle of ballotini is assumed to be equivalent to the angle of repose.

Table 4.3: Ballotini characteristics including: Bulk density ρ, internal friction φ_{int}, static bed friction $\varphi_{bad,stat}$, and dynamic bed friction $\varphi_{bed,dyn}$ (Kahrs, 2015; Lavoie et al., 2002)

$\rho(kg/m^3)$	φ°_{int}	$\varphi^\circ_{bed,stat}$	$\varphi^\circ_{bed,dyn}$	**Carr's index (%)**	**Cohesion index**	**Flowability index**
1583	23-26	37-41	27-28	4	2.73 ± 0.13	1.09 ± 0.22

In this paper, avalanches are further divided according to moisture content as wet (alumina) and dry (ballotini) avalanches. Bases on provided flowability values along with cohesive properties, alumina shows promise in replicating slab avalanches since annotation of cohesive snow layer are regularly initiated by a failure at depth with regards to overlaying snow cover. Ballotini is the accepted as the material to replicate loose snow avalanches which initiate at a single point.

The angle of repose is determined to describe the powder's susceptibility to flow, thus providing a relative measure of flowability. It can be determined by pouring the powder into a funnel which is held at a fixed height above a flat base and measuring the angle formed by the powder's conical heap with a horizontal surface. Angles of repose under 30° point to powders with good flowability, $30° - 45°$ show some cohesiveness, $45° - 55°$ show true cohesiveness, and anything above 55° is considered as having very high cohesiveness and limited flowability (De Campos and Ferreira, 2013).

Table 4.4: Alumina characteristics includeing: Bulk density ρ, internal friction φ_{int}, static bed friction $\varphi_{bad,stat}$, and dynamic bed friction $\varphi_{bed,dyn}$ (De Campos and Ferreira, 2013)

$\rho(kg/m^3)$	$\varphi_{int}x^\circ$	$\varphi_{bed,stat}x^\circ$	$\varphi_{bed,dyn}x^\circ$	**Angle of Repose (x°)**	**Hausner Ratio**	**Flowability index**
930-1000	32-36	41	29	32-36	1.38	3.3

Although the materials have the mass (4kg), the volume is quite different. The volume of ballotini is equal to $3000cm^3$ and alumina is equal to $4200cm^3$. Alumina has also been sieved to $\leq 100\mu$m particles as a consequence, the distribution of particles causes irregular shape and angular morphology. Reducing the size of the particles can reduce flowability because the particle's surface area per unit mass decreases and generates a larger surface area for the surface's cohesive forces to interact (De Campos and Ferreira, 2013). Irregularities in their shape cause considerable interlocking among the particles and increases their resistance to flow, while their roundness reduces the interparticle's forces and improves their flow properties (Mohammed et al., 2011).

Characteristics indicated in Table 4.4, verify that the alumina is moderately cohesive (HR between 1.25 and 1.40). Since the determined 'Hausner Ratio' value of 1.38 is at the boundary between cohesive and medium flow behavior one can expect this material to possess free flow characteristics along with an aptitude toward cohesiveness(cohesive powder with HR over 1.40).

When two particles come in contact, they are subjected to capillary, electrostatic, and van der Waals forces (Castellanos, 2005). The angle of wall friction represents the adhesive strength of the powder and the wall material. The larger the value of the $\varphi_{bed,stat}x^\circ$ is, the more difficult is to move the powder along the wall's surface.

Certain powder characteristics such as particle size, morphology, surface area, absolute density and distribution, modify the flow behavior of powders (Schweder and Shulze, 1990). Powder moisture content usually has a significant impact on powder flowability, as the liquid bridges and capillary forces acting between powder particles lead to reduced flowability (Scoville and Peleg, 1981).

4.3.2 Relative Humidity

Environmental factors such as relative humidity and static electricity, will naturally influence flow regime. By standardizing parameters such as moisture and static electricity, the study of powder avalanches was able to differentiate the flow behaviors of various experiments (Lavoie et al., 2002). In this experimental study we utilize this standardization by differentiating relative humidity and maintaining a constant value of 50%, 60% and 70%. A limitation of relative humidity to a range between 30-70% has been applied to minimize electrostatic cohesive forces in a granular avalanche model before (Iverson et al., 2004). By gradually increasing relative humidity within the environment, the supplementary surface tension allows one to adjust flow properties in a precise modus operandi to ultimately stabilize and control flow parameters.

4.4 Parameters Measured

4.4.1 Surface and Front Velocity

An important factor in measuring velocity is to impose a grid system on the chute that is visible on the camera. Since the powders are white, painting a matte black tone over the chute caused the powder to appear in a sort of 3D effect. The grid was painted in a metallic white and allowed the viewer to observe a clearly defined front as it flowed down the chute. The distance between markings was 2cm through the forest and 10cm on the acceleration/runout zones.

Surface velocity was measured in the same manner as front velocity via Tracker software. Since the camera was mounted orthogonal to the flow path 4.1, vertical and lateral movement could be clearly defined. The avalanche motion was analyzed frame by frame in order to track flow characteristics. To maintain a sense of order while calculating surface velocity, the orientation of beads seen in 4.4 were the placed in the same position for each trial. The beads were tracked frame by frame on a x,y,z coordinate system as the moved through the forest. To visualize the flow, follow the link provide for better visual representation given in Appendix I.3. However, the open source program Tracker must be utilized to observe the videos. It is free and available under the link given in Appendix I.4.

4.4.2 Runout Distance

The runout zone is oriented at a 10° to horizontal and increases to 35° through the transition zone, therefore the runout zone starts at the base of the forest zone. Reasons for the runout lapsing into the forest zone was to maintain a constant area to measure mass passing through the forest zone. The runout distance was measured to a precision of 0.5cm from the base of the forest.

Figure 4.6: Alumina reference trials showing blown-up runout distance alongside the chute view.

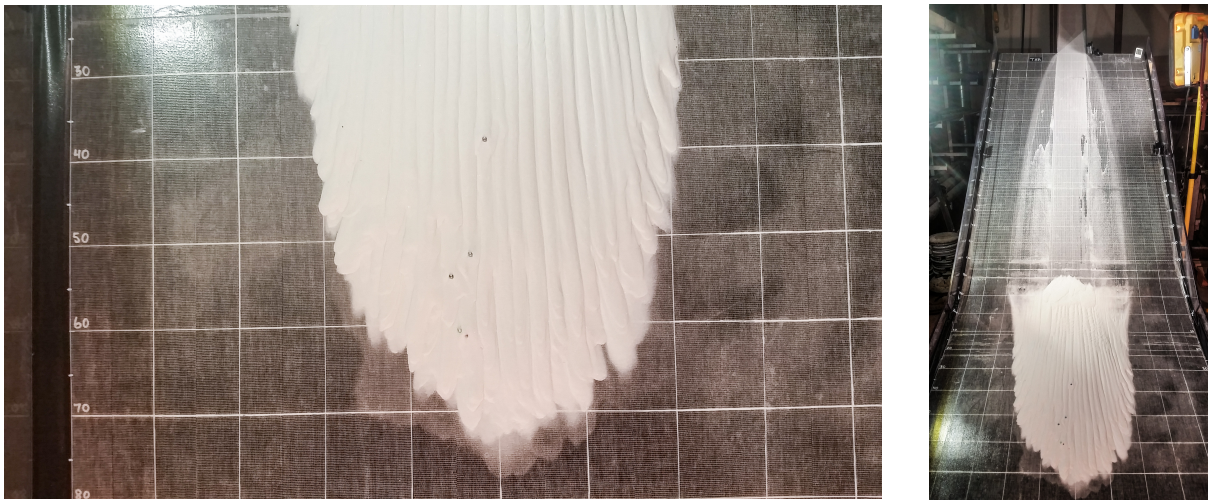

Figure 4.7: Ballotini reference trials showing blown-up runout distance alongside the chute view.

Every so often the runouts had 2 fronts for which the maximum distance was recorded. As displayed in Figures 4.6 and 4.7, the two material types resulted in distinctly different runout distances. The change in runout distance, 50 cm average, for the reference trials were comparatively different. The reference point at the center of the forest had a minor impact on the flow regime, I assume no more than 0.5cm shortening occurred. The reference point was in place for every recorded trial to maintain consistency.

4.4.3 Flow Height

The initial location to measure flow height is located at the base of the acceleration zone. A scale was drawn on the sidewall of the zone, illustrated in Figure 4.8. The other locations are spread throughout the forest zone. The layout of these ten points are oriented 45° to the left and right of the exact center of the forest. For a better representation of the exact locations of these points, refer to Appendix B. At the cost of exact runout distance, a reference point was in place for all trials, including reference trials. The scale throughout the forest was to inscribed to every 5mm with an accuracy within ±1mm. Values were measured on the extreme edges (minimum flow height), the center(maximum flow height), and the initial flow

height above the forest. These values were compiled into one average flow height Appendix I.3.

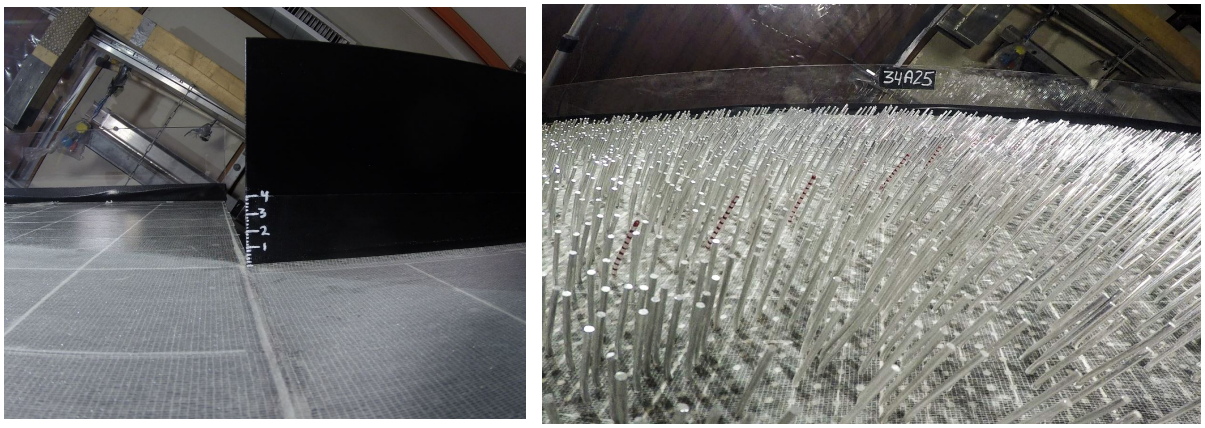

Figure 4.8: Flow depth inscribed on the sidewall of the acceleration zone (left) and 10 trees to scale flow through forest (right).

4.4.4 Deposition Wedge Height

Deposition wedge height proved to be a auxiliary reference to flow height since the powder stuck to the tree stems at an analogous height. The wedge height was subject to material type, tree density and mean velocity. This height was measured manually with a ruler at specific locations along the flow path. The locations chosen throughout the forest zone started at the top (30cm), upper middle (50cm), middle (100cm) and bottom (170cm). In general, the jamming was relative to the flow height and extended up-slope approximately 1cm to the tree above. This effect was magnified when trees grouped together. 3.4 provides an effective depiction of this jamming effect of single trees versus tree groups.

4.4.5 Mean Deposition Height

The mass flux of wedge height blended into mean deposition height toward the forest front and runout zones. Thereby, the mean deposition height is regarded as the detrained height left behind on the surface. This value increased with escalating relative humidity and is intrinsically dependent of forest structure and material type. The film height was measured at 100cm and above the forest where the initial flow height was observed. Appendix D displays the difference in mean deposition height throughout the avalanche flow path.

4.4.6 Deposition Mass

The deposition mass is essentially the material that did not reach the runout zone. The mass was calculated by subtracting the mass which flowed into the runout zone by the initial 4kg. Each material type and relative humidity produced differing values. The higher the humidity the larger the deposition mass. This value is a key factor in determining the loss of momentum and provides a quantitative value to the braking effect of forests on avalanches.

4.4.7 Width

Lateral expansion is a key factor in slowing down flowing mass. As particles are deflected laterally, the momentum is shifted and reduced. The boundaries of the flow was observed at the end of each experiment and then recorded for analysis. The width the powder detrained

through the forest section was of special interest since these values proved to correlate with forest density and relative humidity within the environment.

4.5 Experimental Procedure

A total of 70 experiments were conducted for which 62 were recorded and analyzed. The trials in which the data could not be used had half the chute covered in trees and the other half a smooth surface. These trials were for personal observations in seeing the braking effect of the forest first hand. It soon became clear that the forest has a major effect on braking avalanche flow. The ballotini trials at 50% humidity had an extensive amount due to the fact of checking for experimental repeatably. Once a thin layer stuck to the surface, the return value after the trials equated to an average loss of 5 grams per trial (0.125%). In order to satisfy a meticulous reference experiment ($\leq$ 0.2% error), a total of 20 reference trials were performed (14 ballotini and 6 alumina). In this circumstance, error was determined by comparing the the initial mass and recovered mass after each trial. Since gelatin is neutral, it appeared to be a viable powder to test for avalanche since it is also compressible, adhering, and has a similar rheology to powder avalanches. The problem with gelatin was that it was not repeatable since relative humidity tampered with the samples purity and started to accrue large balls. There were also ten trials testing for avalanche entrainment but the values were not reliable so the data has been discarded. The program in full is given in table 4.5, also in depth analysis provided in D.

% Forest	Ballotini		Alumina		Gelatin	
	RH	Trials	RH	Trials	RH	Trials
0%	50.00	10.0	50.00	2.0	50.00	4.0
	60.00	2.0	60.00	2.0	60.00	0.0
	70.00	2.0	70.00	2.0	70.00	0.0
25%	50.00	3.0	50.00	2.0		
	60.00	2.0	60.00	2.0		
	70.00	4.0	70.00	2.0		
50%	50.00	2.0	50.00	2.0		
	60.00	2.0	60.00	2.0		
	70.00	3.0	70.00	2.0		

Table 4.5: Test Program

This experimental study followed a protocol according to a particular sequence. Since humidity is a driving factor in attaining data for this exercise, I would start with controlling the environment. The room which the chute was held had a strong draft at the early stages of this study. To combat an this ever changing environment, from $-10C^\circ$ at 10% humidity to $15C^\circ$ at 100% humidity outside, a clean room had to be constructed. The entire room was sealed with visqueen plastic which essentially air locked the environment. Once this was established, the experiment could commence. To satisfy a certain threshold of ridding the chute of static electricity, I assumed a constant minimum relative humidity of 50% would be adequate. This is achieved with help of a humidifier purchased from Clas Ohlsen (see Appendix I.5).

Now that the humidity is set to the desired value, the next step is to sieve the powder with an earthen brass sieve. Brass was used for it's inherent conducting abilities to take in electrons via charge sharing and neutralize the ballotini beads and alumina. Sieving the

media also allows the humidity in the air to infiltrate the particles which is also effective in electrostatic dissipation. The total mass of 4kg would run through the sieve multiple times at the desired humidity before trials begin. Afterwards, to further limit static generation, a compressed air-gun was used to blow powder away from the forest and into the runout zone where it was brushed into a metal container via carbon fiber brush for weighing.

Chapter 5

Results

This section is an in-depth review of the results attained within this experimental study, which has been explained in the previous chapter. Observed avalanche rheology is supported for selected parameters with background information such as graphs, charts or images. This analysis provides insight into how forest density, humidity and material properties affect avalanche flow. The raw data for this experiment is provided in Appendix D in full detail. Videos of chosen trials can be found here Appendix I.3. A snapshot sequence of forest density, humidity and material type is available in Appendix I.3, along with a sequence of 25% forest vs. no forest. Runout snapshots are available for viewing in Appendix C.

5.1 Elucidations of Avalanche Flow

5.1.1 Interpretation of Flow Characteristics for Different Materials

A comprehensive elucidation of material properties previewed in Section 5.3.1 is summarized in accordance with observations taken throughout the study. To best describe the phenomena affected by altering the materials is to describe the reference trials rendered before trees affecting flow. Firstly, the average change in runout distance was 50cm so flowability is quite dissimilar. Initially the avalanche flows in a sort of oviform shape from the start to the end of the 'forest zone'. After the avalanche has ran its course, the shape of material deposited can be describes as an elongated bell where lateral expansion is immediate after departing the acceleration zone then gradually levels out until the runout zone where an increase in lateral expansion occurs due to the flattening slope. The shapes for both materials are nearly the same dimensions, after all, the mass is a constant 4kg. For ballotini the maximum change in width from top to the bottom of the forest zone is approximately 30cm to 53.5cm and for alumina the change in width is 30cm to 43.3cm; therefore, alumina is more cohesive and does not expand to the same degree as ballotini. It becomes apparent that ballotini is a good representation of a dry-cohesionless avalanche, where alumina is better described as a wet-slab avalanche.

Furthermore, the distribution of particles within alumina are considered irregularly shaped and have more angular morphology compared to ballotini. Since alumina has also been sieved to $\leq 100\mu$m, the particle's surface area per unit mass decreases and generates a larger surface area for the surface's cohesive forces to interact (De Campos and Ferreira, 2013), thus reducing flowability. Irregularities in their shape cause considerable interlocking among the particles and increases their resistance to flow, while their roundness reduces the interparticle forces and improves their flow properties (Mohammed et al., 2011).

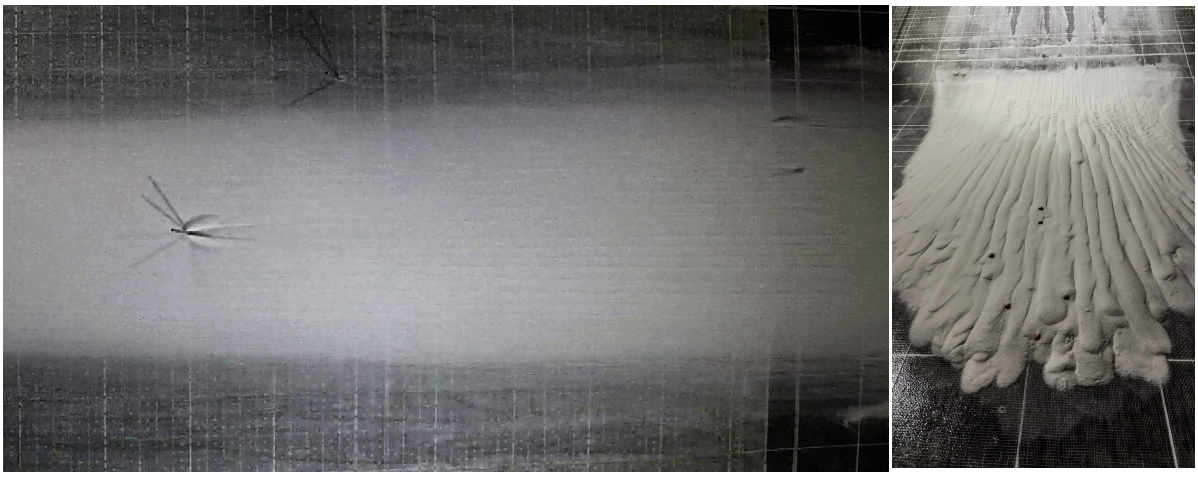

Figure 5.1: Flow instability of ballotini down 'forest zone' (left) and zoomed in fingers over the runout zone (right).

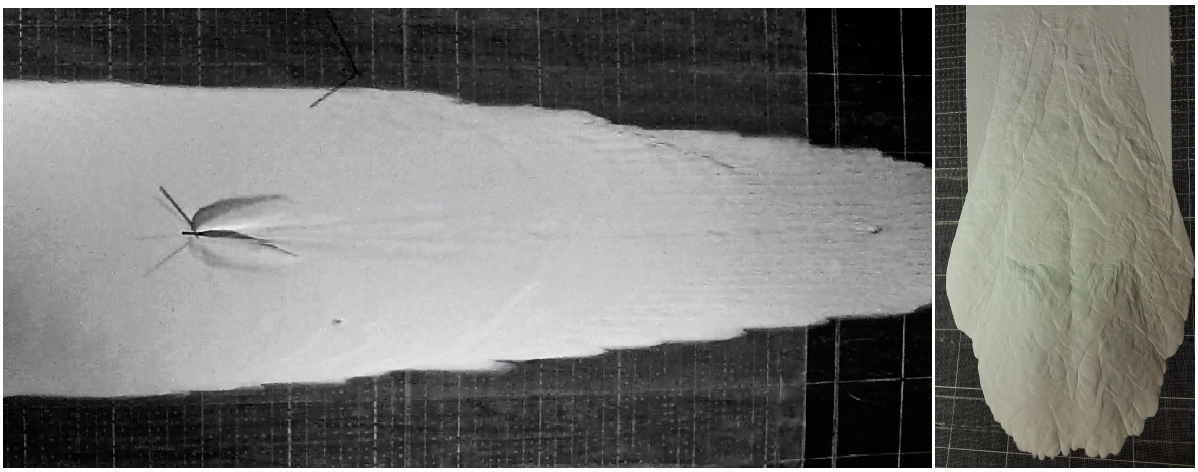

Figure 5.2: Flow instability of alumina down 'forest zone' (left) and zoomed in fingers over the runout zone (right).

Gravitational fingering can be observed under a variety of conditions. It is affected by the dependence of densities on composition. With adverse density ratios or mobilities as triggers, gravitational fingering is related to flow instabilities in porous materials (Moortgat, 2016) and to particle segregation effects in granular materials (Drahun and Bridgwater (1983), Savage and Lun (1988) and Pouliquen et al. (1997)). Pouliquen et al. (1997) describes this instability as a propagation effect in a granular medium on a rough inclined plane. The initially uniform front breaks up and forms the observed finger features. Other than for viscous fingering, the instability observed in granular media is not driven by surface tension, but by grain size segregation with flow propagation (Pouliquen et al., 1997).

The fingers observed in this project (Figure 5.1 and 5.2) are curved smoothly, while they stretch out relatively straight. They are further rather long compared to their width and height. For ballotini, it's not possible to see the ridges until half of the mass has reached the runout. Maybe a reflection of light makes it not possible to see. The image has filters to enhance the ridges. This characteristic is completely opposite for alumina where the formation of ridges is discernible at the front so flow instabilities in alumina occur at higher velocities.

5.1.2 Interpretation of Flow Characteristics for Altering Relative Humidity

As water molecules penetrate between the medium, liquid connections known as capillary bridges form and lock particles together. The additional tension forces create a pseudo-attractive force between the grains that is essentially absent in dry ballotini. The addition of minuscule amounts of water via humidity in the air, greatly increased the grains' ability to adhere to one another; as a result, the particles accrue together at steeper angles thereby increasing the angle of repose. As the particles becomes more saturated, a stable connection between the liquid and solid media is sustained via surface tension. A hierarchy of such contacts has been shown to cause agglomeration of drying colloidal particles into geometric clusters (Manoharan et al., 2003). The main qualitative conclusion from capillary bridge studies is that the tensile strength as function of liquid saturation may have a maximum, "despite the fact that the strength of a single pendular bridge between two particles decreases monotonously with increasing volume" (Mitarai and Nori, 2006). Though, depending on the material used, the exact point of this maximum varies widely between media and can even disappear in some circumstances.

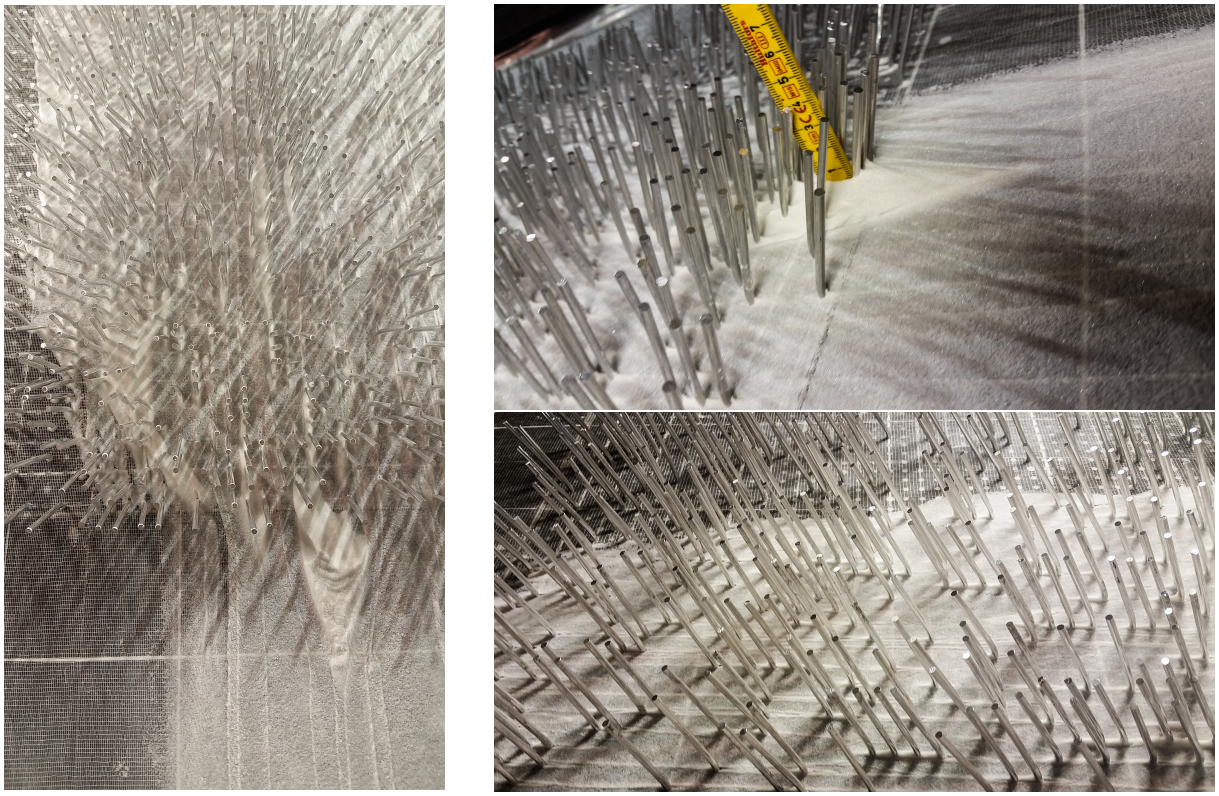

Figure 5.3: Plugging of ballotini at forest front (left). Nearly 5mm of deposited material stuck above the forest(upper-right). cross sectional view of streaks left behind due to plugging(lower-right).

Figure 5.4: Wedge shaped deposition stuck at the forest front(left). Cross sectional view of the plugged ballotini (upper-right). Scale of deposition height approximately 30mm (lower-right).

Powder moisture content usually has a significant impact on powder flowability, as the liquid bridges and capillary forces acting between powder particles lead to reduced flowability (Scoville and Peleg, 1981). This force has proven to be is specifically useful in regard to ballotini since this material is considered cohesionless when dry. At 50% relative humidity, the friction approach is the best method to accurately measure the flow through a forest.

By gradually increasing relative humidity, the additional surface tension makes it possible to adjust flow properties in a targeted demeanor, essentially to stabilize and finally control flow parameters. As depicted in Figures 5.3 and 5.4, it becomes apparent that rheological characteristics, ie flow properties, of the suspension change significantly with water content: a thin, weakly elastic suspension becomes a gelatinous structure with strong elastic properties. As the second phase fraction increases, yield value and viscosity increase by several orders of magnitude (Koos, 2013). At 70% relative humidity, the detrainment approach is best utilized since large volume is released at the forest front

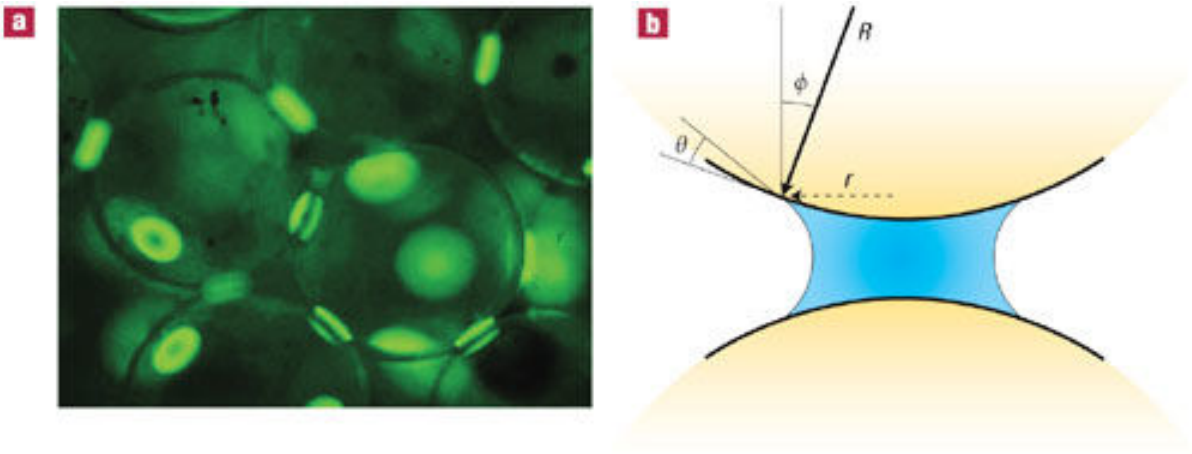

Figure 5.5: Liquid bridges form at the point of contact between grains, as a result of surface tension. a) Fluorescence microscopy image of liquid bridges between 375μm diameter glass beads. b) Schematic of a liquid bridge (blue) between spherical surfaces (yellow). θ is the liquid–solid contact angle, ϕ is the half-filling angle, defined as $\phi = arctan(r/R)$, where r is the radius of the liquid bridge, and R is the radius of the grain (Kudrolli, 2008) From: Taylor and Francis (2005).

The simulation results are consistent with previous experimental observations and reveal interesting phenomena such as the existence of a maximum in the tensile strength of a wet granular medium as function of liquid saturation (Grof et al., 2008). As indicated in Figure 5.5, the fruition of such computations indicate that the liquid bridge force depends significantly on the separation distance, the volume of the liquid bridge, the ratio of sphere radii and the contact angle. Specifically, the force of the liquid bridge increases with decreasing contact angle and with decreasing difference between particle sizes (Grof et al., 2008).

X-ray microtomography was used in Figure 5.5 to quantify the distribution of wetting liquid within an assortment of glass beads. To enhance contrast between the solid and liquid phases, aqueous zinc oxide has been utilized as the liquid. From the measured liquid structure, they identified the volume that was in contact with more than two beads Figure 5.5. As the liquid content increased, it was found that simple liquid bridges between particles merged to give rise to a hierarchy of polyhedral structures, starting with trimers, tetrahedra and pentamers (Kudrolli, 2008), Figure 5.6.

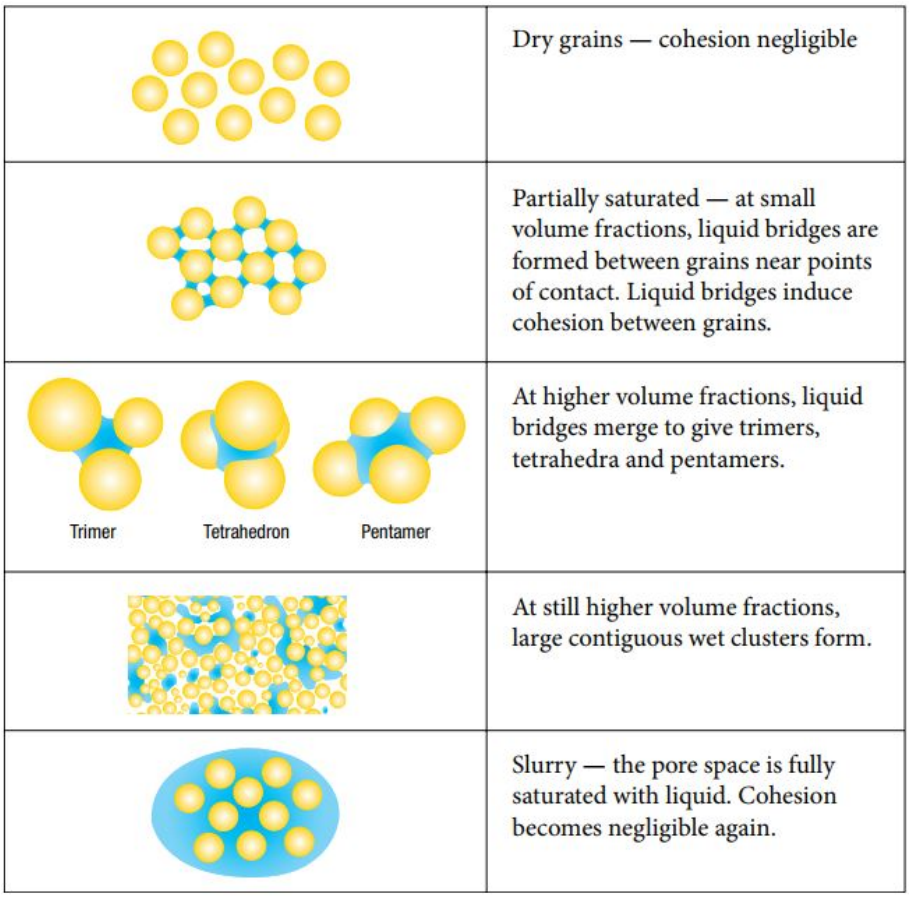

Figure 5.6: Schematic diagrams showing the differing degrees of wetting in granular matter. Dry grains and a fully saturated system have no cohesion between particles. In between these states, cohesive forces are present between grains. (Kudrolli, 2008)

By ridding static electricity with lubrication, the repercussion can cause wet grains to flow more freely compared with dry grains; subsequently, offsetting the stability gained by grain cohesion. X-ray microtomography may be applied to slow-flowing, wet granular matter to clarify how the grain–liquid–air interfaces interact and break as grains flow past each other, and while cohesion, lubrication and pore pressure compete (Xu et al., 2007). The investigation by Herminghaus and colleagues highlights the importance of geometry and surface tension, making sticky matter more tractable (Herminghaus, 2005). As the wetting transition increases, the forces change, and a drag force is introduced when saturation is greater than 35%.

With respect to this experimental study, the pendular state is of special importance because the increase in shear strength due to surface tension causes ballotini to stick the surface and act similar to snow sticking to surfaces as an avalanche flows by. Liquid forming a meniscus leads to intense attraction forces compared to gravitational forces, thus simulating snow with more reliability. Such interparticle forces are presented in Figure 5.4, where the overlaying of fingers within the deposition is quite different with regards to a 20% increase in relative humidity.

Figure 5.7: Ballotini at 50% (left) and 70% relative humidity (right).

Interpretation of flow characteristics for altering forest densities

Tree grouping is the largest contributing factor in detrainment of material. Feistl and his team show grouping in a horizontal fashion (Chapter 3, Figure 3.1) with nonuniform distance between tree stems; however, in this experiment the distance between trees is uniform so wedging with this alignment is not as effective as bulk grouping and vertical grouping. The materials used in this experiment, specifically ballotini, require deceleration via fanning to form wedges so the material passes through horizontal grouping relatively unhindered. As depicted in Figure 5.8, the two types of tree grouping for altering tree densities is presented.

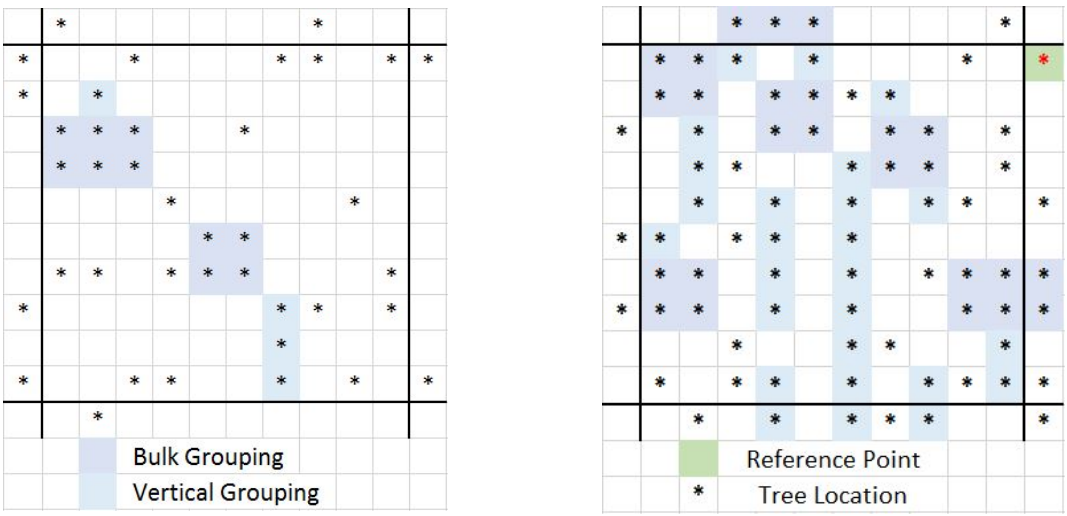

Figure 5.8: Randomly chosen grid to represent grouping at 25% tree density (left) and 50% (right).

The magnitude of avalanche deceleration for different forest density quickly became apparent after an experimental trial where 25% tree density was installed versus a smooth (reference) surface, Figure 5.10. As presented in the figure, the change in runout distance is nearly 50cm and also forms an entirely different form of deposition.

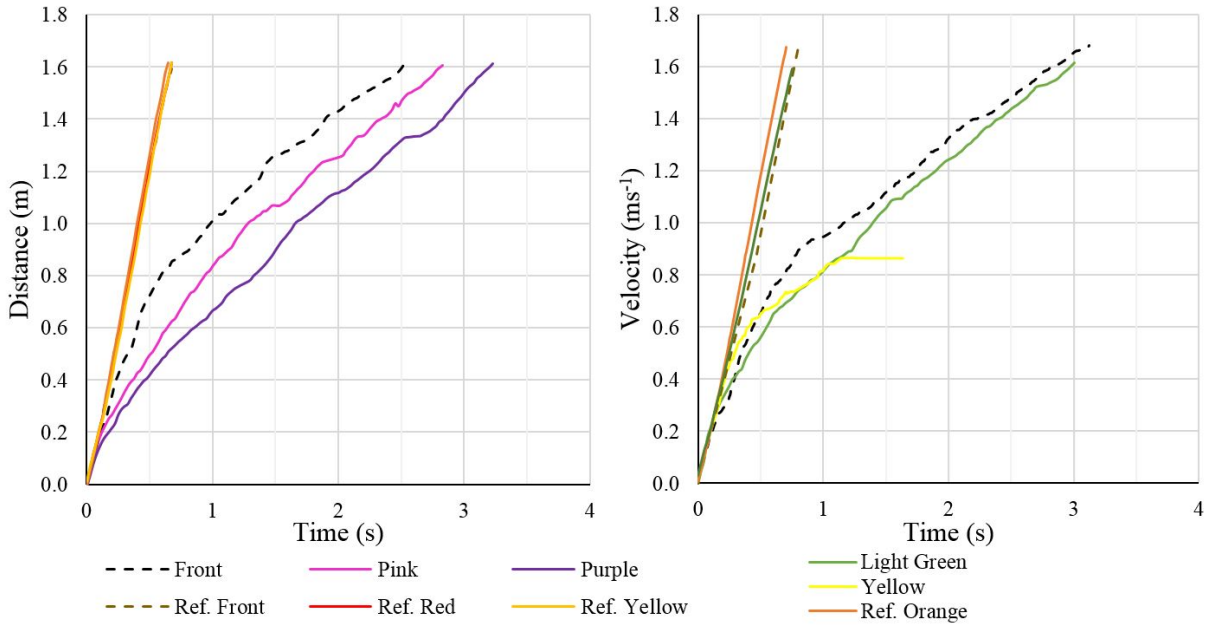

Figure 5.9: Diagram of ballotini flowing through 25% forest at 50% relative humidity showing the change in surface/front velocity between forested and unforested terrain.

As seen in Figure 5.9, the change in velocity is provided by the inclination of the slopes for they depict the change front and surface (bead) velocity between the forested and unforested terrain. The data presented here is not considered relevant and is separate from data presented in the next chapter because the material flowing through the forest seemed to funnel into the unforested terrain. To simplify this problem, faster moving parts of the flow correspond to areas of lower pressure. When the fluid-like material flows on top of the surface, the pressure in the two sides of the chute will differ, forcing the media away from the forest to the "low pressure" side. This effect is also apparent on the right side of Figure 5.10. The right half of the image shows deposition volume of ballotini where there is larger forest density. The region with 50% forest density (right half) extracted much more mass from the avalanche flow compared to the 25% forest region (left half).

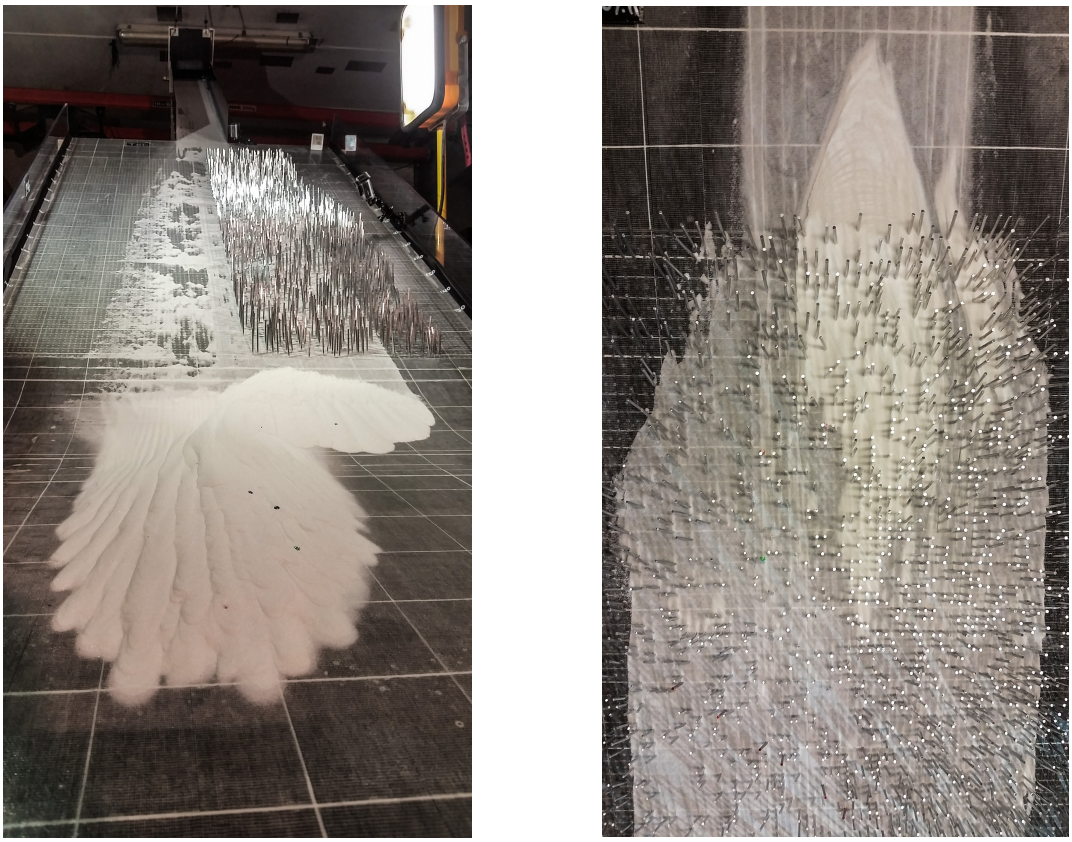

Figure 5.10: Reference test with 0% forest and 25% (left). Visual representation of 25% vs 50% forest density (right).

With the intention of randomizing the model, bending every tree within the forest to vertical became a positive attribute in dispersing material evenly for which resulted in slowing the front velocity considerably. The time required for material to flow into the runout increased exponentially with ascending tree accumulation. Another observation is the effect this action had on media flowing into suspension.

5.1.3 Interpretation of Flow Characteristics for Different Surface and Incident Front Velocities

This section describes observations made in the lab which were previously summarized in Section 5.4.1. The change in avalanche motion and related phenomena is evaluated based on forest density, material type and relative humidity of the environment for velocity is intrinsically dependent on these parameters.

Reference Trials

The average change in lateral expansion between the material types as approximately 10cm at eh bottom of the forest. This observation shows insight into which material properties are affected most by particle shape, cohesion and bed friction. These innate characteristics determine how the media flows down the chute and becomes evident when comparing the velocity of the flowing media. In general, the alumina takes twice as long to flow to the bottom of the chute as the ballotini. As expected for both materials, the amount of volume release became greater with escalating humidity. However, the flow height of ballotini decreased with increasing humidity where the flow height of alumina increased with escalating humidity.

In order to analyze flow height of these initial trials, two reference points were placed in camera view to determine maximum and minimum flow height. The image in Figure 5.11 shows the reference point with maximum flow height. The significant aspect in this figure is the presentation of the change in momentum of the avalanche. At a closer look, the material rebounds up-slope by approximately 10mm after colliding with the vertical tree stem essentially decelerating the particles.

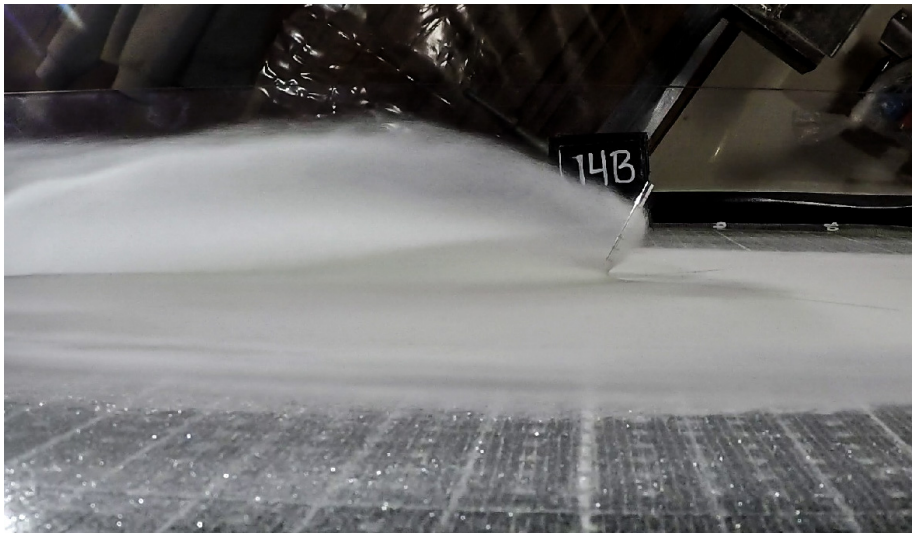

Figure 5.11: Loss of momentum

Forest Trials

For the experiments implementing a given forest density of 25% and 50%, the flow regime appears to be similar for all trials: the front velocity remains constant until about half way down the forest zone where it halts and then accelerates again when the bulk flow catches up. At the start of the forest the media is diverted into fans causing lateral expansion upwards 40°. The fans are largest at the front row of the forest. Eventually the plugged material at the forest front causes a point of diversion where the media is redirected to the outskirts of the forest, Figure 5.4.

For both forest densities, the ballotini gradually increased width as the material glided down-slope. This was not the case for alumina. At 25% forest density, alumina's width increased by approximately 3cm from about 30cm in the forest to the start of the runout. At 50% forest density, alumina's lateral expansion decreased by an average 3.7cm from top to bottom. Also, the material is wedged into the initial 30cm of forest at a greater rate, which causes the powder to settle and glide down the chute, rather than bouncing.

When colliding with a tree, the media is forced to climb up the tree before the particles can be redirected outwards which develop fans. An observed characteristic of forest density at 25% is that material carries more momentum and is deflected into suspension which causes the flow density to decrease since the flow regime is translated into saltation. As the flow depth at each tree fluctuates is more dependent on the forest orientation and velocity than humidity. As observed from the camera analyzing cross sectional area, the mass is wedged on the tree surface into a crescent-shaped body as the material flows around the stem. This effect is dependent of the velocity of the dense-flowing core of the avalanche. At higher velocity the crescent shape increases in height. Please see Figures 4.6 and 4.7 for the reference trial runout characteristics.

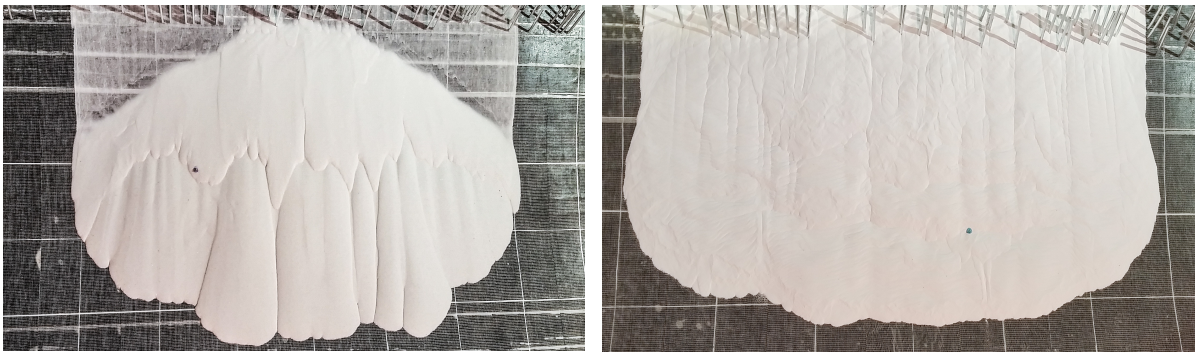

Figure 5.12: Ballotini (left) and alumina (right) at 25% forest density.

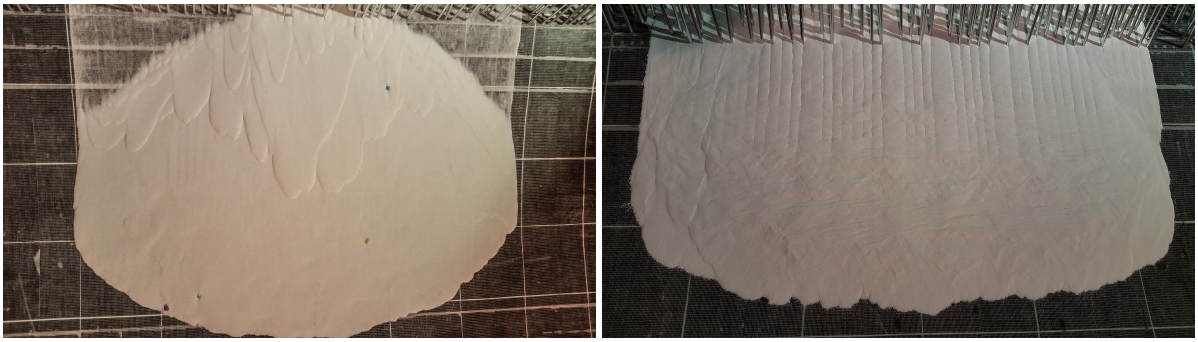

Figure 5.13: Ballotini (left) and alumina (right) at 50% forest density.

As the increasing forest density restricts saltation of the particles in motion, they begin to decrease velocity and undertake a gliding motion instead. At this point, the critical angle of inclination where the dispersive pressure becomes greater than the overburden pressure (Norem et al., 1987) is nonexistent. There is a reversal in forces and the dispersive pressure becomes smaller than the overburden pressure, as a result the buildup of media in the runout zone smoothens out reducing fingers (Figures 5.12 and 5.13).

Figure 5.14: Suspension of the first 30cm

As observed in Figure 5.14, the suspension layer was present in the first 30cm of the forest. The frame width is from midway through the forest to the forest front and show the effect bending the tree stems has on limiting suspension. It is difficult to see in Figure 5.14,

nonetheless the avalanche front is already passing the midway point and has no depiction of material bouncing in the suspension layer while passing through the forest. Another interesting observation is the suspension layer persists for a longer duration with higher humidity. The size of the wedge formed at the forest stand changes from 50% to 70% humidity and acts as a ramp sending material air-born. As seen in Figure 5.4 the tree wedge height is at 30cm orthogonal to flow, limiting the surface area of the forest is the driving factor in limiting suspension propagation.

5.1.4 Summary of Observations

To recapitulate observations made throughout this experimental study, avalanche flow is governed by specific characteristic phenomena: Firstly, gravitational fingering is a product of material densities which caused a propagation effect on the granular material while flowing down a rough inclined plane. For ballotini, the front is uniform and breaks up to form fingers as the particle settle in the runout. This is the opposite for alumina which the front breaks up, segregates and an overlaying powder fills in the trenches and smooths the deposition.

Secondly, as surface tension increases with escalating relative humidity, a thin film of material is left behind. This increased deposited height was proportional to the humidity by a factor of approximately one bead for every 5% increase in humidity. This force undoubtedly altered the momentum of the avalanche flow by removing mass. Even without a forest present, the increased humidity caused a size-able difference in runout shortening. This force is enhanced when particles collide with tree stems plugging material into a wedge.

Thirdly, the deceleration via fanning is an important phenomenon in immobilizing flowing mass and compressing the media into plugged wedges stuck behind tree stems. As depicted in Figure 5.8, the two types of tree grouping for altering tree density is directly affects the amount of mass deposited. For tree grouping is the largest contributing factor in detrainment of material.

Lastly, with the intention of randomizing the model, bending every tree vertically proved a positive attribute in dispersing material evenly resulting in the deceleration of the front. In doing so, duration for material to flow into the runout increased exponentially with ascending tree accumulation. The change in tree stem orientation along with the randomized pattern drastically reduced the length at which the media flows in saltation or tossed into suspension.

5.2 Data Analysis

5.2.1 Relative Humidity

Humidity has played such a major role in this study such that each phenomenon explained below is subject to altering humidity within the controlled environment. The experiments test characteristic phenomena of the two materials at 50%, 60%, and 70% relative humidity. The observations previously described will now have figures and tables for increasing forest density along with altering relative humidity.

5.2.2 Surface and Front Velocity

Time vs. Distance

Figures 5.15 to 5.26 shows profiles of the front velocity and surface (bead) velocity of the avalanche travelling through the forest zone of the chute. Each profile shows the slope of time vs. distance and time vs. velocity of reference experiment along with the front and

surface velocity trends. There is a clear trend in the measured velocities along the chute. As depicted in the figures below, the reference velocity has a steep inclination for distance versus time. The front velocity will tend to carry the same speed as the reference velocity until about half way down the forest zone. This representation displays active channeling takes approximately 0.5-1 second to diminish. The surface velocity is subject to bead velocity through the forest. The beads are less dense and have larger diameter, so they bounce off stems and tend to get plugged on trees. Therefore, generally two beads are tracked to represent surface velocity. There is a clear profile of the surface velocity travelling less distance at the same speed as the front velocity.

Time vs. Velocity

On the right side of Figures 5.15 to 5.26, From Section 5.2.2, we recognized the flow of the avalanche is potentially disturbed by the rough and uneven surface. As previewed in Figures 5.16, 5.20, 5.22, and 5.26, the reference front velocity of alumina decelerates as the media flows down-slope. The cause of repetition here is from having one reference slope for the two 50% and two 70% humidity trials. This action is caused by interaction with material settling on the rough surface via friction force bringing the material to a standstill. The trendline slope of the surface velocity validates that material glides on top of the film stuck to the surface at or near terminal velocity. In retrospect, as humidity escalates, the front velocity of the reference trials pertaining to ballotini appears to decrease. This trend is clear if compared between the first and last trials.

The trendlines of the reference experiments are logarithmic in nature to foresee the flowability of the powder if the chute was longer. In general, these trendlines show the material increases speed with distance. In retrospect, the front/surface velocity in forest trials show an opposite slope. One that dips downward in preview of decreasing velocity regarding time. Every so often a bead will get jammed on a tree stump, then bounced back on track showing a further decrease in overall velocity. In nearly all the trials, the relative velocity of the front is greater than surface velocity; however, in alumina trials with 50% forest (Figures 5.22, 5.24, and 5.26) the surface velocity surpassed the front velocity.

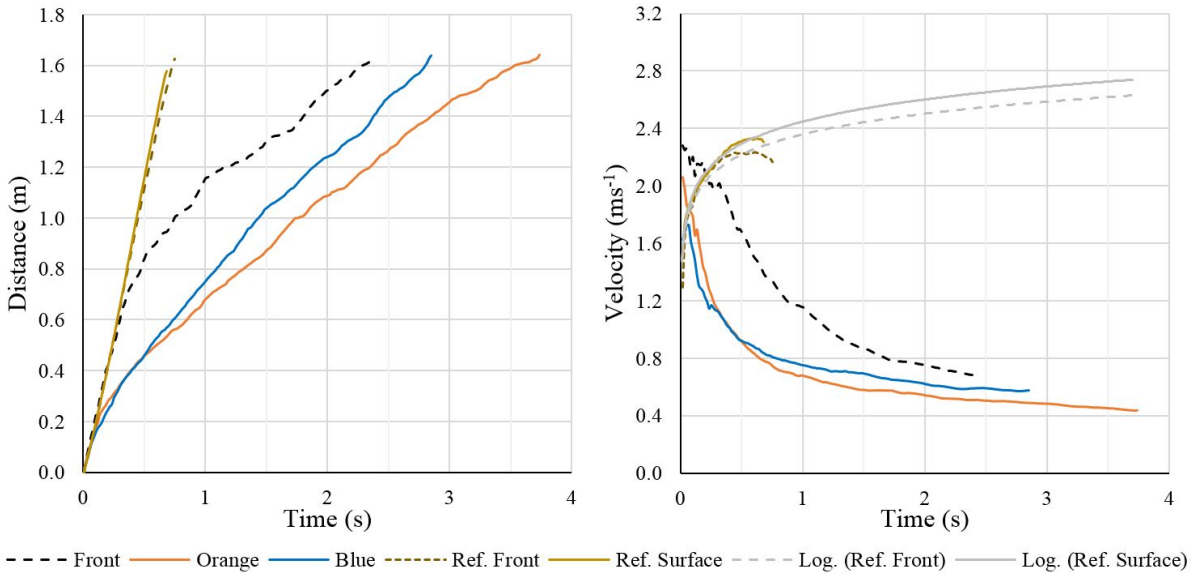

Figure 5.15: Diagram of ballotini flowing through 25% forest at 50% relative humidity showing the change in surface/front velocity between forested and unforested terrain.

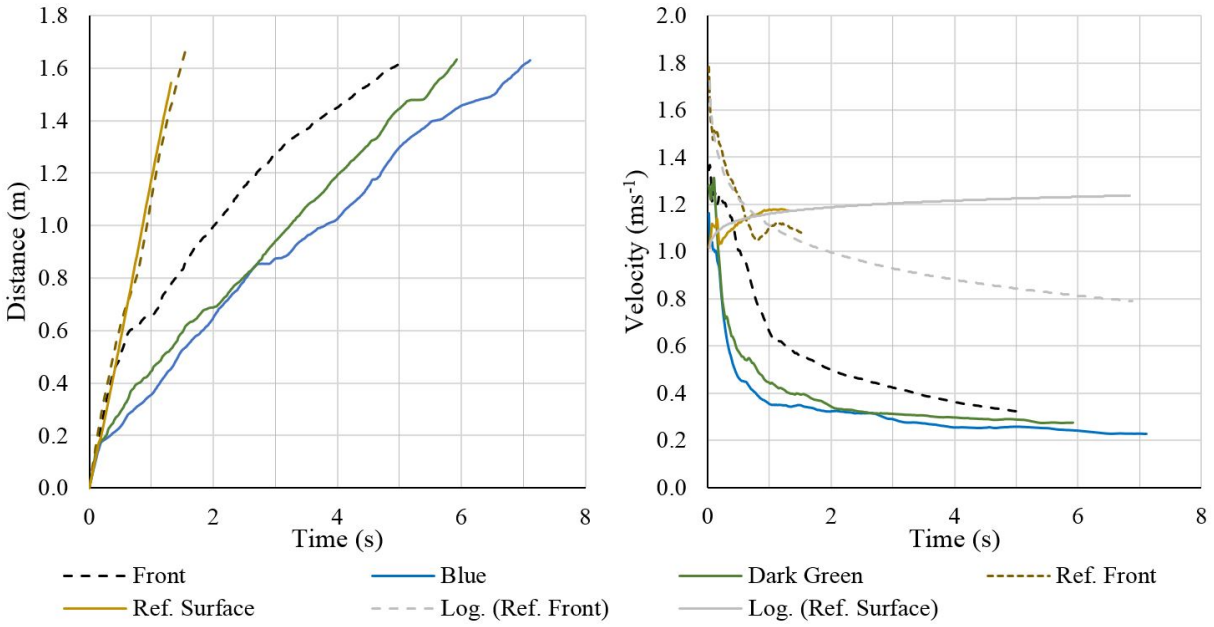

Figure 5.16: Diagram of alumina flowing through 25% forest at 50% relative humidity showing the change in surface/front velocity between forested and unforested terrain.

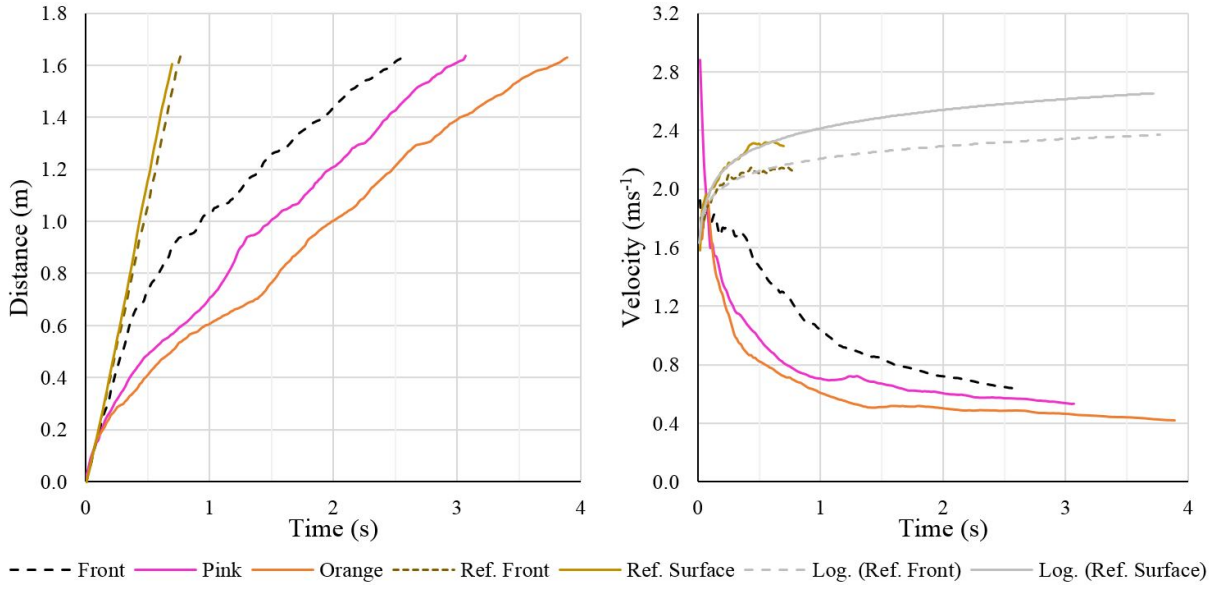

Figure 5.17: Diagram of ballotini flowing through 25% forest at 60% relative humidity showing the change in surface/front velocity between forested and unforested terrain.

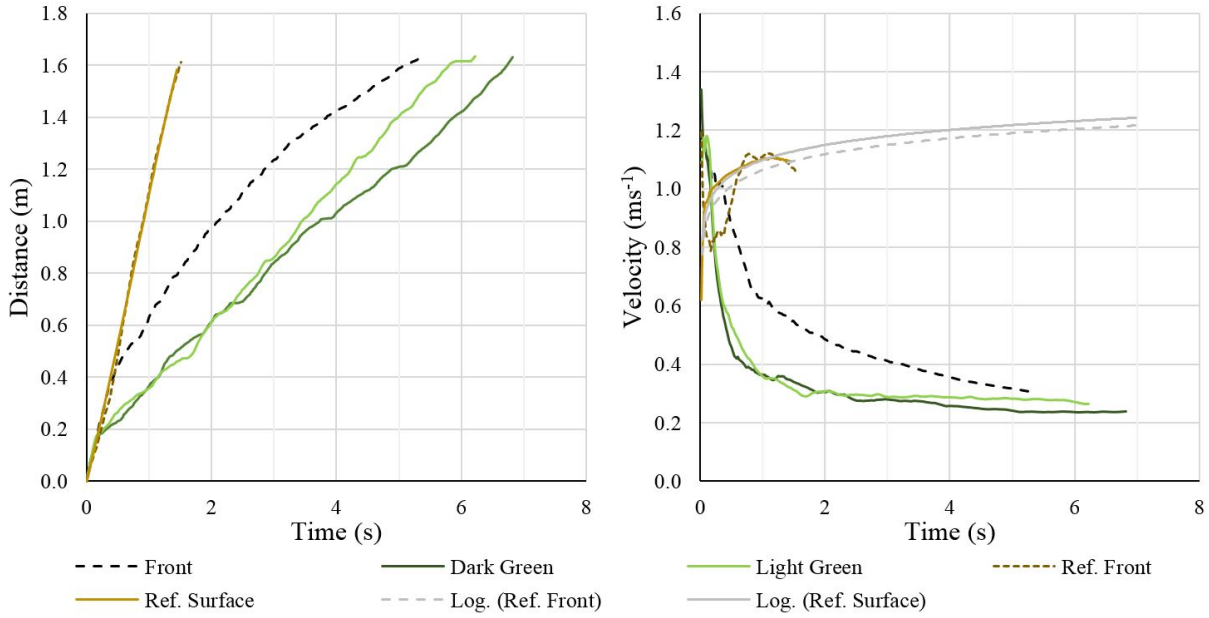

Figure 5.18: Diagram of alumina flowing through 25% forest at 60% relative humidity showing the change in surface/front velocity between forested and unforested terrain.

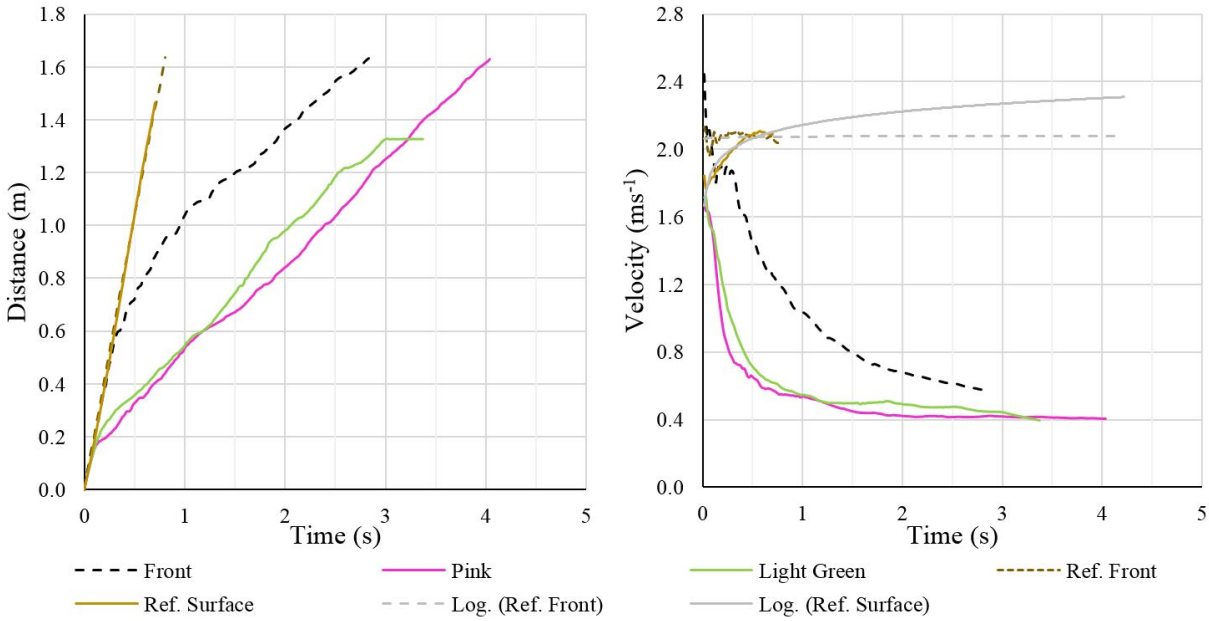

Figure 5.19: Diagram of ballotini flowing through 25% forest at 70% relative humidity showing the change in surface/front velocity between forested and unforested terrain.y

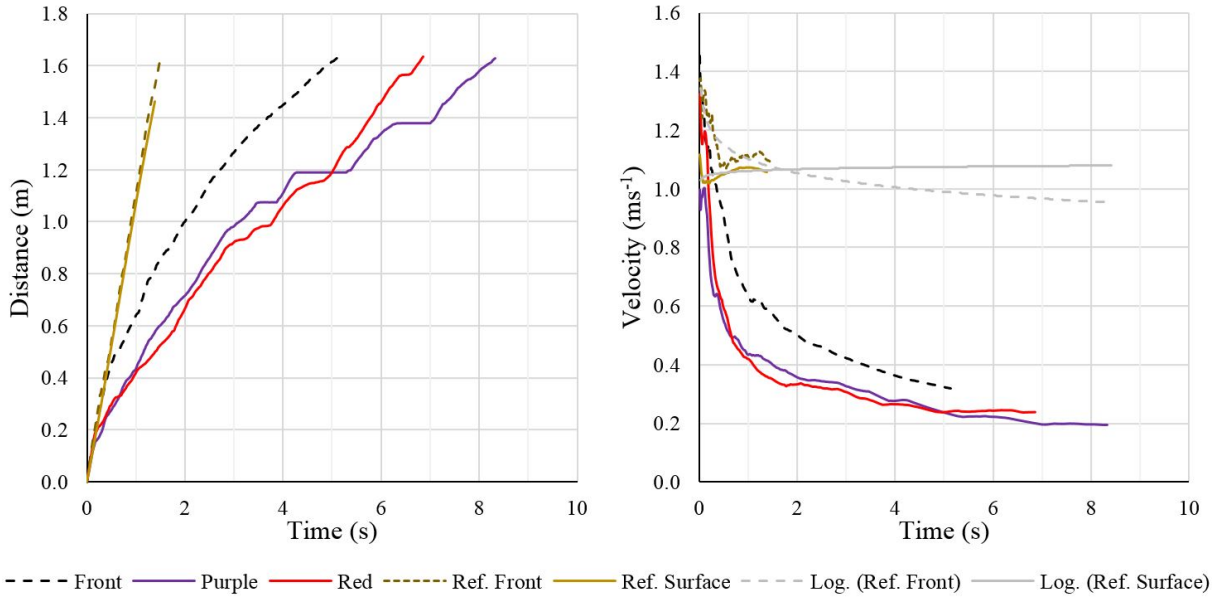

Figure 5.20: Diagram of alumina flowing through 25% forest at 70% relative humidity showing the change in surface/front velocity between forested and unforested terrain.

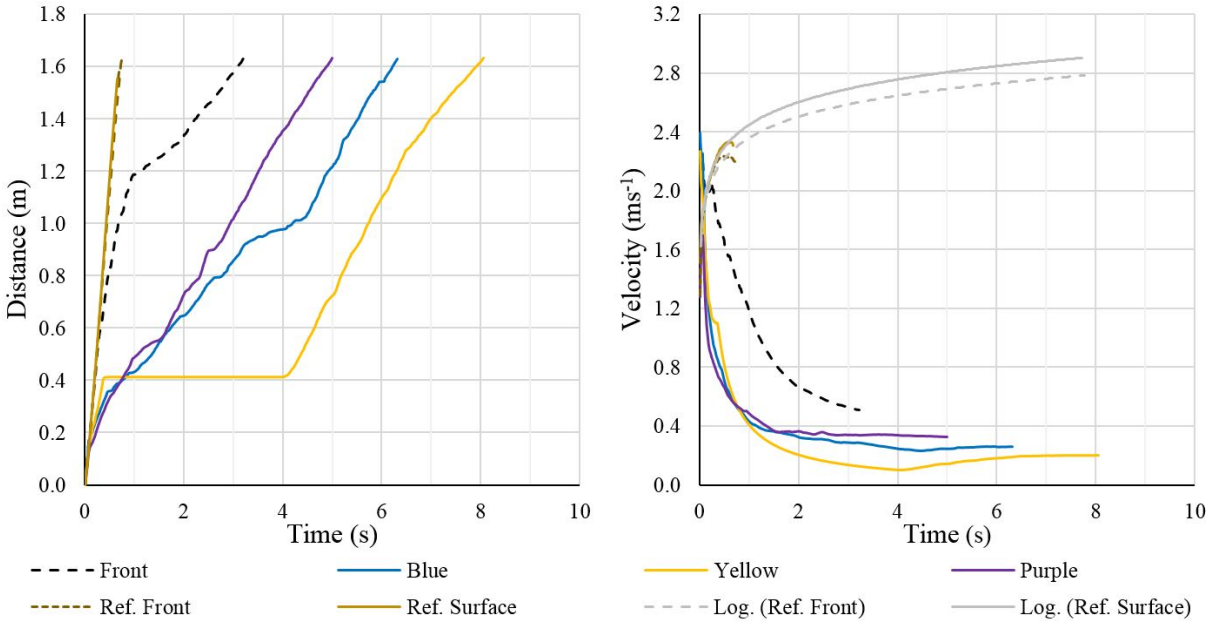

Figure 5.21: Diagram of ballotini flowing through 50% forest at 50% relative humidity showing the change in surface/front velocity between forested and unforested terrain.

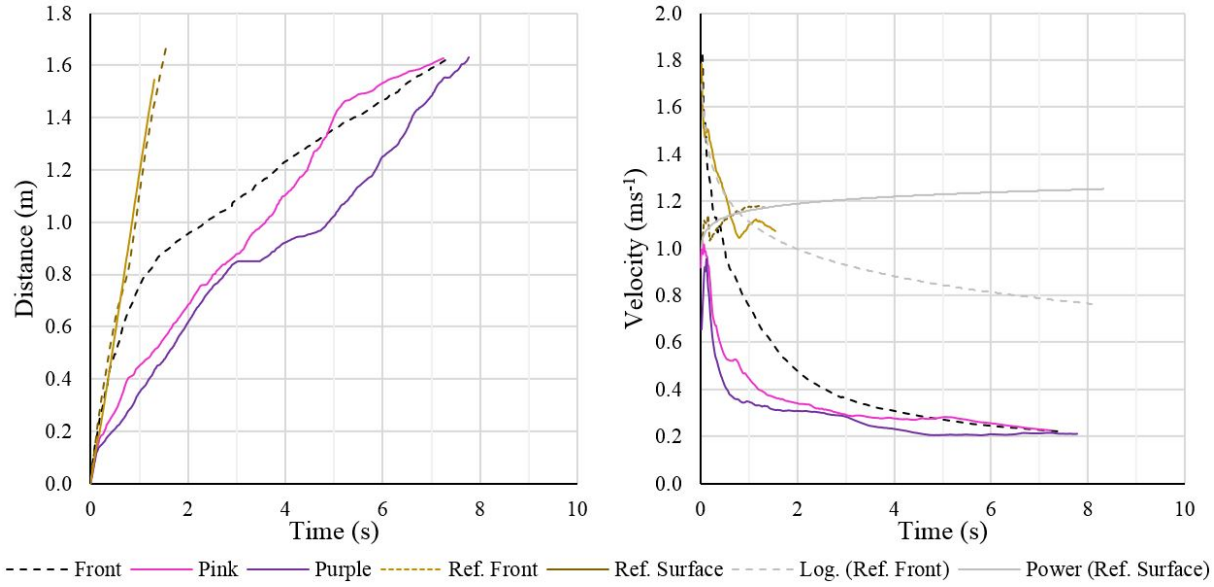

Figure 5.22: Diagram of alumina flowing through 50% forest at 50% relative humidity showing the change in surface/front velocity between forested and unforested terrain.

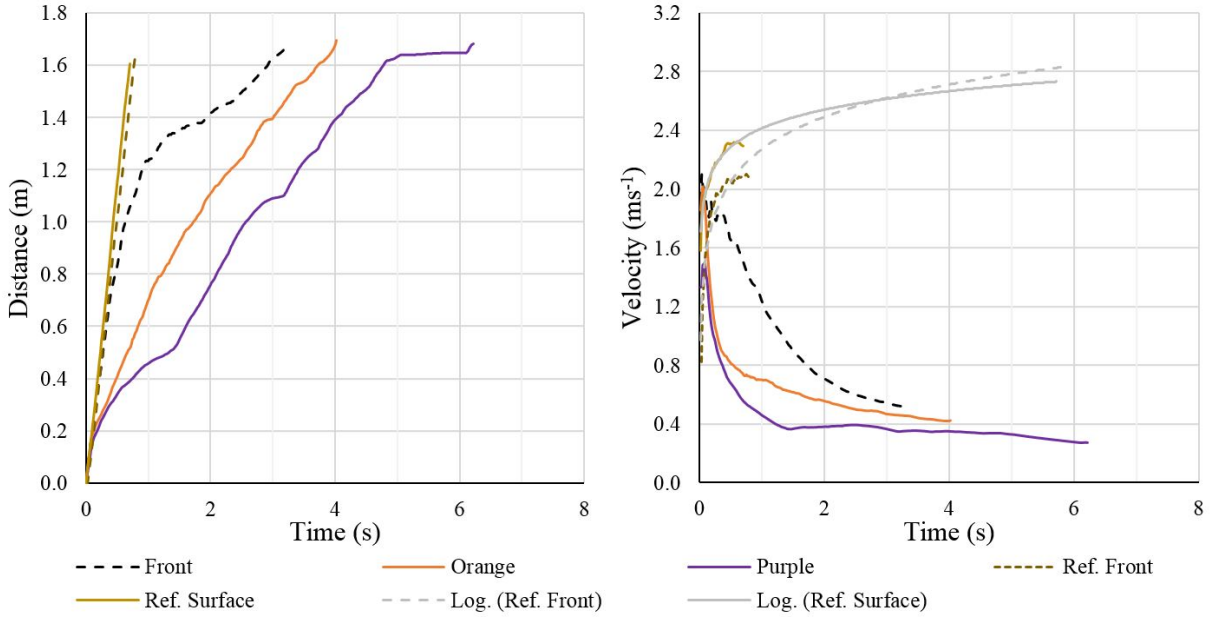

Figure 5.23: Diagram of ballotini flowing through 50% forest at 60% relative humidity showing the change in surface/front velocity between forested and unforested terrain.

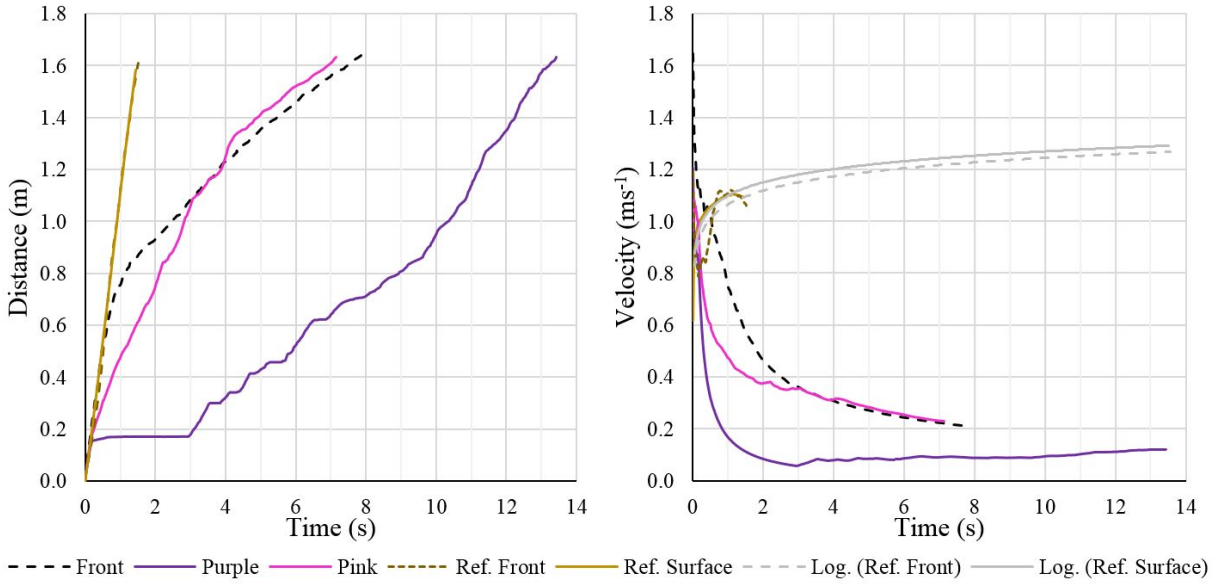

Figure 5.24: Diagram of alumina flowing through 50% forest at 60% relative humidity showing the change in surface/front velocity between forested and unforested terrain.

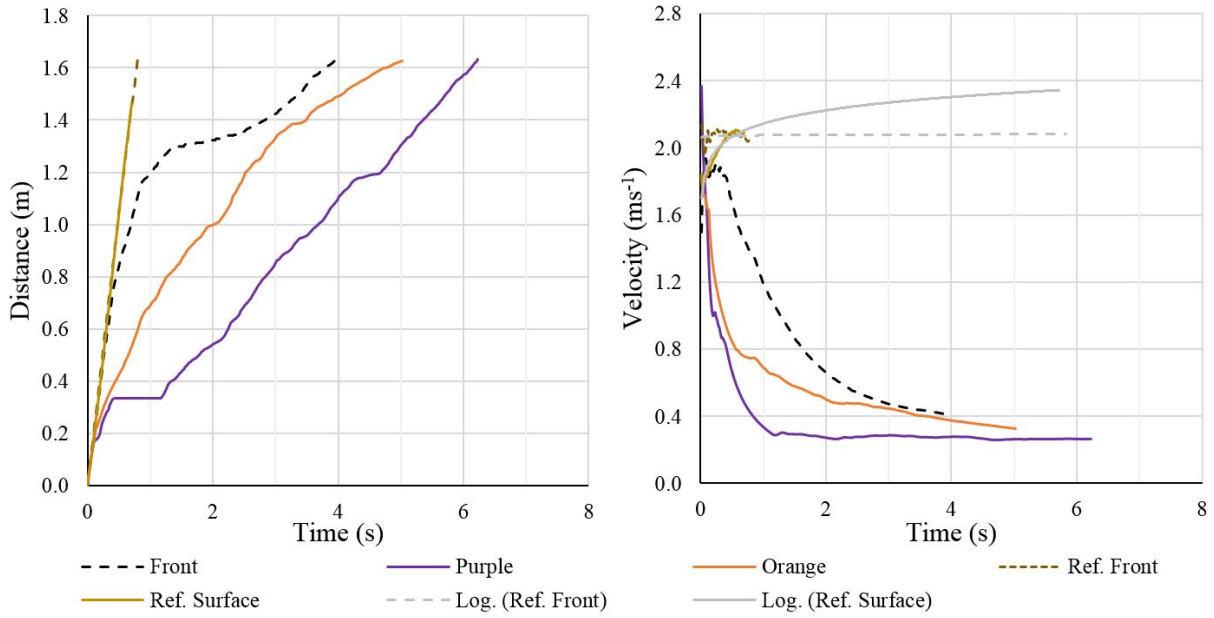

Figure 5.25: Diagram of ballotini flowing through 50% forest at 70% relative humidity showing the change in surface/front velocity between forested and unforested terrain.

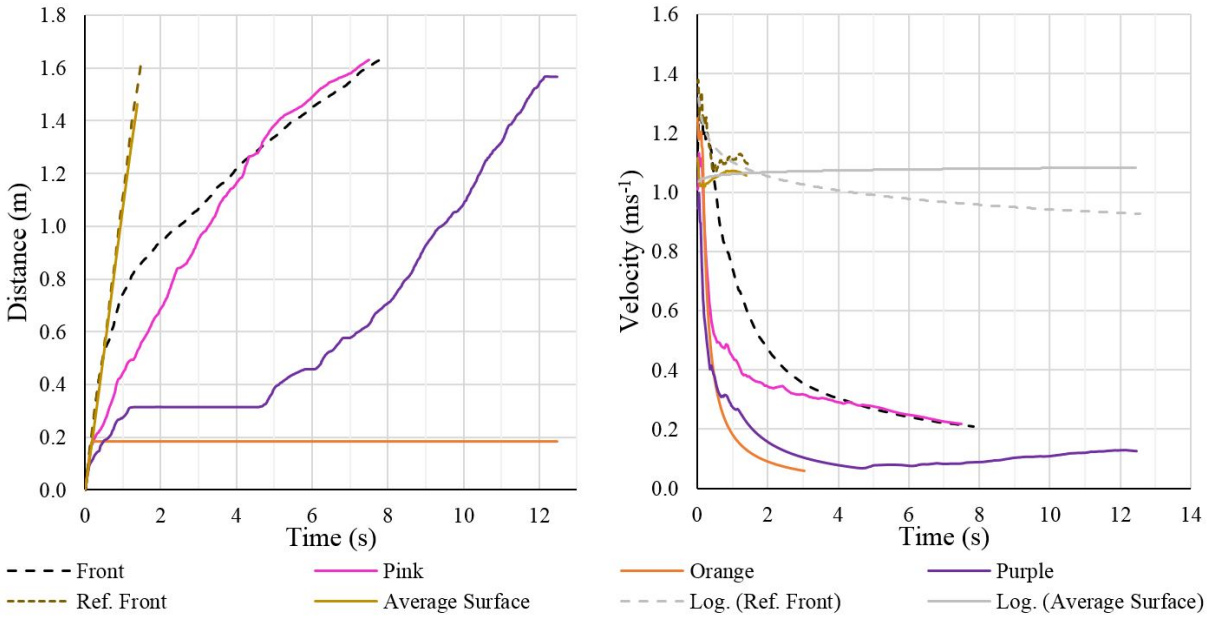

Figure 5.26: Diagram of alumina flowing through 50% forest at 70% relative humidity showing the change in surface/front velocity between forested and unforested terrain.

5.2.3 Runout Distance

The average values for runout distance with increasing relative humidity has been plotted against forest density presented as in Figure 5.27. The following have been observed: (1) For both materials the runout distance decreases exponentially from reference trials to 25% forest trials. The curve then flattens out from 25% forest to 50% forest density. There appears to be a correlation between wide open forest having a larger decrease on runout distance as more trees are added to the pattern. (2) The increase in humidity does not affect the alumina to the same degree as ballotini. It is hardly recognize-able that alumina has a longer runout distance at 50% compared to 70% humidity. (3) Although the material decelerates, after a certain forest density, the channeled material still flows to a similar runout distance.

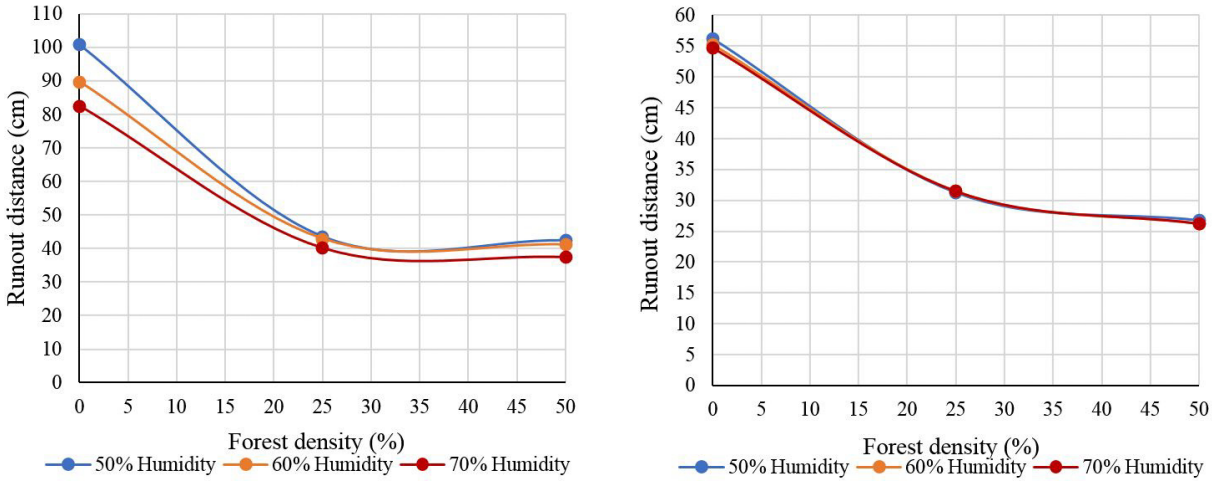

Figure 5.27: Runout distance with alternating forest density and humidity. Ballotini is on the left and alumina on the right

As presented in Section 6.2.2 and described in Section 6.1.4, the driving factors in decelerating an avalanche flow is characterized by the amount of material redirected laterally

by large fans. These fans are located at the tree line of the forest stand for which the initial 10cm generate most of the lateral expansion and therefore the braking effect of trees on avalanches. As the material flows down the forest zone, the fans shrink until the material glides down vertically without opposition. The amount of material decelerated upon entering the forest is therefore larger at 50% than 25% while the degree of lateral expansion is nearly the same.

5.2.4 Characteristics of Detrainment Height, Flow Depth and Lateral Expansion

Deposition Height

The amount of mass wedged on trees is proportional to width and runout distance. As more material is stuck behind trees, the loss of mass and thereby momentum will cause the material to settle and shorten runout distance. As depicted in Figure 5.28, the deposition height vs. relative humidity for increasing forest density is quite dissimilar. Considering ballotini trials: the exponential curve for 50% forest density at 70% humidity proves capillary tension is a driving factor in the rheology of ballotini at altering humidity. As one can discern from the figure, the mean deposition height is nearly the same for 50% humidity. Also, the trend for 0% and 25% forest appears to overlap one another. This variable measures the height of material settled on the surface, not the wedge height of material stuck on tree stems.

The graph on the upper right pertains to alumina, which have quite different properties than ballotini. For one, the humidity within the environment do not appear to influence the deposition height in a predicted manner. 25% forest has the highest deposition followed by 50%. Contrary to the results, material flowing at a higher velocity should carry more material along with the bulk density, however for both forested trials the mean deposition height steadily increases from 60% humidity to 70% even though the additional water (60%-70%) has proved to act as a lubricant for surface interaction during reference trials.

Flow Depth

The method for measuring flow depth forested and unforested terrain is described in Section 5.4.3. Although there a slope showing 0% forest, there is two scales in place to measure the maximum and minimum height deposited on the tree stem where the other forested trials have 10. The flow depth is measured as the observed height of the lowest red marking on tree stems ascribed to scale every 5mm. Although this task is difficult at 50% tree density, this measured height permits the ability to correlate different combinations of parameters qualitatively. For instance, relating the flow height to wedge height on the surface of tree stems. The flow depth has been plotted for altering humidity and forest density in effort to compare the depth with avalanches of greater humidity and forest densities. The trend of such correlations is provided in Figure 5.28. Once again, forested terrain with 25% density are at the top of the charts.

The flow depth and deposition height are proportional to each other in a way that can be interpreted with Figure 5.28. As more material become jammed by the initial 30cm of the forest, the flow height decreases with increasing mass deposition. The figure below depicts the impact of the avalanche flow regime with regards to increasing forest density and humidity. As compaction of the material unfolds, the particles are diverted laterally, spreading out and envelops more surface area at a consequence of losing depth. For ballotini, the reference experiments start at 4.8mm, decreases in flow depth from 50% to 60% humidity and then gradually escalates to 4mm. There is a similar trend for 25% forest, however not as drastic, the trend proves less material was wedged at the forest front, so a larger bulk density flowed down the chute relatively unchallenged. The trend pertaining to alumina shows a

separation of approximately 1mm height difference starting at 50% humidity and converging towards 50% forest and an average 5mm flow height at 70% humidity.

Lateral expansion

Although there is a distinct relationship between width shrinking from ≥ 60% humidity for forested trials, at 50% one can visually discern the width remains unaltered for alumina trials at 25% forest and reference trials. However, at 50% forest density, there is a slight decrease in width at 60% humidity and then slightly increases width towards 70%. Reference trials have a similar shape for ballotini, although the forested trials have a horizontal trend from 50%-60% humidity and then decrease with inflating humidity.

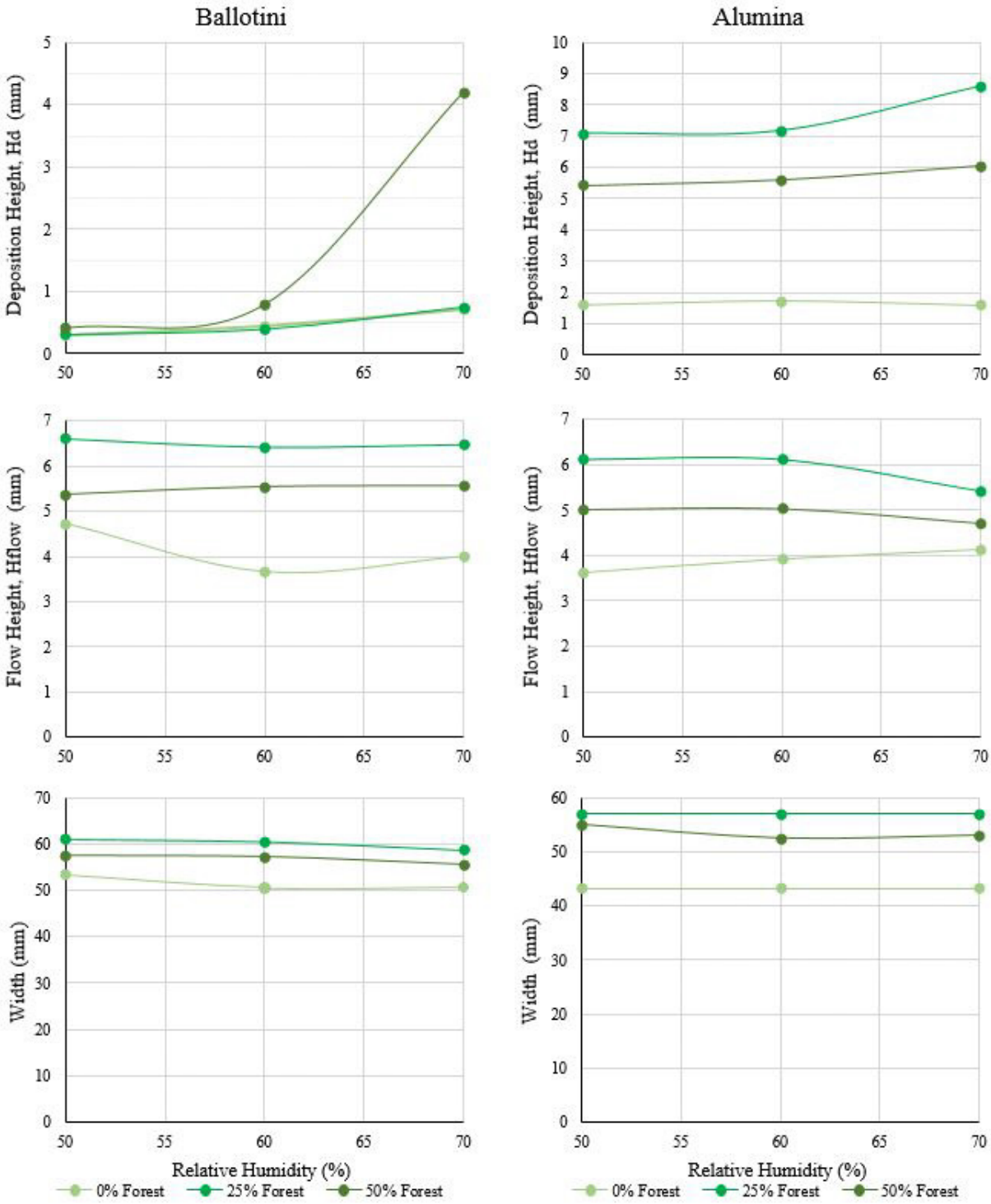

Figure 5.28: Correlation of characteristic phenomena between Ballotini (left) and Alumina (right).

5.2.5 Mass Deposition

Figure 5.29 shows profiles of the average mass deposition left behind as the avalanche flows into the runout zone. The profiles indicate that the amount of deposition is dependent of two phenomenon: First, the amount of forest present and secondly the amount of water content present in the material. Both characteristics have an observable affect on ballotini, left side of Figure 5.29. At 50% humidity, more material accumulates per tree stem for the 25% tree density compared to 50% tree density. This pattern is quickly reversed as the mate-

rial reaches 60% humidity. At this point, one can see an exponential curve increasing in mass deposition with respect to rising humidity. The deposition values for the reference trials of both material remain below the forested trails, thus proving the forest prevents material from flowing into the runout zone. The bottom section of the figure below is the representation of the same values but in a block chart format. By doing this, one can analyze the deposition-humidity-forest density entanglement in a new fashion. Similar to the line chart, the trend throughout the experiments is that 50% forest density accrues the most mass on the surface followed by 25% forest, except for ballotini at 25% forest and 50% humidity.

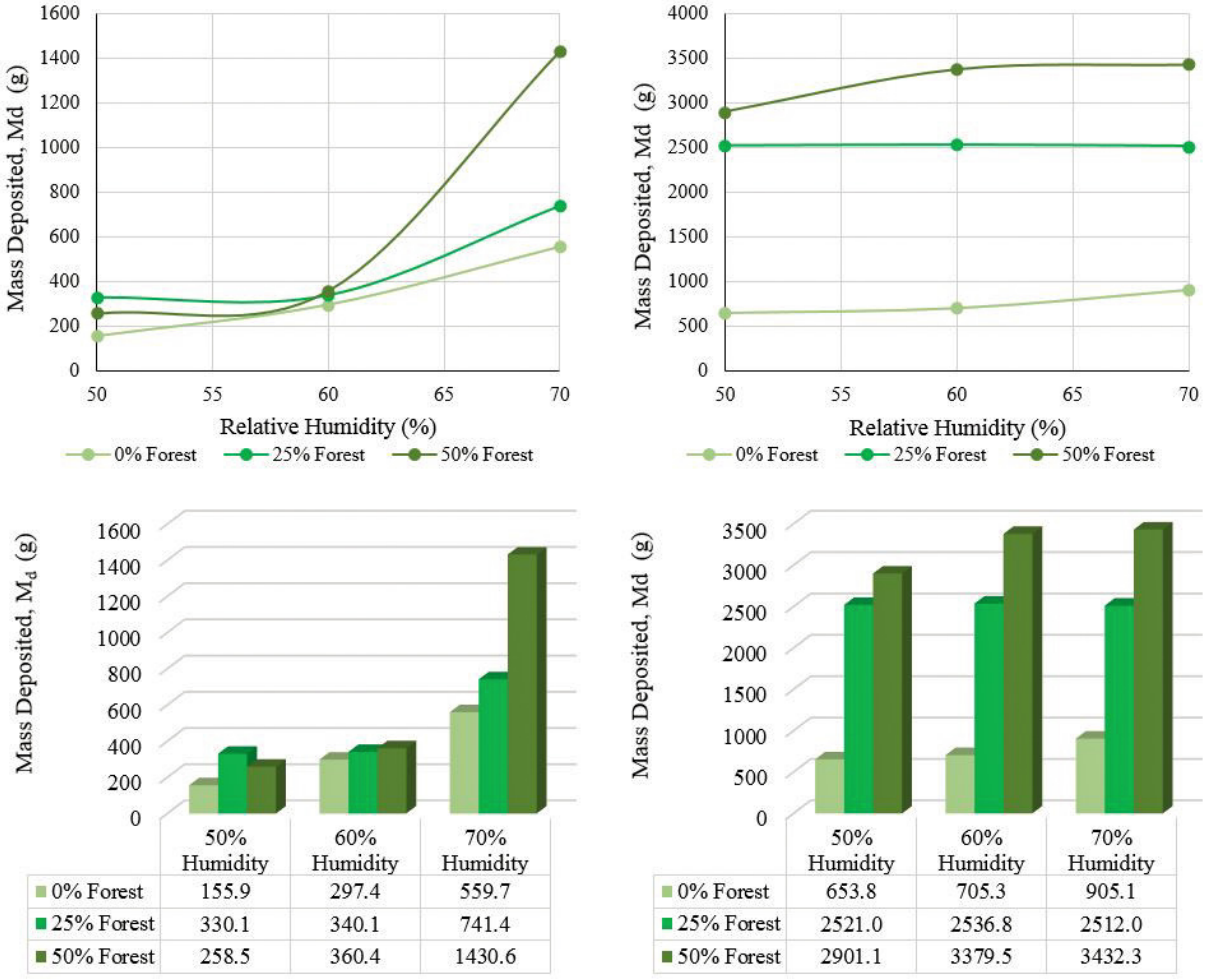

Figure 5.29: Deposition of mass with altering humidity and forest density. Ballotini is located on the left and alumina is on the right.

5.2.6 Mass Extraction Coefficient, K

A major characteristic in determining the actual influence a forest has on the braking effect of trees on avalanches is to measure the force exerted on the tree stems. As shown in Table 5.1, these calculations have been formulated to prove avalanche does not flow through a forest section unhindered. The values provided and Equation 3.1.4 allow one to calculate the mass extraction coefficient, K. The mean deposition height, h_d, is the height of material stuck on the surface of the forest zone along with the average height of wedges, h_w, stuck to tree stems. For bulk and vertical tree grouping, the deposition angle is approximately horizontal so for simplicity 35% angles are used to calculate wedge volume. In general, the larger the mean deposition height the larger the K-value. This extraction coefficient measures the energy loss

from of the flowing mass colliding with individual trees.

				h_d	ρ	‖v‖	K-Value
				m	(kg/m^3)	ms^{-1}	Pa
50% Relative Humidity	25% Forest	Ballotini	Single	0.0003	1583	0.840	0.243
			Vertical	0.0003			0.238
			Bulk	0.0003			0.258
		Alumina	Single	0.0071	955	0.400	0.725
			Vertical	0.0072			0.738
			Bulk	0.0074			0.758
	50% Forest	Ballotini	Single	0.0005	1583	0.540	0.142
			Vertical	0.0004			0.133
			Bulk	0.0005			0.147
		Alumina	Single	0.0054	955	0.351	0.426
			Vertical	0.0056			0.439
			Bulk	0.0059			0.461
60% Relative Humidity	25% Forest	Ballotini	Single	0.0004	1583	0.779	0.276
			Vertical	0.0004			0.284
			Bulk	0.0005			0.311
		Alumina	Single	0.0072	955	0.380	0.664
			Vertical	0.0074			0.680
			Bulk	0.0077			0.705
	50% Forest	Ballotini	Single	0.0009	1583	0.698	0.444
			Vertical	0.0009			0.448
			Bulk	0.0010			0.500
		Alumina	Single	0.0056	955	0.299	0.321
			Vertical	0.0059			0.334
			Bulk	0.0062			0.355
70% Relative Humidity	25% Forest	Ballotini	Single	0.0008	1583	0.676	0.401
			Vertical	0.0009			0.452
			Bulk	0.0011			0.518
		Alumina	Single	0.0086	955	0.379	0.789
			Vertical	0.0088			0.806
			Bulk	0.0091			0.833
	50% Forest	Ballotini	Single	0.0043	1583	0.601	1.628
			Vertical	0.0043			1.657
			Bulk	0.0046			1.736
		Alumina	Single	0.0061	955	0.316	0.391
			Vertical	0.0066			0.421
			Bulk	0.0074			0.468

Table 5.1: Calculation of extraction coefficient, K-Value: h_d is the mean deposition height, ρ is the material density, ||V|| is the average velocity of the dense-flowing core and the length of the forest zone is 1.5m.

The general trend in augmented mass deposition from single tree to vertical grouping to bulk grouping is due to the area affecting flow: for vertical grouping the stem diameter is multiplied by 3 because there are 3 tree stems per vertical group. For bulk grouping, the area affecting flow is much larger, so the tree stem is multiplied by 8 for a grouping of 4 trees. This protocol was developed alongside (Feistl et al., 2014) assumptions in Chapter 3, Equations 3.1, 3.2, and 3.1.4. The main difference between these assumptions is that he assumed a standard deposition height based off observations in the field where this study included the average wedge height, h_w, to the mean deposition height, h_d, observed on the chute. For a clear depiction of this assumption please visit Figure 3.2 located in Chapter 3.2.2.

Ballotini

The general trend of ballotini in Table 5.1 is the increase in force exerted on tree stems with increasing forest density and humidity. However, for 50% density the force per tree drops from 25% to 50% forest density. The even distribution of forces is apparent at this humidity. At 60% humidity the K-value doubles from 25% to 50% forest density and then quadruples at the same step in forest density for 70% humidity.

Alumina

Alumina carries similar phenomena as the ballotini at 50% humidity, where there is a constant decrease in pressure per tree for a greater number of trees present. This pattern persists through each trial and does not seem to be affected by fluctuating water content. From 50% humidity to 70% humidity, there is just a minor increase in pressure per tree at 25% forest. Also, the dip in K-value for 60% could act as a bridge from dry flow to wet flow. The general pattern one can excerpt from this table is the pressure decreases by nearly half from 25% forest to 50% forest density.

5.2.7 Summary of Material Comparison

Based on the data provided throughout the chapter, increased tree stem quantity has proven to impact the momentum of the flowing avalanche. The increase in forest density appears to have a maximum braking effect at 50% since deposition occurred at a larger magnitude and that fans behind neighboring trees interact at a larger scale with respect to dense forests. At 50% forest density, the rigid trees slow down the bulk of the dense-flow immediately upon entering the forest where 25% allows for more material to flow past the initial tree line unhindered. Further down the path the dense flow is broken up by smaller fans that cause the material to spread sideways. It becomes apparent that the larger the avalanche volume, the greater the braking affect becomes for a given forest size. Aside from the material property difference, alumina starts with more mass and leaves more mass behind throughout the forest. Characteristic phenomena are provided in Table 5.2 to help relate these quantities in a qualitative manner. This table shows the relationship between the increase in humidity, forest density, and the effect those characteristics have on the wedge height of single trees vs. grouping and overall mass deposition. Furthermore, in this study it is not feasible to calculate each wedge-shaped deposition pattern behind individual trees or tree groups, as we assume average forest values for each computational element such as forest density.

Average Values

0% Forest

Material	Width (cm)			Runout (cm)			h_d (mm)			Single tree, h_w (mm)			Tree group, h_w (mm)			H_{flow} (mm)			M_d (g)		
	50	60	70	50	60	70	50	60	70	50	60	70	50	60	70	50	60	70	50	60	70
Ballotini	53.5	50.5	50.8	100.8	89.8	82.5	0.3	0.5	0.7	0.3	0.5	0.7	1.3	1.3	3.0	4.7	3.7	4.0	155.9	297.4	559.7
Alumina	43.3	43.3	43.3	56.3	55.3	54.8	1.6	1.7	1.6	0.9	1.0	1.0	2.3	2.6	2.7	3.6	3.9	4.1	653.8	705.3	905.1

25% Forest

Material	Width (cm)			Runout (cm)			h_d (mm)			Single tree, h_w (mm)			Tree group, h_w (mm)			H_{flow} (mm)			M_d (g)		
	50	60	70	50	60	70	50	60	70	50	60	70	50	60	70	50	60	70	50	60	70
Ballotini	61.0	60.3	58.8	43.7	42.3	39.8	0.3	0.4	1.6	1.7	2.0	2.5	2.2	3.3	5.9	6.6	6.4	6.5	330.1	340.1	741.4
Alumina	57	57	57	31.3	31.5	31.5	7.1	7.2	8.6	3.1	3.1	3.5	6.0	7.0	7.3	6.1	6.1	5.4	2521.0	2536.8	2512.0

50% Forest

Material	Width (cm)			Runout (cm)			h_d (mm)			Single tree, h_w (mm)			Tree group, h_w (mm)			H_{flow} (mm)			M_d (g)		
	50	60	70	50	60	70	50	60	70	50	60	70	50	60	70	50	60	70	50	60	70
Ballotini	57.5	57.3	55.5	42.5	41.3	37.5	0.4	0.8	4.2	1.4	1.9	2.2	2.0	3.0	4.3	5.4	5.5	5.6	258.5	360.4	1430.6
Alumina	55.0	52.5	53.0	26.8	26.3	26.3	5.4	5.6	6.1	3.0	4.2	4.4	5.0	5.8	8.1	5.0	5.0	4.7	2901.1	3379.5	3432.3

Table 5.2: Characteristic phenomena at 50%, 60%, and 70% relative humidity.

				Ratio Observed	M_{wedge}	M_d Corrected	$M_{d\_average}$ Corrected	M_d Observed	Error
				(%)	(g)	(g)	(g)	(g)	(%)
50% Relative Humidity	25% Forest	Ballotini	Single	0.33	62.18	147.22	149.19	330.11	54.80
			Vertical	0.33	45.39	144.03			
			Bulk	0.33	110.09	156.33			
		Alumina	Single	0.25	22.21	2432.99	2484.97	2521.00	1.43
			Vertical	0.25	203.67	2476.30			
			Bulk	0.25	494.01	2545.61			
	50% Forest	Ballotini	Single	0.40	143.25	251.84	249.57	258.50	3.45
			Vertical	0.40	75.02	236.12			
			Bulk	0.40	181.97	260.76			
		Alumina	Single	0.35	45.79	2600.28	2698.01	2901.13	7.00
			Vertical	0.35	282.87	2679.50			
			Bulk	0.35	686.12	2814.26			
60% Relative Humidity	25% Forest	Ballotini	Single	0.43	73.94	250.61	263.54	340.10	22.51
			Vertical	0.43	102.12	257.51			
			Bulk	0.43	204.18	282.49			
		Alumina	Single	0.25	32.21	2469.57	2540.00	2536.78	0.13
			Vertical	0.25	277.21	2528.05			
			Bulk	0.25	672.40	2622.38			
	50% Forest	Ballotini	Single	0.30	152.70	354.64	370.35	360.38	2.77
			Vertical	0.30	168.80	357.42			
			Bulk	0.30	409.43	399.00			
		Alumina	Single	0.38	49.07	2889.77	3033.67	3379.45	10.23
			Vertical	0.38	380.63	3008.48			
			Bulk	0.38	923.25	3202.75			
70% Relative Humidity	25% Forest	Ballotini	Single	0.50	77.06	569.28	648.50	741.35	12.53
			Vertical	0.50	326.43	641.10			
			Bulk	0.50	652.87	735.11			
		Alumina	Single	0.30	36.87	3539.26	3630.82	2512.03	44.54
			Vertical	0.30	301.48	3615.05			
			Bulk	0.30	731.27	3738.16			
	50% Forest	Ballotini	Single	0.40	166.11	2336.03	2401.74	1430.55	67.89
			Vertical	0.40	346.78	2377.66			
			Bulk	0.40	841.10	2491.55			
		Alumina	Single	0.40	60.81	3360.44	3668.69	3432.28	6.89
			Vertical	0.40	742.36	3620.73			
			Bulk	0.40	1800.66	4024.91			

Table 5.3: Correlation between the Mass Detrainment Model and measured values from the experimental study.

Since deposition height of the material wedged on the tree stems is not equally distributed over the total area, a correction is considered. This correction utilizes a ratio of the area which most of the flow passed through and undoubtedly settles. For calculation purposes, the reference area is $8460 cm^2$ of which underlies the location of the affected tree stems. This correction is presented in Table 5.3, where measured mass (M_d Observed) in the experimental study is presented alongside calculated values based on the theoretical model (M_d Corrected). The correlation focuses primarily on assessing the observed values in the lab vs. the calculated theoretical values via percent error located on the far-right side of the table. It becomes clear which trials were more successful and have potential to replicate to a large-scale model.

Chapter 6

Summary and Conclusion

In this thesis, the focus of the experimental study was to observe the characteristics of the braking effect of a given forest density after triggering avalanches and monitoring such phenomena as the material flows down the small-scale chute. The assumptions that set boundaries to the model include an avalanche being released above the perfectly rigid forest stand for which no external factors are entrained in the flow.

In Chapter 2, a brief introduction is provided regarding snow avalanche categories, formation, avalanche susceptibility and forest coverage as active avalanche mitigation. Chapter 3 and 4 entail a descriptive analysis of prevailing theory to back-up the experimental study. The theory provided in previously enables one to highlight the variances and similarities of modeling avalanches in timberland via correlations of $\alpha = 0$ and $\alpha \neq 0$ for the detrainment approach where α is an extraneous factor that determines the behavior of random fluctuation energy. When $\alpha = 0$ for the detrainment approach, snow is deposited on the steep slope and eventually extracts enough momentum to halt the avalanche before reaching the road. For the $\alpha \neq 0$ case, the avalanche overflows the road as observed in the field and is therefore accepted as an accurate simulation. "These significant differences can be illustrated using the calculated velocity profiles where the fluctuation energy for dry snow (characterized by $\beta = 0.7$) causes higher velocities for $\alpha \neq 0$, and therefore less snow is deposited, leading to a longer run-out" (Feistl et al., 2014).

The addition of the detrainment approach regarding forest effects on avalanche dynamics is a significant addition to current avalanche hazard analysis, especially for particularly recurrent, small-to-medium avalanches. Protection forests have proven to shorten the run-out distance of such avalanches and are therefore an attractive asset to alpine communities. By digging deeper into quantifying this role, Feistl and his team have been able to compare the two different approaches in determining the braking effect of trees on avalanches: first, is to increase friction parameters (Gruber and Bartelt, 2007).). The second, which is carried out in this experimental study, is to measure the mass extraction rate which is entirely dependent on the forest structure and snow conditions and then parametrized by a single coefficient K. "The extraction is the result of higher friction, so the methods are equivalent, but they lead to different parametrization of the braking process. However, the detrainment approach is more direct and appears to account for physical processes, such as snow jamming between trees, that are not embodied in the Voellmy friction model" (Feistl et al., 2014). As observed in Chapter 6, the friction method is preferred since large wedge formation is minimal for ballotini at a humidity of 50%. Also, the volume of wedge deposition decreases from single trees to vertical grouping which proves there is no jamming between the tree stems.

Feistl and his team systematically tested the friction and detrainment methods on an ideal, parabola-shaped slope to accurately measure the performance of their new model. It's accepted that run-out shortening caused by detrainment is subject to release volume, pro-

vided the smaller the release volume, the greater the reduction in run-out length. "This result implies that the stopping of equal mass will have a greater effect on smaller avalanches, which qualitatively agrees with observations. There is almost no effect of detrainment on larger avalanches, which also agrees with observations" (Feistl et al., 2014). Moreover, the deposition patterns athwart the avalanche track were heavily investigated and concluded that forest effects on small-to-medium sized avalanches are indeed dependent on velocity. Another significant observation was that generally more snow is deposited in steep terrain when applying the detrainment approach compared to the friction approach. "This result also corresponds to the field observations: avalanches did not reach the valley floor because of snow being continuously detrained in the forest, even on steep slopes. Interestingly, our analysis of the development of the total momentum of the avalanche revealed that the deceleration and stopping of the flow are triggered later but more efficiently" (Feistl et al., 2014). The velocity profiles provided in Chapter 6.2.2 provide an in-depth analysis of the powder being continuously detrained in the forest relative to the reference trials. A detailed theoretical background is provided and therefore meeting objective one. A detailed review of snow avalanche dynamics and correlation between avalanche types, numerical models, and small-scale chute experiments has been included, thus meeting Objective one.

In Chapter 5, a thorough description of the model is provided as follows: chute set up, materials utilized and their character properties, alterations to the clean room, filming equipment used, methods to control humidity and steps taken to reduce electrostatic generation. Objective two is satisfied by including a brief overview of small-scale model design in effort to replicate avalanche deposition and overall braking effect of trees on avalanches. Objective three has been met with a total of 62 small-scale experiments, for which every trial was subject to varied forest density, relative humidity, and material types.

Chapter 6 provides the key phenomenological characteristics of the avalanche flow through the forest, meeting Objective four. As the experiment continued, three main phenomena have a role in the braking effect on the avalanche:

Firstly, since material subject to higher humidity were forced into wedges at the forest stand, with an enlarging flow density, the ballotini approaches its densest state which limits further compression. When colliding with a tree, the ballotini is forced to climb up the tree before the particles can be redirected outwards, thus creating a fan. The placement of tree stems within this random grid along the chute and relative to other trees is an elemental constituent to the braking effect of trees on avalanches. This property impacts the change in mass of the flowing avalanche since the fans behind neighboring trees interact at a larger scale with respect to dense forests. For this reason, tree groups appear to grab chunks out of the flowing mass and settle the material in place.

Secondly, the larger forest density caused the material to be tossed into suspension meaning the flow density decreased with expanding forest density since more material is moving in saltation. The first 30cm of forest plug material at a much higher rate than everywhere else. For this reason, the uppermost areas in the forest stand take on a fundamental role regarding the stability of the entire forest below. As the amount of tree stems increases to 50% density, the amount of material slowed down and plugged upon entering the forest increases while the degree of lateral expansion decreases proportionally. Also, the suspension layer persists for a longer duration at higher humidity, especially 70%. This could be due to the acceleration of material jamming at the forest front, consequently, the wedge acts as a ramp sending more material air-born.

Thirdly, as stated by Bernoulli's principle, a decrease in the speed of a fluid occurs simultaneously with an increase in the fluid's potential energy. As the increasing forest density restricts saltation of the particles in motion, along with bending tree stems to vertical, they begin to decrease velocity and undertake a gliding motion instead. At this instance, the crit-

ical angle of inclination where the dispersive pressure becomes greater than the overburden pressure is nonexistent. There is a reversal in forces and the dispersive pressure becomes smaller than the overburden pressure, as a result, the buildup of media in the runout zone smoothens out reducing.

To finish, after these observations, it became apparent that a compaction ratio was essential to compute the mean deposition throughout the forest. The distinguishing feature in this experimental study is the tree stems are perfectly rigid and will therefore not become entrained and part of the flowing debris.

Furthermore, front/surface velocity, runout distance, flow height, stem wedge height, mean deposition height/mass, width and the mass extraction coefficient have been quantified; thus, satisfying Objective five. The methods for controlling humidity and thereby flowability of the material in a targeted demeanor is explained in Chapter 6 along with each parameter explained above. Profiles have been plotted of the front/surface velocity vs. reference trials. In nearly all the trials, the relative velocity of the front is greater than surface velocity; however, in alumina trials with 50% forest, the surface velocity surpassed the front velocity. This hydrodynamic effect was solely observed in alumina trials. The reason for this phenomenon is due characteristics indicated in Table 10 which verify alumina is moderately cohesive. Because the determined 'Hausner Ratio' value of 1.38 is at the boundary between cohesive and medium flow behavior, one can expect this material to possess free flow characteristics along with an aptitude for cohesiveness. Based on data provided in Chapter 6, it is safe to assume ballotini represents a dry-cohesionless flow where alumina can be considered a fitting representation of a wet-slab avalanche due to its inherent cohesive properties. A determined hydrodynamic effect of ballotini and alumina is when their particles counteract, they are exposed to capillary, electrostatic, and van der Waals forces. The angle of wall friction represents the adhesive strength of the powder and the wall composition. The larger the value of the $\varphi^{\circ}_{bed,stat}$ is, the more difficult is to move the powder along the wall's surface which is significant for the front velocity of alumina slowing down.

Certain material characteristics such as particle size distribution, morphology, surface area, absolute and density influence avalanche rheology. The most influential parameter was moisture content. This characteristic phenomenon proved to have a significant impact on the study, as the liquid bridges and capillary forces acting between ballotini particles lead to reduced flowability and increasing volume release. This interesting feature was of special interest concerning ballotini since the material properties are rounded-well sorted. The liquid bridge has much more impact on ballotini for this reason, where alumina did not seem to be influenced as much since the material properties were rounded poorly sorted.

Based on values attained in Chapter 6.2.7. and after correlating the accuracy of the Detrainment Approach vs. observed values obtained in the lab, it is safe to assume ≈65% relative humidity is the optimal level to test ballotini. Since alumina did not have the same alterations to fluctuating relative humidity, and humidity is satisfactory. In comparison with the reference trials, the maximum forest density (50%) has the largest impact on avalanche rheology. Reasons being, the generalized force exerted on each tree stem has more influence on volume release for a densely packed forest than one with minimal tree stems. Although the individual trees might take more force per tree, the number of trees limits the overall deceleration of a densely flowing mass.

The amount of force exerted per tree stem for ballotini experiments generally intensifies with increasing forest density and humidity. However, for 50% density, the force per tree drops from 25% to 50% forest density parallel to decreasing observed volume release. This result proved that more tree stems spreads out the material to a higher degree thus evenly distributing the load exerted by the dense-flowing core and preventing active wedging to occur. For 50% humidity, the friction method is preferred since the wedge volume is lower for

vertical grouping compared to single tree stems. Comparable phenomena occur to alumina as the ballotini at 50% humidity. Where there is a constant decrease in pressure per tree for a greater number of trees present. This pattern persists through each trial and does not seem to be predisposed by altering water content. The Detrainment Approach is effective for trials performed ≥60 relative humidity.

6.1 Discussion

6.1.1 Experiment Repeatability

A total of 20 reference experiments were conducted to limit error and enhance repeatability of the study to an average of ≤0.2% error regarding mass loss. To ensure qualitative results, a clean room was build around the chute which limited environmental influence and gave the possibility to control the humidity within the lab. Relative humidity became a critical parameter and undoubtedly developed into a driving factor in analyzing the validity of this experimental study. Initially the humidity was regulated to hinder static electricity generation until the influence of capillary bridges became evident. This manifest phenomenon altered material characteristics with additional surface tension and provided the opportunity to adjust flow regime in a targeted demeanor.

6.1.2 Human Error

A large portion of material was wedged in the corners of the start zone and was not accounted for in the calculations. The mass should have been weighed and subtracted from the original since the focus was to measure the mass deposited through the forest, this unknown volume procures skewed results since the forest did not actually stop the mass; for the higher the humidity, the larger the wedged mass. There is a portion of the surface where forested area is not located on the flow path. The area in that section is nearly proportional to the surface area of the acceleration zone, so material stuck to the surface is nearly proportional but still not exact enough to have a fool proof model. Additionally, maintaining a constant relative humidity proved difficult since the reliability of the humidifier proved to be too weak for the size of the room. Another human error is caused by manually measuring the dimensions of each deposit to the nearest 0.5 mm. Some tree groups would have a deposition height much higher than others just a few centimeters apart so much of the determination of relative height was determined empirically. To simplify this issue, I took height measurements every 50cm over the forest zone.

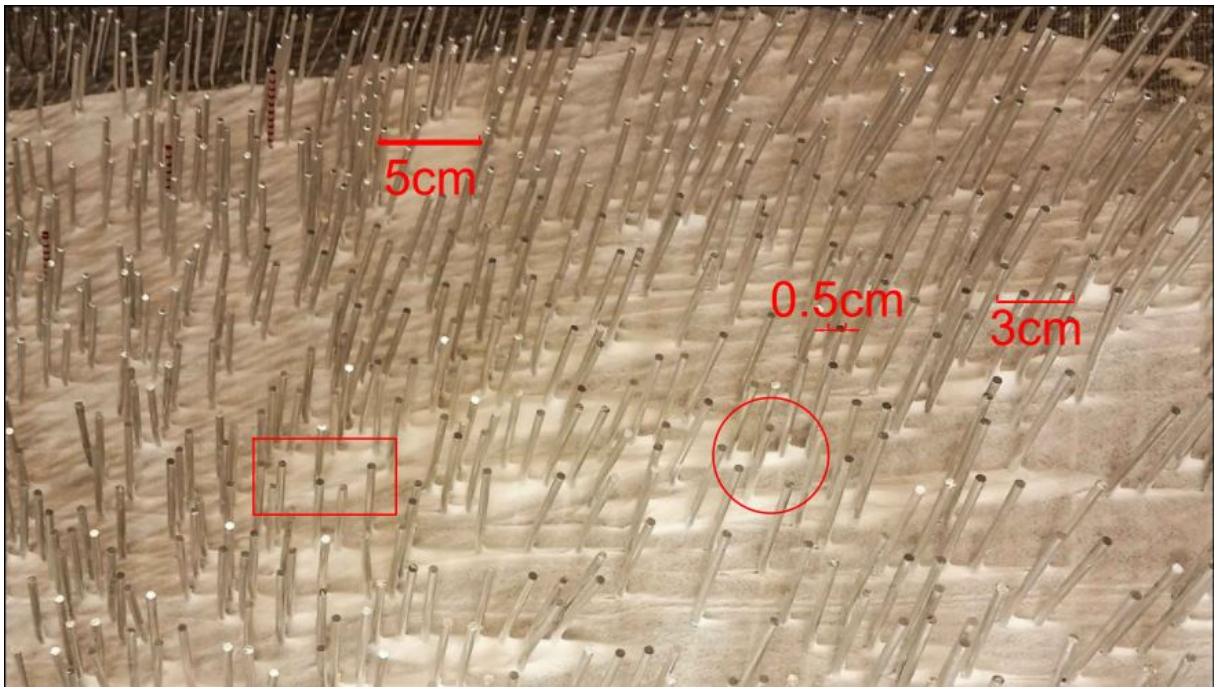

Figure 6.1: Uncertainties in measuring deposition shapes.

As depicted in the Figure 6.1 above, one tree group has a mass deposition length of 5cm where another one of nearly the same dimensions has a value of 0.5cm. On the right side of the figure lies a deposition length of 3cm from a vertical group. In opposition a vertical group with equal number of trees in the circle and has a deposition length of 1cm. At a closer look, the height between each stem on the vertical group in the circle is quite variable. The square is not considered a tree group; however, this region causes a large volume release. The image above proves how difficult it is to accurately measure deposition values. Another error is pertaining to the flow height through the forest. Although the video was recorded in 4K, it was difficult to find the reference points/scales when the forest density was at 50%.

6.1.3 Model Error

At first glance one could assume the stump hole voids beneath the tape disturb the flow regime by propagating separation of particles into sub-parallel trenches. This apparent trampoline effect could be relevant since the formation of these trenches appears to be over this area and not over the incompressible aluminum. However, this action is most likely due to the slope and surface roughness of the material which causes saltation flow instead of gliding. At times the beads flew past the front, so they instantly became void. The trials where the surface velocity was of higher magnitude than the front refers to beads catching the front but not surpassing it.

While investigating what occurs when the surface is previously coated in media, i.e. whether more material entrained or detrained, I was not able to attain valid results so those results of which are void. Although mass balance values for ballotini did not stay far from the reference trials, alumina values were too far over the standard for reliability. As trials unfold, large mass would detrain to the model (570g), then after 5 trials the avalanche entrained about 20g and then detrained 300g after 2 more trials.

6.1.4 Nature vs. Experimental Study

The study by Feistl and team observed natural characteristics after triggering seven avalanches and simulated each into a case study to demonstrate the applicability of the detrainment approach on small-to-medium sized avalanches. The methods were centered around finding a relationship of the mean deposition heights and their correlation to observed wedge heights of snow pinned to trees.

To properly calculate mass extraction rates will require in depth knowledge of the forest structure, as it encompasses averaging spatially inhomogeneous deposition patterns behind trees. "This, coupled with a comparison of the observed run-outs and lateral extension of the avalanches, is presently the only method we can apply to ascertain model performance. However, it also indicates that the parameter, K, can be calibrated by performing more mass-balance studies in forests" (Feistl et al., 2014). To increase reliability, such studies need documentation of the overall mass balance for each case study and relating these data sets to the observed forest structure and deposition patterns within them.

This is where the experimental study comes into play; however, in this experiment the distance between trees is uniform so wedging with this alignment is not as effective as compared to the horizontal grouping provided by Feistl and team. Reasons for this could be due to the inherent compressibility properties of snow. To replicate similar effect, this study incorporated bulk grouping (2x2 row) and vertical grouping with a minimum of 3 trees per group.

Only when such methods are completely accountable, the values of K can therefore be improved with in depth fieldwork. To ascertain reliable K values, on must parametrize forest type, stem density, surface roughness and vertical structure of the forest seem to be the decisive constraints to be considered (Teich et al., 2012). The third avalanche that could not be simulated adequately (ID-VI) could, however, be reproduced using the Voellmy extension ($\alpha > 0$). This suggests that the fluidization of the avalanche in dry/cold conditions is important, stressing the idea that jamming effects cannot develop easily in low density flows with large granular fluctuations (Feistl et al., 2014). The ballotini at 50% humidity is a good representation of the Voellmy extension ($\alpha > 0$) where fluidization of the avalanche occurs.

In personal correspondence with Dieter Issler from NGI, he described a snow avalanche with similar features, which he observed in the winter of 2006 in Davos, Switzerland. The trenches and ridges which characterized this specific avalanche had – surprisingly - developed in a concavely curved area of the slope, where a compressive stress environment was to be expected. As Dieter Issler explained further, he had not found any mentioning of similar deposits in literature, but made an observation in 2005, which might, in relation to the observations mentioned above, indicate shear-rate dependency. This hypothesis is based on the observations in 2005, where the deposit of an avalanche flowing through a narrow gully showed an approximately ellipsoidal cross-section. Other than what Dieter Issler observed in 2006, there was only little curvature in flow direction this time, but a significant influence of the banks on both sides. In correspondence with one of his colleagues, he proposes a considerable difference in normal stress as cause for the observed surface features: $N_2 = \theta_{zz} - \theta_{yy}$, for simple shear. The flow is along the x-direction. The velocity from the bed to the free surface varies along the z-direction, while the velocity transverse to the flow, which is approximately constant, is found along the y-direction.

6.1.5 Avalanche Rheology

To recapitulate observations made throughout this experimental study, avalanche flow is governed by specific characteristic phenomena: Ballotini at 50% relative humidity appeared to be partly fluidized for both forested and unforested trials. Additionally, the front and rear

of the avalanche had a low density where the dense flowing core was in the middle of the flow. The dense flowing for of alumina was much more spread out than for ballotini. Although no powder cloud formed, the materials were subject to immediate suspension upon entering the forest.

The lateral expansion of reference trials has a similar shape for ballotini, although for the forested trials, the width of alumina shrinking is a result of large fans at the start of the forest pushing material outward. This material settles and the remaining core flow density in the middle pushes forward. The general trend throughout the experiments is that 50% forest density accrues more mass on the surface of the forest zone, except for ballotini at 25% forest and 50% humidity. The observed behavior of flow height of ballotini compared to alumina with humidity variation was unexpected with respect to the Detrainment Approach. This issue would be better suited with the friction approach representing a dry flowing avalanche. In retrospect of replicating a noncompressible fluid, loosely packed snow has the ability to compress; therefore, as in nature, the particles are diverted laterally as compaction of the material unfolds, spreading out and envelops more surface area at a consequence of losing flow depth. There is a similar trend for 25% forest, however not as drastic, the trend proves less material was wedged at the forest front, so a larger bulk density flowed down the chute relatively unchallenged. The inclusion of forest effects in avalanche dynamics simulations is an important feature for avalanche hazard analysis, especially for frequent, small-to-medium avalanches. Forests play a crucial protective role by shortening the runout distance of such avalanches. In this paper we have compared two different approaches to quantify this role. The first theoretical method is to increase the friction parameters (Bartelt and Stockli, 2001); the second, which is utilized in this model, is to directly extract mass and its momentum from the flow that has been stopped by the trees. The rate of mass extraction is parameterized by a single coefficient, K, which depends on forest structure.

6.1.6 Protection Forest

As upsurges in population density stresses the local environment, protection forest will become an attractive answer to help keep communities safe and preserve the natural ecosystem within the alpine region. It is through silviculture that forest devastated via large avalanches, other natural disasters and human interaction are revitalized and restored promoting a healthy ecosystem for all inhabitants. As attention is given to potentially healthy trees, commercial thinning removes approximately 1/3 of the forest stand which could hinder ecosystem growth. During the final 20 year-long management cycles, a second commercial thinning, called shelter wood cut, removes nearly 1/2 the volume leaving behind a nurse crop for newly seeded plants to thrive.

Regarding this method of directly influencing healthy growth of the natural ecosystem, fuels management teams tend to remove tree groups which tend to grow alongside one another. However, this might be attractive for silviculture, this has a detrimental impact in decelerating avalanches in the alpine regions which are more susceptible to avalanche danger. Since tree grouping has proved to hinder avalanche flow more than any other phenomena, it is imperative to leave such grouping in a randomized fashion.

Furthermore, as climate change is likely to influence avalanche–forest interactions and their regional importance, a better understanding of these interactions in the light of climate change and potential management implications is increasingly needed (Bebi et al., 2009). Usually avalanches are triggered in extreme weather events where the snow depth accumulates all at once or precipitation falls and percolates through the snow cover causing active pore pressure pushing upwards on the wet shush. Therefore, predictions about future avalanche activities in a warmer climate must deal with large uncertainties and regional

characteristics of such extreme weather events in winter (Reardon et al., 2008).

Although it is not so easy to generalize such trends, nevertheless it is plausible that an increase in climate extremes will increase in the alpine regions and consequently snowballing the ratio of wet to dry avalanches. "On the other hand, in the event of an extreme warming scenario combined with a drastic increase of winter precipitation, more and perhaps heavier avalanches may start at high elevations", (Marty et al., 2007), which could ultimately form new avalanche paths. Considering the scenarios of both a rise and decline in avalanche activity as a result of climate change, would lead to important changes in forest structure and function (Bebi et al., 2009).

6.2 Recommendations for Further Work

As mentioned before, the detrainment approach, which is grounded on momentum extraction, seemed to be more reliable in comparison to the friction approach, which is functions on modified friction coefficients. Even so, the real-world application of the detrainment approach has two fundamental complications that are critical to overcome in future investigations.

First, it is unfortunate that this approach is only legitimate for small-to-medium avalanches trees are not destroyed and instead act as rigid obstacles. This is not always the circumstance in real world situations; thus, if at all possible, the model should govern the time and location where trees within the forest break. "This is not an easy task, as the breaking mode can vary from tree fracture to root upheaval and tree overturning. Furthermore, when the trees and other woody debris are entrained in the flow, they can become entangled in tree stands, leading to a complex flow state that is difficult, if not impossible, to model" (Feistl et al., 2014). Therefore, the model is restricted to certain cases where no entangled mass is stopped, does not account for momentum gains or increased destruction throughout the forest. The application of the model is therefore restricted to a specific flow case.

Second, it is apparent that the models outcomes are sensitive to the range of initial avalanche mass and snow characteristics. Granted, it is conceivable to back-calculate documented avalanches but remains a problematic to the simulation of small and medium avalanches, "which depends strongly on the size and location of the release zone, entrainment processes, snow properties and terrain features (which might be modified by avalanche deposits). Because of the strong variability of the initial and boundary conditions, as well as material properties, avalanche simulations that include forest effects should only be applied to selected problems" (Feistl et al., 2014).

The results are, however, very promising and will be reinforced by accumulating specific data during future field studies. Feistl plans on mapping the entire deposition area and quantifying mass piles behind individual tree clusters. "The exact structure of each tree group (location in forest, relative tree composition, tree diameter, branch density, tree spacing, low-lying vegetation) will be documented and correlated with the stopped mass. This will help to calibrate the K parameter, by linking structural features of the forest to mean deposition heights. (Feistl et al., 2014). Granulometry studies are desirable with respect deposition wedges and should provide insight to the jamming process to snow properties. To support the fieldwork previously carried out, small-scale granular chute experiments should be carried out to explore how detrainment in forest-like structures modifies momentum and energy fluxes of avalanches. (Feistl et al., 2014).

In regards to the small scale model, these suggestions should be investigated in full:

- ⚒ Drill an additional hole in between the current gap of 1cm. This would resemble the tree grouping provided by Feistl since there should be 3 trees within a 4 stem diameter

gap.

- ⚒ Improve the smoothness of the rounded parabola shaped transition from the forest to the runout zone.
- ⚒ Improvement to the chute would be the application of varying inclinations: less than 30 degree slope to minimize fluidization for ballotini and greater than 40 degrees for alumina.
- ⚒ It appears ≥65% relative humidity is best for ballotini.
- ⚒ Try photogrametry methods to measure surface speed via differing colored spheres. Lidar? Also, could be beneficial to map the change in deposition volume to correlate the Detrainment Approach to the physical model.
- ⚒ Gelatin trials at a lower humidity. This material was initially used in this study but were nonrepeatable since the powder accrued into balls and was difficult to handle at 55% humidity. The powder is neutral, very low density and non-static generating so there are similarities to snow.
- ⚒ Add broken trees flowing with avalanche to model.
- ⚒ Utilize 2 humidifiers to limit fluctuation.
- ⚒ Use different beads with more realistic properties than plastic.

6.2.1 Scaling

Avalanche behavior is scale-dependent (Iverson et al., 2004). Thus, scaling is critical for the applicability of laboratory tested results to real conditions. This means, that the avalanche model carried out on laboratory which is subject to this project will not fully represent avalanche behavior at geophysical scale and will need to be further developed with regard to scaling in the future. However, where the two main scaling issues - cohesion and intergranular fluid effects - are negligible, small-scale experiments are suited for modelling granular avalanches (Iverson et al., 2004). Designing those experiments, Iverson et al. (2004) conducted a scaling analysis to resolve the causes for this scale-dependency in granular avalanches composed of sand and air. To clarify the neglibility of intergranular cohesion and fluid effects and to analyze the variation in scale with and without these effects, scaling parameters have been derived. Having arbitrary magnitudes, those parameters are fundamental for evaluating the significance of cohesion and fluid effects and avalanche scale (Iverson et al., 2004). Iverson et al. (2004) assume a rigid, uniform slope with a two-dimensional, granular, fluid-saturated avalanche in downward motion. Further a uniform bulk density of the avalanche ρ, that the ambient flow effects are negligible and that the material properties of the avalanche do not change. Generally the theoretical knowledge of avalanche dynamics is assumed to be low. After Iverson et al. (2004), variables probably influencing the macroscopic avalanche dynamics are mostly related to physical avalanche properties, avalanche geometry and the avalanche's dynamic response. This dynamic response (u,τ) is assumed to be a function of the variables mentioned above:

$$(u,\tau) = f\left(g, L, H, \delta, \rho, \rho_s, \rho_f, D, \mu, \phi_{int}, \phi_{bed}, c, E, e, \theta\right)$$

Further, the granular aggregate's intrinsic hydraulic permeability k is expressed as $k = \mu D/E$, and its porosity n is formulated as $n = \left(\rho - \rho_s\right) / \left(\rho_f - \rho_s\right)$ Iverson et al. (2004).

The variables are further explained below (Table 6.1).

This gives four criteria for similarity:

$$\left(\frac{u}{\sqrt{gl}}, \frac{\tau}{\rho g h}\right) = f\left(N_P, N_R, c^*, E^*\right) \tag{6.1}$$

With:

$$N_P = \frac{\sqrt{g/l}}{\mu h^2/kE} \tag{6.2}$$

$$N_R = \frac{\rho h \sqrt{gl}}{\mu} \tag{6.3}$$

N_P is the timescale ratio of avalanche motion and excess pore pressure with k as hydraulic permeability of the granular material (Kahrs, 2015). N_R - a Reynolds number - includes the characteristic velocity of the avalanche $\sqrt{gl}$. The parameters c and E are normalized (*) by $\rho g h$, which is the characteristic stress (Kahrs, 2015). As Kahrs (2015) points out, for a pore fluid with a minimum viscosity of water, the critical parameter impacting avalanche motion on a geophysical scale will be the pore pressure, while it will be the viscosity for avalanche motion in a small-scale model. It is found that the effect of cohesive forces (e.g. electrostatic forces between grains and surfaces) is considerably more significant in modelling on laboratory scale than in large-scale conditions, while the effect of bulk stiffness is similar for both scales (Iverson et al., 2004).

Table 6.1: Dimensional Analysis of Avalanche Motion: Variables after citeIverson2004.

Variable	Definition	Dimensions	Units
c	intergranular cohesion	M/LT^2	Pa
D	hydraulic diffusivity of grain-fluid mixture	L^2/T	$m^2\ s^{-1}$
e	restitution coefficient of colliding grains		
E	bulk compressive stiffness of granular mixture	M/LT^2	Pa
g	magnitude of gravitational acceleration	L/T^2	$m\ s^{-2}$
H	avalanche thickness	L	m
L	avalanche length	L	m
u	magnitude of avalanche velocity (speed)	L/T	$m\ s^{-1}$
δ	typical grain diameter	L	m
θ	bed slope		degrees
μ	dynamic viscosity of intergranular fluid	M/LT	Pa s
ρ	bulk density of granular mixture	M/L^3	$kg\ m^{-3}$
ρ_s	bulk density of solid grains	M/L^3	$kg\ m^{-3}$
ρ_f	bulk density of intergranular fluid	M/L^3	$kg\ m^{-3}$
τ	magnitude of avalanche stress	M/LT^2	Pa
ϕ_{int}	internal friction angle of granular mass		degrees
ϕ_{bed}	basal friction angle of grains contacting bed		degrees

Due to the laboratory scale of this project and existing issues with regard to scaling theories and their applicability (Iverson et al., 2004), this project does not include the execution of scaling for the results found for the small-scale avalanche model that was used. Thus, with regard to the model presented by Iverson et al. (2004), future work objectives could include an assessment and analysis focusing further on the variables mentioned above: physical avalanche properties, avalanche geometry and the avalanche's dynamic response. This means, that the next step should be the development of a suitable scaling method for the small-scale results found in this project to make them applicable and available for large-scale conditions and avalanche bio-engineering.

Appendix A

MATLAB Code

```
clc; clear; close all;

rows = 144;
cols = 97;

density1=0.5;
M2 = zeros(rows,cols);
no_trees1 = floor(density1*rows*cols);
r = randperm(rows*cols,no_trees1);

for i=1:no_trees1
M2(r(i)) = 1;
end
print_matrix(M2);
fprintf('\n');

density2=0.25;
M1 = zeros(rows,cols);
no_trees2 = floor(density2*rows*cols);
r1=r(1:no_trees2);
for i=1:no_trees2
M1(r1(i)) = 1;
end
print_matrix(M1);
```

```
function forest_generator( density )

rows = 144;
cols = 97;
f = zeros(rows,cols);
no_trees = floor(density*rows*cols);
r = randperm(rows*cols,no_trees);

for i=1:no_trees
f(r(i)) = 1;
end
print_matrix(f);
end
```

Appendix B

Forest Configuration

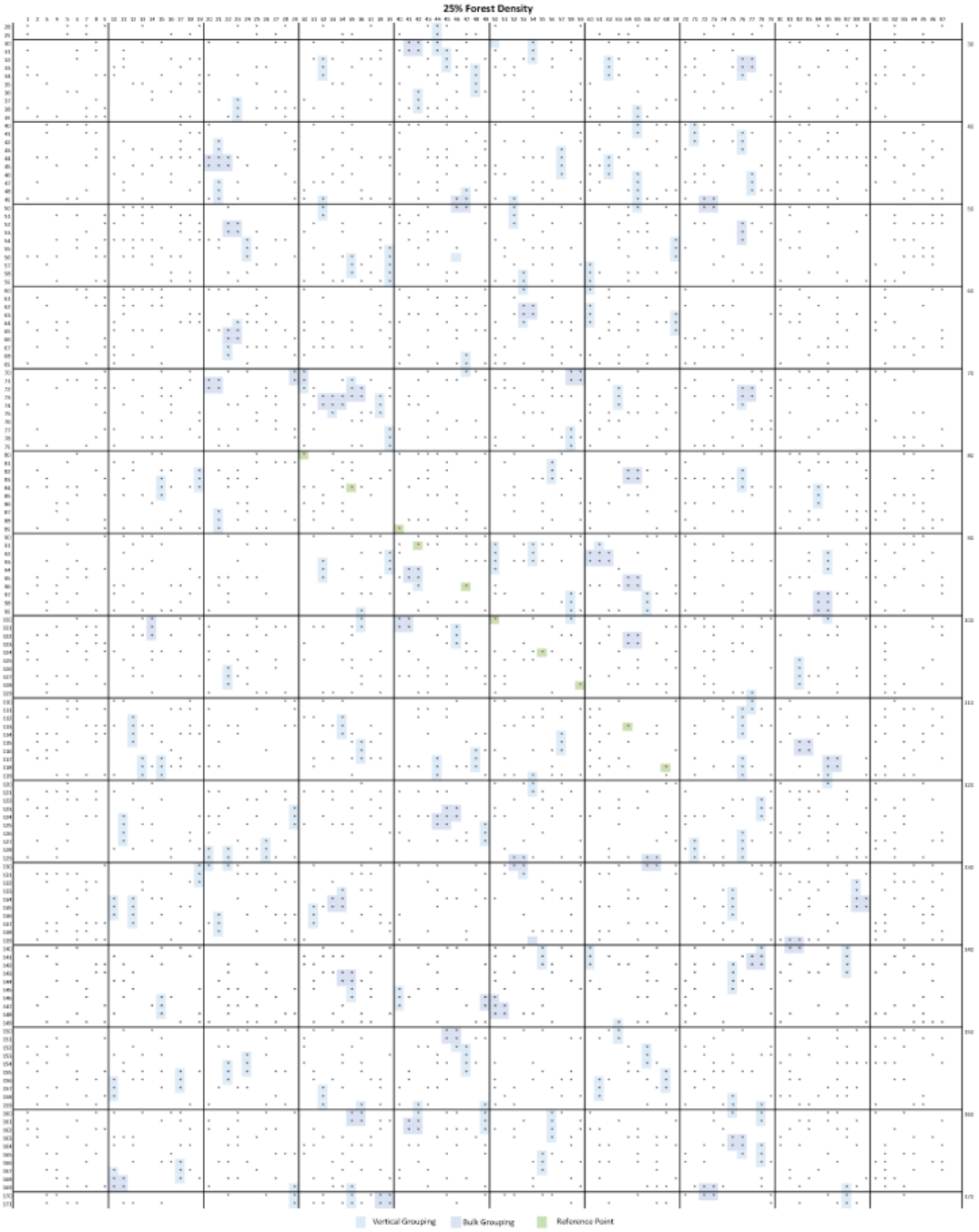
25% Forest Density
Vertical Grouping
Bulk Grouping
Reference Point

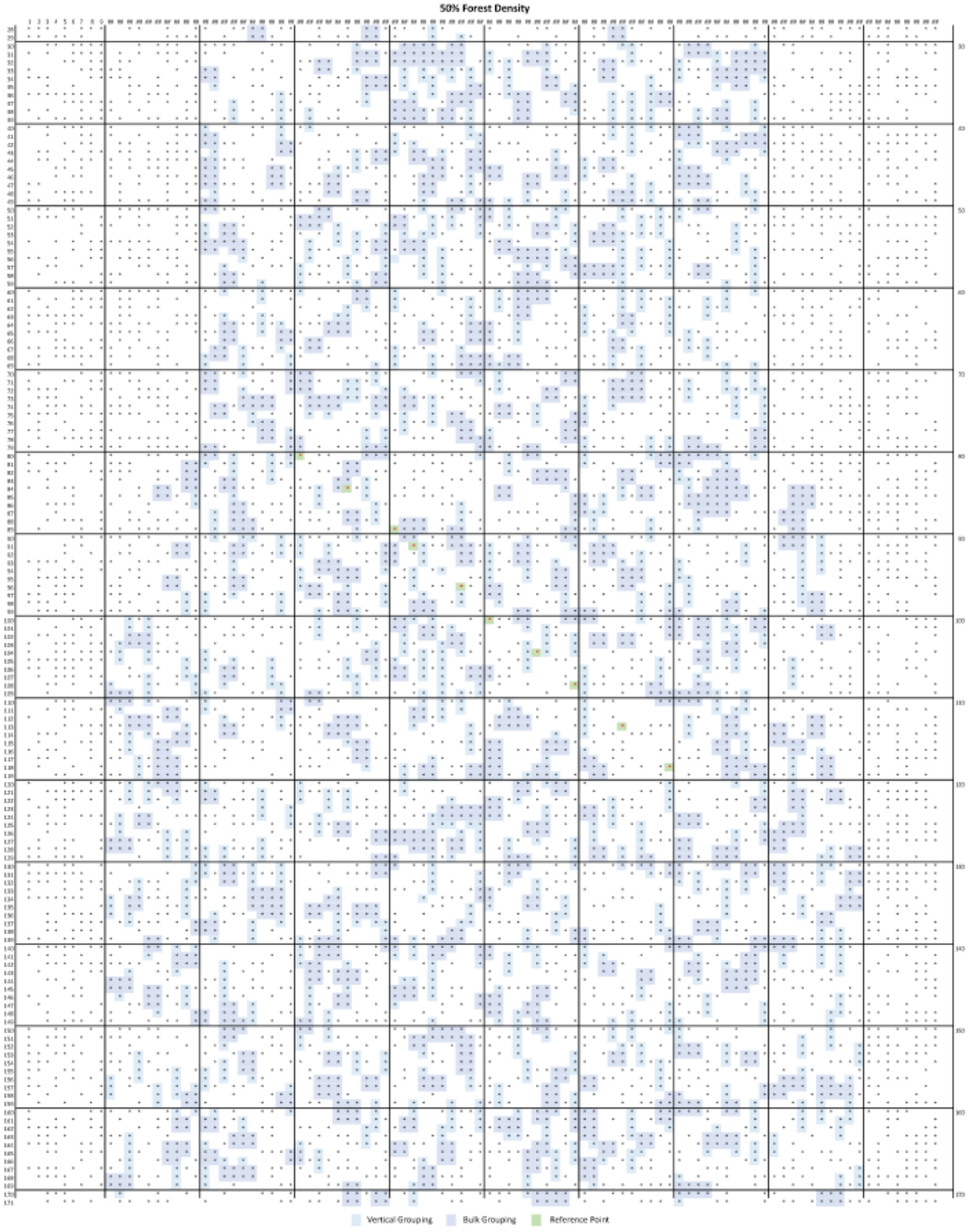
50% Forest Density
Vertical Grouping
Bulk Grouping
Reference Point

Appendix C

Ballotini: Experiment Snapshots

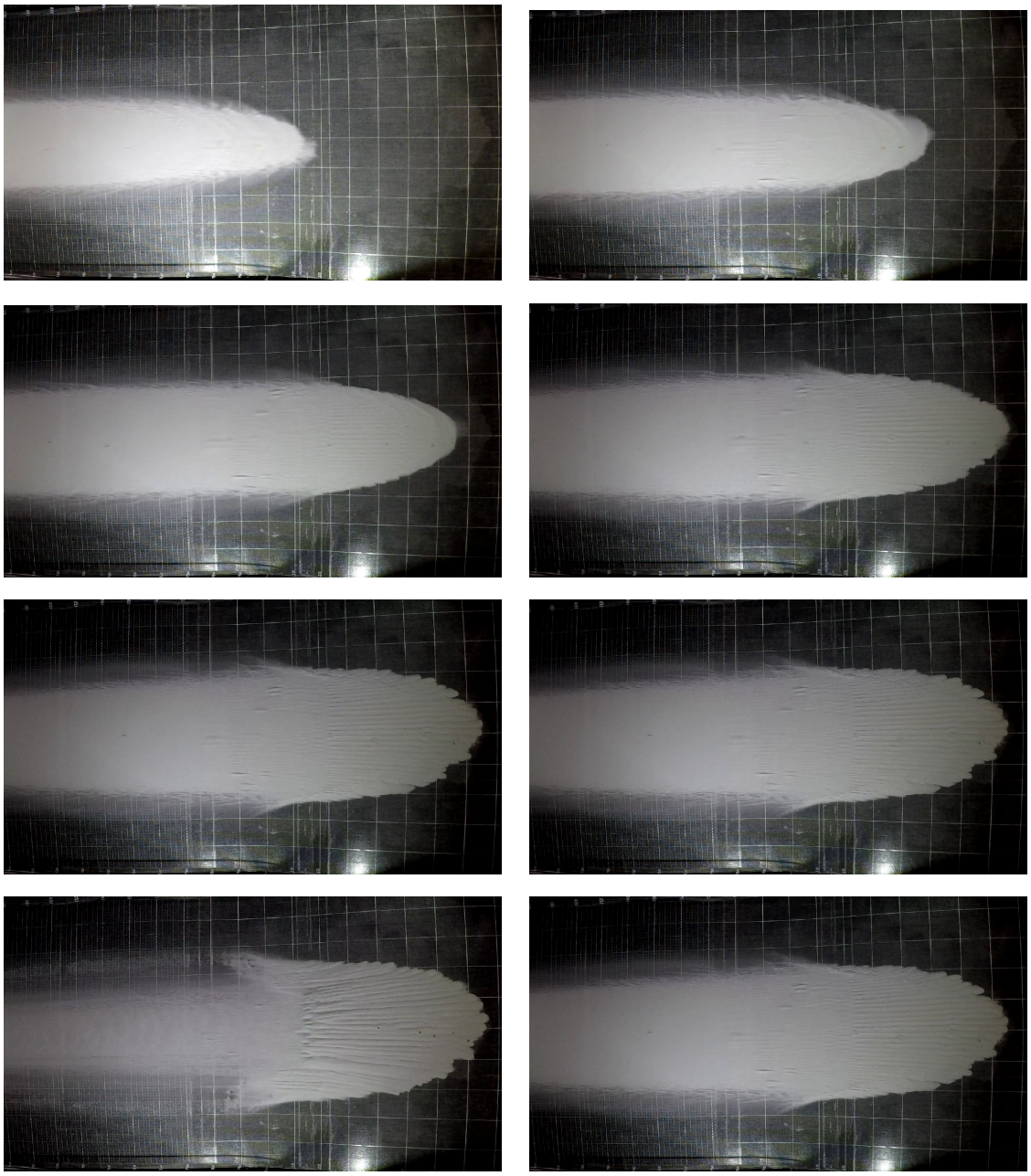

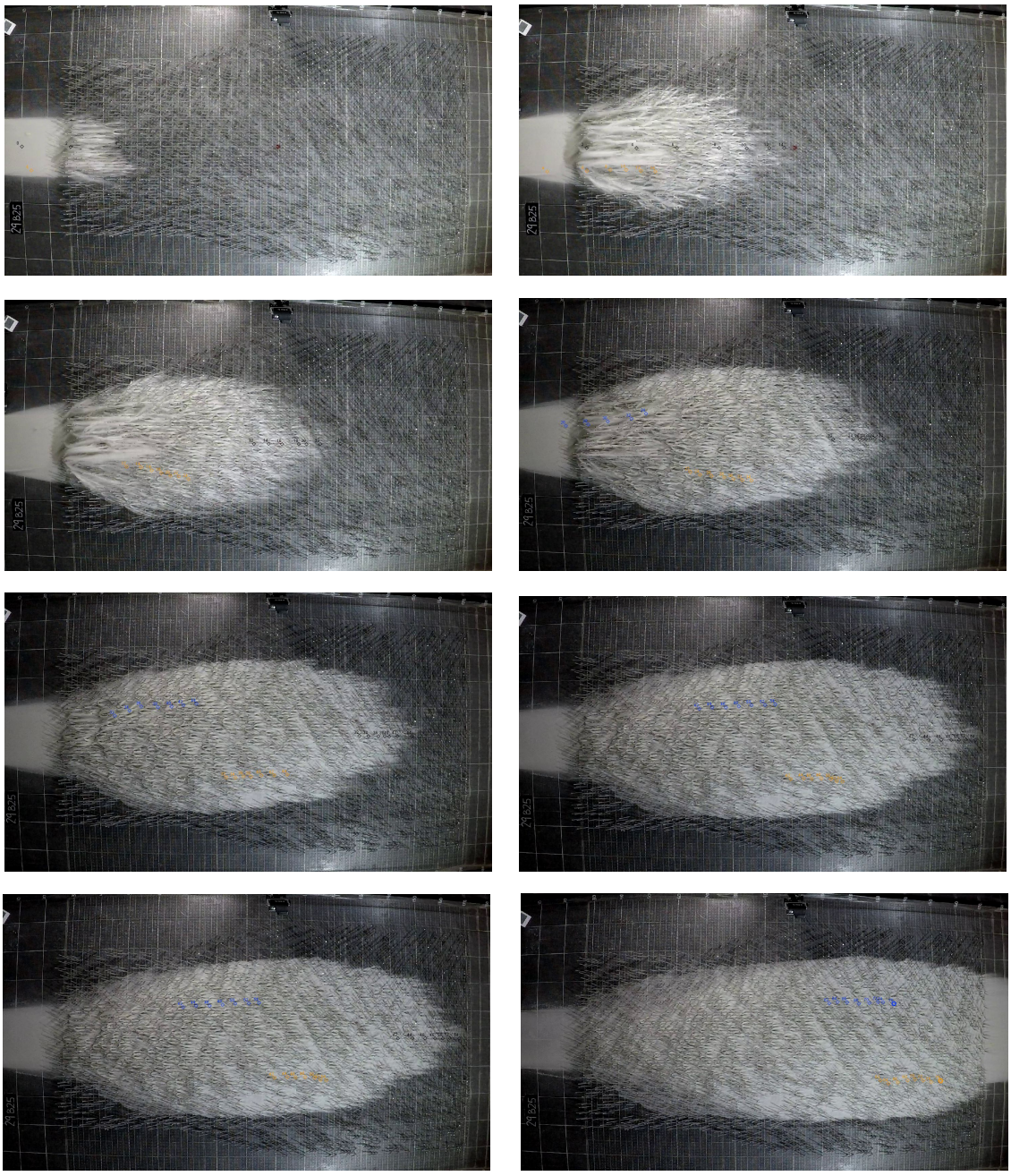

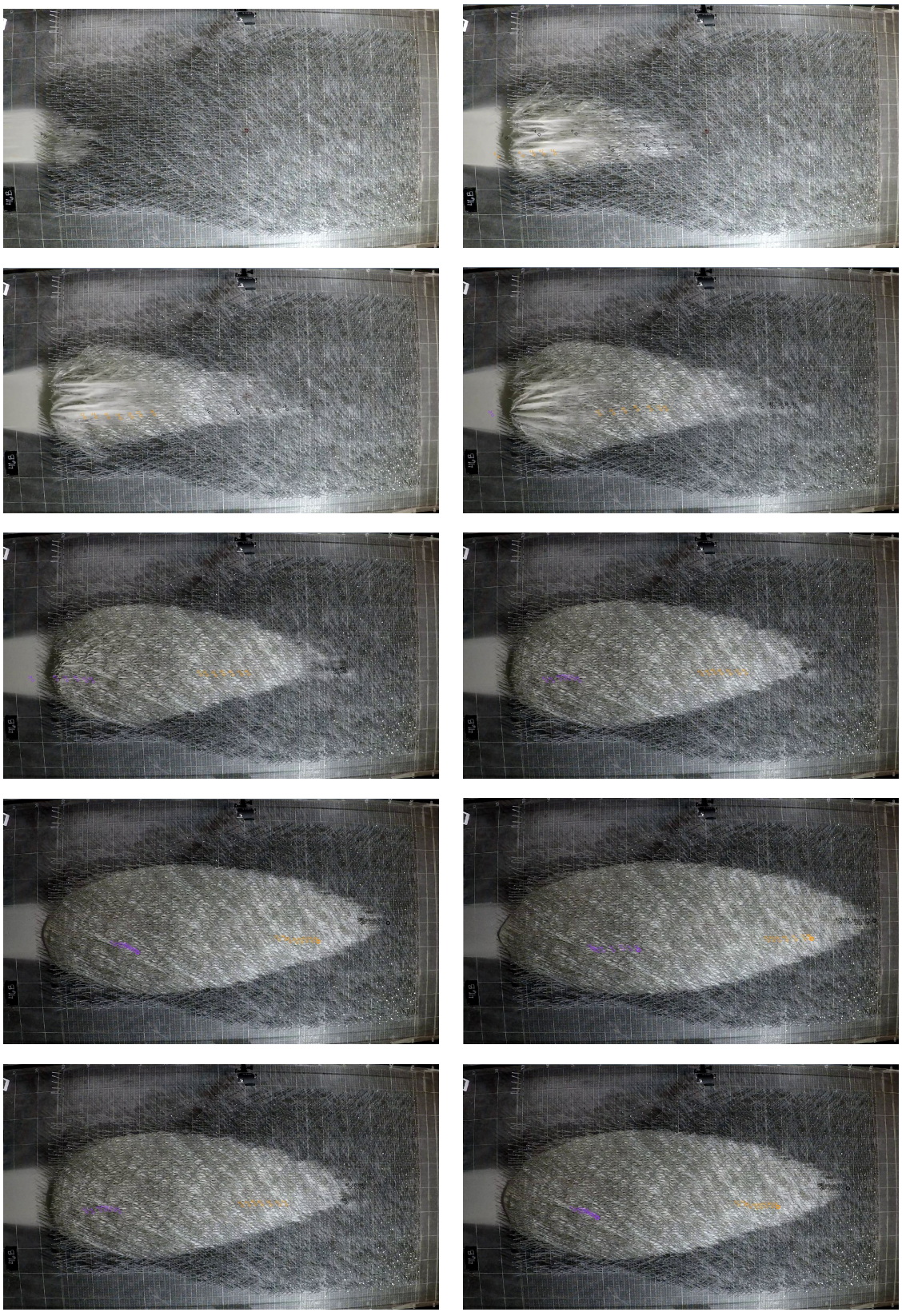

Appendix D

Raw Data

				Slope angle, Y°	Stem width, d (mm)	Wedge height, h_w (mm)	Wedge length, l_w (mm)	Top wedge angle, δ °	Wedge volume, W mm^3	Stem ratio (%)	Total Trees	Trees per category	Depostion volume cm^3	Initial volume cm^3	Extraction ratio (%)	Length, l m	h_d m	ρ (kg/m^3)	$\|v\|$ ms^{-1}	K-Value Pa
50% Relative Humidity	25% Forest	Ballotini	Single	35.0	3.2	1.7	5.0	53.8	15.2	0.02	2593	1	39.3	3000	1.3	1.5	0.0003	1583	0.840	0.243
			Vertical		9.6	2.2	7.5	51.3	33.2			3	28.7		1.0		0.0003			0.238
			Bulk		25.6	2.2	7.5	51.3	107.3			4	69.5		2.3		0.0003			0.258
		Alumina	Single		3.2	3.1	5.0	66.8	9.0			1	23.3	4200	0.6		0.0071	955	0.400	0.725
			Vertical		9.6	6.0	10.0	66.0	246.8			3	213.3		5.1		0.0072			0.738
			Bulk		25.6	6.0	10.0	66.0	798.1			4	517.3		12.3		0.0074			0.758
	50% Forest	Ballotini	Single	35.0	3.2	1.4	5.0	50.6	17.5	0.04	5185	1	90.5	3000	3.0	1.5	0.0005	1583	0.540	0.142
			Vertical		9.6	2.0	7.5	49.9	27.4			3	47.4		1.6		0.0004			0.133
			Bulk		25.6	2.0	7.5	49.9	88.7			4	115.0		3.8		0.0005			0.147
		Alumina	Single		3.2	3.0	5.0	66.0	9.2			1	47.9	4200	1.1		0.0054	955	0.351	0.426
			Vertical		9.6	5.0	10.0	61.6	171.4			3	296.2		7.1		0.0056			0.439
			Bulk		25.6	5.0	10.0	61.6	554.3			4	718.5		17.1		0.0059			0.461
60% Relative Humidity	25% Forest	Ballotini	Single	35.0	3.2	2.0	7.5	49.9	18.0	0.02	2593	1	46.7	3000	1.6	1.5	0.0004	1583	0.779	0.276
			Vertical		9.6	3.3	12.5	49.8	74.7			3	64.5		2.2		0.0004			0.284
			Bulk		25.6	3.3	20.0	44.4	199.0			4	129.0		4.3		0.0005			0.311
		Alumina	Single		3.2	3.1	7.5	57.5	13.0			1	33.7	4200	0.8		0.0072	955	0.380	0.664
			Vertical		9.6	7.0	15.0	60.0	335.9			3	290.3		6.9		0.0074			0.680
			Bulk		25.6	7.0	20.0	54.3	1086.3			4	704.1		16.8		0.0077			0.705
	50% Forest	Ballotini	Single	35.0	3.2	1.9	7.5	49.2	18.6	0.04	5185	1	96.5	3000	3.2	1.5	0.0009	1583	0.698	0.444
			Vertical		9.6	3.0	12.5	48.5	61.7			3	106.6		3.6		0.0009			0.448
			Bulk		25.6	3.0	20.0	43.5	199.5			4	258.6		8.6		0.0010			0.500
		Alumina	Single		3.2	4.2	7.5	64.2	9.9			1	51.4	4200	1.2		0.0056	955	0.299	0.321
			Vertical		9.6	5.8	15.0	56.1	230.6			3	398.6		9.5		0.0059			0.334
			Bulk		25.6	5.8	20.0	51.2	745.8			4	966.8		23.0		0.0062			0.355
70% Relative Humidity	25% Forest	Ballotini	Single	35.0	3.2	2.5	10.0	49.0	18.8	0.02	2593	1	48.7	3000	1.6	1.5	0.0008	1583	0.676	0.401
			Vertical		9.6	5.9	20.0	51.4	238.6			3	206.2		6.9		0.0009			0.452
			Bulk		25.6	5.9	25.0	48.3	636.3			4	412.4		13.7		0.0011			0.518
		Alumina	Single		3.2	3.5	10.0	54.3	14.9			1	38.6	4200	0.9		0.0086	955	0.379	0.789
			Vertical		9.6	7.3	20.0	55.1	365.3			3	315.7		7.5		0.0088			0.806
			Bulk		25.6	7.3	30.0	48.7	1181.5			4	765.7		18.2		0.0091			0.833
	50% Forest	Ballotini	Single	35.0	3.2	2.2	10.0	47.4	20.2	0.04	5185	1	104.9	3000	3.5	1.5	0.0043	1583	0.601	1.628
			Vertical		9.6	4.3	20.0	47.1	126.8			3	219.1		7.3		0.0043			1.657
			Bulk		25.6	4.3	30.0	43.2	409.9			4	531.3		17.7		0.0046			1.736
		Alumina	Single		3.2	4.4	10.0	58.7	12.3			1	63.7	4200	1.5		0.0061	955	0.316	0.391
			Vertical		9.6	8.1	20.0	57.0	449.8			3	777.3		18.5		0.0066			0.421
			Bulk		25.6	8.1	30.0	50.1	1454.6			4	1885.5		44.9		0.0074			0.468

Velocity Tracke	Forest Density	Trial	Entrain	M_t (g)	M_r (g)	M_{rec} (g)	M_d (g)	RH (%)	Temp (C°)	H_{start} (mm)	$H_{initial}$ (mm)	$Hmin_{flex}$ (mm)	$Hmax_{flex}$ (mm)	$H_{dynamic}$ (mm)	h_d (mm) H30	H50	H100	H170	H_{avg}	h_{wedge} (mm) Single	Group	Width (cm) Forest	Runout	Runout (cm)	Comments	
		1B		4000.5	3821.0	3978.8	168.7	50.0	16.6	55	6.8				0.3	0.3	0.3	0.3	0.3			51.0		94.5		
		2B		4000.5	3897.8	3994.5	99.7	52.0	17.2	50	6.5				0.3	0.3	0.3	0.3	0.3			53.0		97.5		
		3B		4001.0	3917.3	3993.9	80.1	51.0	17.4	50	6.0				0.3	0.3	0.3	0.3	0.3			54.0		102.5		
		4B		4001.0	3921.2	3985.5	72.1	50.0	17.4	50	6.2				0.3	0.3	0.3	0.3	0.3			55.0		100.5	After oven 3985	
		5B		4001.0	3754.7	3994.5	243.1	52.0	17.2	50	6.3				0.3	0.3	0.3	0.3	0.3			52.0		95.5	Oven baked 0% wc caused static electricity to gener	
		6B		4001.0	3805.7	3997.5	193.6	50.0	17.1	50	6.0				0.3	0.3	0.3	0.3	0.3			54.0		105.5	Sieved	
		7B		4001.0	3831.3	3999.0	168.7	47.0	17.7	50	6.5				0.3	0.3	0.3	0.3	0.3			54.0		101.5	Sieved	
		8B		4001.0	3729.5	3998.1	270.1	50.0	18.0	50	6.7				0.3	0.3	0.3	0.3	0.3			53.0		101.5	Oven baked 30 min, sieved. Entire path has a thin la	
	No Forest	9B		4001.0	3848.7	3994.5	149.1	50.0	17.9	50	6.5				0.3	0.3	0.3	0.3	0.3	1.3		54.0		103.0	Acceleration zone completely covered. (less than 8B	No Forest
		10B		4001.0	3886.5	4000.3	114.2	51.0	18.1	50	6.5				0.3	0.3	0.3	0.3	0.3	1.3		55.0		103.5	Much less detrainment than T9B	
		11B	x	4001.0	3838.0		163.0	50.0	19.8	50	6.6				0.3	0.3	0.3	0.3	0.3	1.3		53.5		102.5	Measuring entrainment. Flow height	
		12B	x	4001.0	3879.0		122.0	49.0	19.8	50	6.7	2.5	4.5	7.5	0.3	0.3	0.3	0.3	0.3	1.3		54.0		102.0	Flow height	
		13B	x	4001.0	3972.0		29.0	50.0	19.8	50	6.8	3.0	5.0	8.0	0.3	0.3	0.3	0.3	0.3	1.3		53.0		100.5	This trial is measuring entrainment and flow height	
		14B	x	4001.0	3854.1	4144.5	218.7	51.0	19.9	50	7.0	2.5	4.5	7.5	0.3	0.3	0.3	0.3	0.3	1.3		53.0		100.5	Will have to guess the entrainment since value was n	
		15A		4001.0	3432.7		568.3	49.0	20.4	70	5.0	1.5	4.5	6.5	0.9	0.9	0.9	0.9	0.9	5.5		37.0		49.5	Compaction possible. Initial start zone has Alumina	
		16A	x	4001.0	3893.5		107.5	49.0	20.3	70	6.0	1.5	4.5	6.5	0.9	0.9	0.9	0.9	0.9	5.5		41.0		52.5	Detrainment zone reaches farther upslope in V shape	
Void		17A	x	4001.0	3957.3		43.7	50.0	20.3	70	5.8	2.0	5.0	7.0	0.9	0.9	0.9	0.9	0.9	5.5		42.0		53.0	Less compaction at sart but still to level 2cm.	
		18A	x	4001.0	3889.7		111.3	52.0	20.4	70	5.0	1.5	4.5	6.5	0.9	0.9	0.9	0.9	0.9	5.0		43.0		51.5	Had a breach and lost material through the bottom sl	
		19A	x	4001.0	4020.0		-19.0	50.0	20.4	70	5.5	1.5	4.5	6.5	0.9	0.9	0.9	0.9	0.9	5.0		42.0		51.0	scooped too much runout	
		20A	x	4001.0	3936.5		64.5	48.0	20.5	70	6.0	2.0	5.0	7.0	0.9	0.9	0.9	0.9	0.9	4.5		41.5		52.5	Error due to start zone compaction	
		21A	x	4001.0	4041.8	4707.4	312.4	45.0	20.4	70	5.0	1.5	4.5	6.5	0.9	0.9	0.9	0.9	0.9	5.0		41.5		53.0	error due to initiation being more rough than usual.	
		22G		2308.1	2262.5		45.6	51.0	19.2	130	27.0	20.0	30.0	30.0	8.0		3.0		5.0	25.0		44		43.5		
		23G		2262.5	2371.5		-109.0	46.0	19.2	130	80.0	20.0	30.0	30.0	9.0		6.0		7.0	30.0		56.0		65.5	yellow is stuck just ahead of purple----> half way dov	
		24G		2371.5	2351.5		20.0	46.0	19.4	135	50.0	20.0	35.0	35.0	8.0		5.0		5.0	12.5		57.5		89.5	Pink 148. Blue stuck at the gate slide. Yellow and L	
		25G		2351.5	2337.0		14.5	47.0	19.5	140	75.0	20.0	40.0	40.0	9.0		5.5		7.0	15.0		49.0		76.5		
		26B25		4001.0	3667.2	3988.2	327.4	50.0	20.0	50	7.3	4.8	7.5	9.5	0.3	0.3	0.3	0.3	0.3	2.0	2.5	61.0		43.5		
		27B25		4001.0	3664.5	3995.0	333.5	52.0	20.1	50	7.5	5.0	8.0	10.0	0.3	0.3	0.3	0.3	0.3	1.5	2.0	60.5		43.5	pink 168 x 50	
		28B25		4001.0	3636.2	3997.1	362.9	60.0	20.5	50	7.3	5.0	7.0	9.0	0.4	0.4	0.4	0.5	0.4	2.0	3.5	60.5		43.0	orange ran thru	
	25% Forest	29B25		4001.0	3664.3	3986.4	329.4	50.0	19.9	50	7.3	4.8	7.5	9.5	0.3	0.4	0.3	0.4	0.4	1.5	2.0	61.5		44.0	Flow height 9mm	25% Forest
		30B25		4001.0	3302.2	4000.0	698.3	70.0	20.9	50	7.5	4.5	7.0	9.0	1.4	1.25	0.7	3.3	0.7	3.0	7.0	59.0		41.0	Ortho camera died half way thru. Flow height 10-12.	
		30$_2$B25		4001.0	3138.6	3992.4	858.1	70.0	19.8	50	8.0	4.5	8.0	10.0	1.0	1.25	0.7	3.3	0.8	3.0	7.0	58.5		39.5	After intensive cleaning runout was cleaner causing	
		31A25		4001.0	1369.5	3971.1	2616.6	70.0	21.1	70	7.0	3.0	6.0	8.0	21.7	5.8	2.0	5.4	8.7	4.0	8.0	57.0		31.5	Only blue made it to runout. P 76x50 Y 59x54 DG 3	
		32A25		4001.0	1466.1	3979.7	2524.3	60.0	31.1	70	8.0	3.5	6.5	8.5	19.0	5.0	1.5	3.6	7.3	3.3	8.0	57.0	59.5	31.5	Labeled wrong. Less bulging in the center than 31A.	
		33A25		4001.0	1490.7	3985.7	2502.7	50.0	20.9	70	8.0	3.5	7.0	9.0	17.3	5.6	1.5	5.6	7.5	3.0	6.0	57.0	60.0	31.0	Pink 41x28 O 143x40 Purp 152x45 Red 116x60 yell	
		34A25		4001.0	1455.5	3988.7	2539.4	50.0	21.1	70	7.8	3.5	7.0	9.0	15.7	5.4	2.6	3.0	6.7	3.3	6.0	57.0	60.0	31.5	Y 120x50 P 42x50 LG 29x45	
		35A25		4001.0	1445.5	3988.5	2549.3	60.0	21.4	70	8.0	4.0	6.8	8.8	19.0	2.1	1.4	5.8	7.1	3.0	6.0	57.0	60.0	31.5	P 46X50 Y74X54 O104X36 GREEN 147X32	
		36A25		4001.0	1590.0	3994.0	2407.5	70.0	19.7	70	7.5	3.0	6.0	8.0	20.7	6.2	1.1	6.0	8.5	3.0	6.5	57.0	60.5	31.5	Mass shifted to the right due to increased density. P/	
		37B25		4000.0	3678.9	3992.5	317.4	60.0	20.8	50	7.3	5.0	7	9	0.4	0.4	0.4	0.4	0.4	2.0	3.0	60.0		41.5	Minor compaction around start zone edges	
		38B25		4000.0	3356.9	3996.0	641.1	70.0	21.3	50	7.5	5.0	6.8	8.8	0.7	0.7	0.7	6.8	2.2	2.0	4.0	59.0		39.5	Mislabeled on vid	
		39B25		4000.0	3230.0	3995.8	767.9	71.0	21.1	50	8.0	4.5	6.5	8.5	3.2	0.7	0.7	5.4	2.5	2.0	5.5	58.5		39.0	LG 138X26 Look at photo on camera to oblserve co	
		40B50		4000.0	3745.5	3995.0	252.0	50.0	20.3	50	7.0	3.5	5.0	6.0	0.4	0.35	0.4	0.9	0.5	1.3	2.0	57.5	61.0	42.0	Friction method applicable	
		41B50		4000.0	3733.0	3996.0	265.0	50.0	20.4	50	7.2	4.0	5.5	6.5	0.3	0.30	0.3	0.5	0.3	1.5	2.0	57.5	60.0	43.0	O 120x37	
	50% Forest	42B50		4000.0	3642.0	3996.0	356.0	60.0	21.0	50	7.5	3.0	6.0	7.0	0.5	0.45	0.4	2.2	0.9	2.0	3.0	57.0		41.5	signs of initial detrainment compression wedge at sta	50% Forest
		43B50		4000.0	3350.6	3993.0	645.9	70.0	21.1	50	7.0	3.3	6.0	7.0	3.0	1.64	0.7	3.3	2.2	2.0	4.3	56.0		39.5	Error due to Ballotini not at 70rh since initial forest	
		44B50		4000.0	1923.8	3996.0	2074.2	70.0	21.4	50	7.0	3.0	6.5	7.5	12.3	5.60	0.7	1.5	5.0	2.5	4.5	54.5		36.5	Reason for short runout is mass stuck at top. Large i	
		45B50		4000.0	2425.7	3994.5	1571.6	70.0	21.7	50	7.2	3.0	7.0	8.0	12.7	5.94	0.7	2.3	5.4	2.0	4.0	56.0		36.5	Very large wedge at forest start but failed upon meas	
		46B50		4000.0	3633.1	3995.7	364.8	60.0	21.4	50	7.2	3.5	6.0	7.0	0.5	0.50	0.4	1.5	0.7	1.8	3.0	57.5		41.0	G 160x41	
		47A50		4000.0	1268.0	3982.5	2723.3	50.0	18.2	70	7.5	3.0	4.0	4.5	11.8	4.80	1.9	2.8	5.3	3.0	5.0	56.0	52.0	26.5	Look at width drawing. Initial compaction length 35	
		48A50		4000.0	918.0	3994.0	3079.0	50.0	19.5	70	7.8	3.3	4.5	5.0	12.2	5.70	1.7	2.4	5.5	3.0	5.0	54.0	52.0	27.0	Some wedge height up to 25mm in tree group (5,12,	
		49A50		4000.0	623.0	3995.5	3374.8	60.0	19.0	70	8.2	3.2	4.0	4.5	14.5	4.90	1.5	1.8	5.7	3.0	4.0	53.0	48.5	26.0	DG 90x48 B 32x60 R 52x64 LG 28x38. Strange to s	
		50A50		4000.0	611.6	3991.5	3384.2	60.0	19.4	70	7.5	3.3	4.0	4.3	14.6	4.50	1.4	1.6	5.5	5.3	7.5	52.0	49.0	26.5	Large mass compacted in start zone edges. P 149x50	
		51A50		4000.0	564.5	3991.6	3431.3	70.0	19.4	70	7.8	3.0	3.5	4.0	15.0	5.40	1.7	2.1	6.1	5.7	7.0	53.0	49.0	26.5	Track Purp 162x34 R 50x58 B48x68 DG 55x50 LG	
		52A50		4000.0	566.0	3998.5	3433.3	70.0	19.7	70	8.0	2.8	3.3	3.8	15.0	6.10	1.6	1.5	6.1	3.2	9.3	53.0	48.5	26.0	R/O ran to bottom. Y 48x58 P 48x50 B 32x62 Purp	
		53B		4000.0	3693.3	3990.0	301.7	60.0	19.0	50	6.0	2.0	3.0	7.5	0.5	0.50	0.4	0.4	0.5	1.3		50.0		89.5		
		54B		4000.0	3705.0	3996.0	293.0	60.0	19.1	50	7.0	1.5	2.5	7.0	0.5	0.50	0.4	0.4	0.5	1.3		51.0		90.0	Film height was 0.5 from 20cm initial to 30cm at run	
		55B		4000.0	3440.7	3997.2	557.9	70.0	19.5	50	6.8	1.8	3.0	8.0	0.7	0.7	0.7	0.7	0.7	3.0		50.5		81.5	There were streaks of 1mm grouping where the rest	
	No Forest	56B		4000.0	3435.5	3994.0	561.5	70.0	19.5	50	7.5	2.0	3.0	8.0	0.7	0.7	0.7	0.7	0.7	3.0		51.0		83.5		No Forest
		57A		4000.0	3097.5	3987.3	896.2	70.0	19.6	70	7.5	2.5	3.0	8.0	1.0	1.00	1.0	3.2	1.6	2.9		43.5		55.0	Start zone compression ran to runout zone so H170	
		58A		4000.0	3083.4	3995.0	914.1	70.0	19.6	70	6.8	2	3	8	1.0	1.00	1.0	3.6	1.7	2.6		43.0		54.5		
		59A		4000.0	3311.5	3996.1	686.6	60.0	19.6	70	7.0	2.5	2.5	8.0	1.0	1.00	0.9	3.9	1.7	2.7		43.5		55.5		
		60A		4000.0	3273.0	3994.0	724.0	60.0	19.7	70	6.8	2.3	2.5	8.5	0.9	0.90	0.9	4.3	1.8	2.6		43.0		55.0	Actual height of stem is 8mm at the 10mm mark (fro	
		61A		4000.0	3326.0	3995.0	671.5	50.0	19.7	70	6.8	1.8	2.3	7.5	0.9	0.90	0.9	4.8	1.9	2.3		43.0		55.5	Values seem to be too similar to 60A. Possibly did n	
		62A		4000.0	3362.0	3996.0	636.0	50.0	19.7	70	7.0	1.8	2.2	7.0	0.8	0.80	0.8	3.0	1.4	2.3		43.5		57.0	Alumina much drier than 61A so runout and width i	

				Slope angle, Υ	Stem width, d	Wedge height, h_w	Wedge length, l_w	Top wedge angle,	Wedge volume, W	Stem ratio	Total Trees	Trees per category	Depostion volume	Initial volume	Extraction ratio	Length, l	Mean dep. Height, h_d	Dendity, ρ	Mean Velocity $\lVert v \rVert$	K-Value	Ratio Observed	M_{wedge}	$M_{d\_average}$	M_d Corrected	$M_{d\_average}$ Corrected	M_d Observed	M_d Corrected	M_{d_max}	Ratio corrected	Error
				°	(mm)	(mm)	(mm)	°	mm^3	(%)			cm^3	cm^3	(%)	m	m	(kg/m^3)	ms^{-1}	Pa	(%)	(g)	(g)	(g)	(g)	(g)	(g)	(g)	(%)	(%)
50% Relative Humidity	25% Forest	Balotini	Single	35.0	3.2	1.7	5.0	53.8	15.2	0.02	2593	1	39.3	3000	1.3	1.5	0.0003	1583	0.840	0.243	0.33	62.18	72.55	147.22	149.19	330.11	330.11	446.13	0.74	54.80
			Vertical		9.6	2.2	7.5	51.3	33.2			3	28.7		1.0		0.0003			0.238	0.33	45.39		144.03			330.11	436.46	0.76	
			Bulk		25.6	2.2	7.5	51.3	107.3			4	69.5		2.3		0.0003			0.258	0.33	110.09		156.33			330.11	473.72	0.70	
		Alumina	Single		3.2	3.1	5.0	66.8	9.0			1	23.3	4200	0.6		0.0071	955	0.400	0.725	0.25	22.21	239.96	2432.99	2484.97	2521.00	2521.00	9731.96	0.26	1.43
			Vertical		9.6	6.0	10.0	66.0	246.8			3	213.3		5.1		0.0072			0.738	0.25	203.67		2476.30			2521.00	9905.21	0.25	
			Bulk		25.6	6.0	10.0	66.0	798.1			4	517.3		12.3		0.0074			0.758	0.25	494.01		2545.61			2521.00	10182.42	0.25	
	50% Forest	Balotini	Single	35.0	3.2	1.4	5.0	50.6	17.5	0.04	5185	1	90.5	3000	3.0	1.5	0.0005	1583	0.540	0.142	0.40	143.25	133.41	251.84	249.57	258.50	258.50	629.60	0.41	3.45
			Vertical		9.6	2.0	7.5	49.9	27.4			3	47.4		1.6		0.0004			0.133	0.40	75.02		236.12			258.50	590.30	0.44	
			Bulk		25.6	2.0	7.5	49.9	88.7			4	115.0		3.8		0.0005			0.147	0.40	181.97		260.76			258.50	651.90	0.40	
		Alumina	Single		3.2	3.0	5.0	66.0	9.2			1	47.9	4200	1.1		0.0054	955	0.351	0.426	0.35	45.79	338.26	2600.28	2698.01	2901.13	2901.13	7429.36	0.39	7.00
			Vertical		9.6	5.0	10.0	61.6	171.4			3	296.2		7.1		0.0056			0.439	0.35	282.87		2679.50			2901.13	7655.72	0.38	
			Bulk		25.6	5.0	10.0	61.6	554.3			4	718.5		17.1		0.0059			0.461	0.35	686.12		2814.26			2901.13	8040.74	0.36	
60% Relative Humidity	25% Forest	Balotini	Single	35.0	3.2	2.0	7.5	49.9	18.0	0.02	2593	1	46.7	3000	1.6	1.5	0.0004	1583	0.779	0.276	0.43	73.94	126.75	250.61	263.54	340.10	340.10	589.67	0.58	22.51
			Vertical		9.6	3.3	12.5	49.8	74.7			3	64.5		2.2		0.0004			0.284	0.43	102.12		257.51			340.10	605.91	0.56	
			Bulk		25.6	3.3	20.0	44.4	199.0			4	129.0		4.3		0.0005			0.311	0.43	204.18		282.49			340.10	664.69	0.51	
		Alumina	Single		3.2	3.1	7.5	57.5	13.0			1	33.7	4200	0.8		0.0072	955	0.380	0.664	0.25	32.21	327.27	2469.57	2540.00	2536.78	2536.78	9878.28	0.26	0.13
			Vertical		9.6	7.0	15.0	60.0	335.9			3	290.3		6.9		0.0074			0.680	0.25	277.21		2528.05			2536.78	10112.20	0.25	
			Bulk		25.6	7.0	20.0	54.3	1086.3			4	704.1		16.8		0.0077			0.705	0.25	672.40		2622.38			2536.78	10489.52	0.24	
	50% Forest	Balotini	Single	35.0	3.2	1.9	7.5	49.2	18.6	0.04	5185	1	96.5	3000	3.2	1.5	0.0009	1583	0.698	0.444	0.30	152.70	243.64	354.64	370.35	360.38	360.38	1182.13	0.30	2.77
			Vertical		9.6	3.0	12.5	48.5	61.7			3	106.6		3.6		0.0009			0.448	0.30	168.80		357.42			360.38	1191.40	0.30	
			Bulk		25.6	3.0	20.0	43.5	199.5			4	258.6		8.6		0.0010			0.500	0.30	409.43		399.00			360.38	1330.00	0.27	
		Alumina	Single		3.2	4.2	7.5	64.2	9.9			1	51.4	4200	1.2		0.0056	955	0.299	0.321	0.38	49.07	450.98	2889.77	3033.67	3379.45	3379.45	7706.04	0.44	10.23
			Vertical		9.6	5.8	15.0	56.1	230.6			3	398.6		9.5		0.0059			0.334	0.38	380.63		3008.48			3379.45	8022.60	0.42	
			Bulk		25.6	5.8	20.0	51.2	745.8			4	966.8		23.0		0.0062			0.355	0.38	923.25		3202.75			3379.45	8540.68	0.40	
70% Relative Humidity	25% Forest	Balotini	Single	35.0	3.2	2.5	10.0	49.0	18.8	0.02	2593	1	48.7	3000	1.6	1.5	0.0008	1583	0.676	0.401	0.50	77.06	352.12	569.28	648.50	741.35	741.35	1138.56	0.65	12.53
			Vertical		9.6	5.9	20.0	51.4	238.6			3	206.2		6.9		0.0009			0.452	0.50	326.43		641.10			741.35	1282.20	0.58	
			Bulk		25.6	5.9	25.0	48.3	636.3			4	412.4		13.7		0.0011			0.518	0.50	652.87		735.11			741.35	1470.22	0.50	
		Alumina	Single		3.2	3.5	10.0	54.3	14.9			1	38.6	4200	0.9		0.0086	955	0.379	0.789	0.30	36.87	356.54	3539.26	3630.82	2512.03	2512.03	11797.53	0.21	44.54
			Vertical		9.6	7.3	20.0	55.1	365.3			3	315.7		7.5		0.0088			0.806	0.30	301.48		3615.05			2512.03	12050.17	0.21	
			Bulk		25.6	7.3	30.0	48.7	1181.5			4	765.7		18.2		0.0091			0.833	0.30	731.27		3738.16			2512.03	12460.52	0.20	
	50% Forest	Balotini	Single	35.0	3.2	2.2	10.0	47.4	20.2	0.04	5185	1	104.9	3000	3.5	1.5	0.0043	1583	0.601	1.628	0.40	166.11	451.33	2336.03	2401.74	1430.55	1430.55	5840.07	0.24	67.89
			Vertical		9.6	4.3	20.0	47.1	126.8			3	219.1		7.3		0.0043			1.657	0.40	346.78		2377.66			1430.55	5944.14	0.24	
			Bulk		25.6	4.3	30.0	43.2	409.9			4	531.3		17.7		0.0046			1.736	0.40	841.10		2491.55			1430.55	6228.86	0.23	
		Alumina	Single		3.2	4.4	10.0	58.7	12.3			1	63.7	4200	1.5		0.0061	955	0.316	0.391	0.40	60.81	867.94	3360.44	3668.69	3432.28	3432.28	8401.10	0.41	6.89
			Vertical		9.6	8.1	20.0	57.0	449.8			3	777.3		18.5		0.0066			0.421	0.40	742.36		3620.73			3432.28	9051.83	0.38	
			Bulk		25.6	8.1	30.0	50.1	1454.6			4	1885.5		44.9		0.0074			0.468	0.40	1800.66		4024.91			3432.28	10062.27	0.34	

Appendix E

Material Specification: Alumina

DADCO

Material Specification : Smelter Grade Alumina

SGA

Chemical and Physical Analysis		Typical Value	Limit	Method
Al_2O_3	%	98,5	≥ 98	Dif.*
SiO_2	%	0,011	≤ 0,015	XRF*
Fe_2O_3	%	0,013	≤ 0,020	XRF*
TiO_2	%	0,002	≤ 0,003	XRF*
CaO	%	0,004	≤ 0,010	XRF*
Na_2O	%	0,30	≤ 0,38	XRF*
L.O.I. [1)] (300° - 1000° C)	%	0,70	≤ 1,0	ISO 806
Bulk Density	kg/m^3	955	930 – 1000	ISO 903
Angle of Repose	°	33	32 – 36	ISO 902
Specific Surface Area BET	m^2/g	75	67 – 83	ISO 9277
Granulometry < 45 µm	%	10	≤ 15	ISO 13320-1
[1)] L.O.I. at the time of production * Data of dried material (105° C)				

General Information

Appearance
White free-flowing powder

Packaging
Bulk delivery

Safety Information
This product is non-hazardous, non-toxic and not inflammable. Since legislation may vary from country to country the specific instructions have to be adhered to.

Handling & warehousing
Due to the hygroscopic nature of the product, proper handling and warehousing are necessary.

REACH reference number
01-2119529248-35-0020

Appendix F

Material Specification: Rustoleum

PRODUCT DATA — COMBICOLOR® METAL 7300/7400

DESCRIPTION

RUST-OLEUM® CombiColor Metal 7300/7400 coating is primer and topcoat in one, based on a urethane modified alkyd, providing good drying properties at low temperatures.
The product contains rust-inhibitive pigments and is lead- and chromate free.

RECOMMENDED USES

RUST-OLEUM CombiColor Metal 7300/7400 should be applied on bare, manually derusted or with CombiPrimer Anti-Corrosion 3369/3380 primed steel. CombiColor Metal is intended for brush and roller application and can also be applied by air spray.
RUST-OLEUM CombiColor Metal 7300/7400 offers corrosion protection in a light industrial environment.
For metal structures in a more aggressive industrial environment, prior application of a RUST-OLEUM CombiPrimer Anti-Corrosion 3369/3380 is recommended.

TECHNICAL DATA

Appearance:	High gloss, Satin (black and white), Flat (black and white).
Colour:	See colour card. Satin and High gloss are also available as tint base.
Density:	High gloss/flat: 1.07 kg/l. ± 0.09 depending on colour Satin: 1,22 kg/l. ± 0,10 depending on colour
Solids Content:	High gloss/flat: 54.6% by volume ± 2.0 depending on colour Satin: 50,6 volume % ± 2,0 depending on colour
Viscosity:	High gloss/flat: 100 - 104 KU / Krebs Stormer Units at 20°C Satin: 86 - 91 KU /Krebs Stormer Units bij 20°C
Recommended film thickness:	55 µm dry, equals 100 µm wet
VOC-content:	439 g/l max.
Ready-to-use mixture:	495 g/l max.
Category:	A/i
EU Limit values:	600 g/l (2007) / 500 g/l (2010)

Drying times	20°C/50% r.h.	10°C/60% r.h.	30°C/50% r.h.
To touch:	2 hours	3 hours	1 ½ hours
To handle:	8 hours	16 hours	6 hours
To recoat:	After 16 hours	After 24 hours	After 8 hours
Full hardness	7 days	14 days	5 days

Heat resistance: 90°C (dry heat), at elevated temperatures discoloration may occur.

Coverage

Theoretical:	10.3 m²/l at 55 µm dry, depending on colour.
Practical:	Practical coverage depends on many factors such as porosity and roughness of the substrate and material losses during application.

SURFACE PREPARATION

Remove oil, grease and all other surface contaminations by alkaline or high pressure (steam) cleaning in combination with appropriate detergents. Remove rust scale, loose mill scale, loose rust and loose coatings by scraping and wire brushing to St 3 (ISO 8501-1 : 1988), light blast cleaning or sanding. Sand intact coatings to roughen the surface slightly.
The surface must be clean and dry during application. Galvanised, Zinc and Aluminium surfaces have to be primed first with CombiPrimer Tack Coat 3302.

Appendix G

Material Specification: Ballotini

SiLibeads Glass beads Type S Version: V2/2017

Product Data Sheet

First created on: 2017-04-06 Updated on: 2017-05-08
Next inspection on: 2017-12-31 Printed on: 2017-05-08

SIGMUND LINDNER

Produkt	**SiLibeads Glass beads Type S**
Material	polished Glass beads made of soda lime glass Specific weight: 2.50 kg/l Hydrolytic resistance on Glass beads: HGB 2 (based on DIN ISO 720) Acidic resistance on Glass beads: S2 (according to DIN 12116) Alcaline resistance on Glass beads: A1 (according to DIN ISO 695)
Application	Grinding and dispersing media in horizontal and vertical pearl mills for the wet grinding of paints, pigments, dyestuff, ink, agro-chemicals and minerals; Filling material in the chemical-, paper- and synthetic materials industry; Filling material for the modification of the physical properties of thermoplast and duroplast Reflection beads for road marking (in diameters > 0.8 mm), specially to improve the visibility at night in case of rain, Type II marking; Polishing agent for optical and interocular lenses; diameters between 0.3 - 0.4 mm and 0.4 - 0.6 mm show excellent results; Glass beads for shot peening of the surface of metal, plastics, ceramics and wood; and further technical applications
Technical Data	
Roundness	≥ 0.95 (ratio width/length (x_{min}/x_{max})
Compressive strength	up to 2.100 N (belonging to diameter, see table Standard Sizes)
Refractive index	1.52
Size (Diameter)	between 0.25 – 4.40 mm (see table Standard Sizes)
Transformation temperature	549 °C
Softening point (Littleton point)	734 °C
Melting point	1446 °C
Specific thermal Conductivity	1.129 W/km
Thermal expansion	9.05 10^{-6} K^{-1} [20 °C] (Coefficient of linear expansion **α**)
Specific thermal capatcity	1.329 kJ/kg K [>600 °C]
Youngs-Module	63 GPa
Hardness according to Mohs	≥ 6
Surface	polished (uncoated); surface-coating with silane/siloxane is possible on request

Assessment acc. to Food Legislation

The Glass beads are a consumer good in the sense of §2 clause 6 no. 1 German Code for Food Stuff (LFGB), Commodities and Feeding Stuff. Therefore they have to comply with the legal requirements.

The Glass beads comply with the requirements § 31 of the German Food and Feed Code (LFGB) and of the European Food Regulation 1935/2004/EC, Article 3.

Chemical Analysis; Glass beads made of soda lime glass; CAS-Nr. 65997-17-3 / EINECS 266-046-0

Name	Method	Weight	CAS-No.	EINECS
Silicon dioxide SiO_2	DIN 51001	72.30 %	7631-86-9	231-545-4
Sodium oxide Na_2O	DIN 51001	13.30 %	1313-59-3	215-208-9
Calcium oxide CaO	DIN 51001	8.90 %	1305-78-8	215-138-9
Magnesium oxide MgO	DIN 51001	4.00 %	1309-48-4	215-171-9
further		1.50 %		

SiLibeads Glass beads Type S

Product Data Sheet

Version: V2/2017

First created on: 2017-04-06 Updated on: 2017-05-08
Next inspection on: 2017-12-31 Printed on: 2017-05-08

SIGMUND LINDNER

The heavy metal content of the Glass beads keeps the permitted limits of EU directive 2011/65/EC (RoHS).

Lead < 1000 ppm Cadmium < 100 ppm Chrome VI < 1000 ppm Mercury < 1000 ppm

Standard Sizes –special diameters available by request

Article	Diameter	Resistance to compression *)	Bulk density	Amount (pcs. per kg)
4501	0.25 – 0.50 mm	---------	1.46 kg/l	14.486.600
45015	0.40 – 0.60 mm	---------	1.47 kg/l	6.111.500
4502	0.50 – 0.75 mm	---------	1.49 kg/l	3.129.100
4503	0.75 – 1.00 mm	---------	1.50 kg/l	1.140.300
4504	1.00 – 1.30 mm	250 – 350 N	1.51 kg/l	502.300
4505	1.25 – 1.65 mm	350 – 500 N	1.51 kg/l	250.580
4506	1.55 – 1.85 mm	500 – 650 N	1.52 kg/l	155.490
4507	1.70 – 2.10 mm	600 – 750 N	1.52 kg/l	111.370
4508	2.00 – 2.40 mm	750 – 900 N	1.53 kg/l	71.740
4510	2.40 – 2.90 mm	950 – 1100 N	1.53 kg/l	41.050
4511	2.85 – 3.45 mm	1100 – 1450 N	1.53 kg/l	24.440
4512	3.40 – 4.00 mm	1450 – 1650 N	1.53 kg/l	15.080
4513	3.80 – 4.40 mm	1700 – 2100 N	1.53 kg/l	11.080

*) Resistance to compression: internal test with Compressive strength inspector No. 10004.1, Company Hegewald & Peschke

Additional Information	
Storage indication	Store in a dry manner in closed (original) container by room temperature.
Disposal	Please consult national laws and local regulations in force for disposal or landfill.
Safety advice	High risk of slipping due to spillage of product
Product information	Sample card … glass beads for technical applications, Safety Data Sheet SiLibeads Type S, Microglass; Test Reports
Manufacturer/Supplier	Sigmund Lindner GmbH; Oberwarmensteinacher Strasse 38; 95485 Warmensteinach / GERMANY Phone: +49-9277-9940 Fax: +49-9277-99499 E-Mail: sili@sigmund-lindner.com Web: www.sili.eu

All data are reference values – subject to change without prior notice

Appendix H

Triboelectric Series

H.1 Triboelectric Series: Part I

TriboElectric Table

Column 1 (this col.): Insulator name. Col.2: Charge affinity in nC/J (nano ampsec/wattsec of friction). Col.3: Charge acquired if rubbed with metal (W=weak, N=normal, or consistent with the affinity). Col.4: Notes.	Affinity nC/J	Metal effect	**Triboelectric Table** Tests were performed by Bill Lee (Ph.D., physics). ©2009 by AlphaLab, Inc. (TriField.com), which also manufactured the test equipment used. This table may be reproduced only if reproduced in whole.
Polyurethane foam	+60	+N	All materials are good insulators (>1000 T ohm cm) unless noted.
Sorbothane	+58	-W	Slightly conductive. (120 G ohm cm).
Box sealing tape (BOPP)	+55	+W	Non-sticky side. Becomes more negative if sanded down to the BOPP film.
Hair, oily skin	+45	+N	Skin is conductive. Cannot be charged by metal rubbing.
Solid polyurethane, filled	+40	+N	Slightly conductive. (8 T ohm cm).
Magnesium fluoride (MgF2)	+35	+N	Anti-reflective optical coating.
Nylon, dry skin	+30	+N	Skin is conductive. Cannot be charged by metal rubbing.
Machine oil	+29	+N	
Nylatron (nylon filled with MoS_2)	+28	+N	
Glass (soda)	+25	+N	Slightly conductive. (Depends on humidity).
Paper (uncoated copy)	+10	-W	Most papers & cardboard have similar affinity. Slightly conductive.
Wood (pine)	+7	-W	
GE brand Silicone II (hardens in air)	+6	+N	More positive than the other silicone chemistry (see below).
Cotton	+5	+N	Slightly conductive. (Depends on humidity).
Nitrile rubber	+3	-W	
Wool	0	-W	
Polycarbonate	-5	-W	
ABS	-5	-N	
Acrylic (polymethyl methacrylate) and adhesive side of clear carton-sealing and office tape	-10	-N	Several clear tape adhesives are have an affinity almost identical to acrylic, even though various compositions are listed.
Epoxy (circuit board)	-32	-N	
Styrene-butadiene rubber (SBR, Buna S)	-35	-N	Sometimes inaccurately called "neoprene" (see below).
Solvent-based spray paints	-38	-N	May vary.
PET (mylar) cloth	-40	-W	
PET (mylar) solid	-40	+W	
EVA rubber for gaskets, filled	-55	-N	Slightly conductive. (10 T ohm cm). Filled rubber will usually conduct.
Gum rubber	-60	-N	Barely conductive. (500 T ohm cm).
Hot melt glue	-62	-N	
Polystyrene	-70	-N	
Polyimide	-70	-N	
Silicones (air harden & thermoset, but *not* GE)	-72	-N	
Vinyl: flexible (clear tubing)	-75	-N	
Carton-sealing tape (BOPP), sanded down	-85	-N	Raw surface is very + (see above), but close to PP when sanded.
Olefins (alkenes): LDPE, HDPE, PP	-90	-N	UHMWPE is below. Against metals, PP is more neg than PE.
Cellulose nitrate	-93	-N	
Office tape backing (vinyl copolymer ?)	-95	-N	
UHMWPE	-95	-N	
Neoprene (polychloroprene, *not* SBR)	-98	-N	Slightly conductive if filled (1.5 T ohm cm).
PVC (rigid vinyl)	-100	-N	
Latex (natural) rubber	-105	-N	
Viton, filled	-117	-N	Slightly conductive. (40 T ohm cm).
Epichlorohydrin rubber, filled	-118	-N	Slightly conductive. (250 G ohm cm).
Santoprene rubber	-120	-N	
Hypalon rubber, filled	-130	-N	Slightly conductive. (30 T ohm cm).
Butyl rubber, filled	-135	-N	Conductive. (900 M ohm cm). Test was done fast.
EDPM rubber, filled	-140	-N	Slightly conductive. (40 T ohm cm).
Teflon	-190	-N	Surface is fluorine atoms-- very electronegative.

(Lee, 2009)

H.2 Triboelectric Series: Part II

Comparison of four published triboelectric series

Ref. [3]	Ref. [4]	Ref. [5]	Ref. [6]
Positive charge			
		Silicone elastomer with silica filler	Air
		Borosilicate glass, fire polished	Human hands
	Wool	Window glass	Asbestos
		Aniline-formol resin	Rabbit fur
		Polyformaldehyde	Glass
		Polymethyl methacrylate	Mica
		Etylcellulose	Human hair
		Polyamide 11	
Nylon 6,6	Nylon	Polyamide 6-6	Nylon
		Rock salt (NaCl)	Wool
		Melanime formol	Fur
		Wool, knitted	Lead
		Silica, fire polished	Silk
	Viscose	Silk, woven	Aluminum
Cellulose		Polyethylene glycol succinate	Paper
Cellulose acetate		Cellulose acetate	
		Polyethylene glycol adipate	
		Polydiallyl phthalate	
		Cellulose (regenerated) sponge	
	Cotton	Cotton, woven	Cotton
		Polyurethane elastomer	Steel
	Silk	Styrene-acrylonitrile copolymer	Wood
		Styrene-butadiene copolymer	Amber
	Acetate	Polystyrene	Sealing wax
Polymethyl methacrylate	Lucite	Polyisobutylene	Hard rubber
Polyacetate	Polyvinyl alcohol	Polyuretane flexible sponge	Nickel, Copper
	Dacron	Borosilicate glass, ground state	Brass, Silver
Polyethylene terephthalate		Polyethylene glycol terephthalate	Gold, Platinum
		Polyvinyl butyral	Sulfur
		Formo-phenolique, hardened	Acetate, Rayon
		Epoxide resin	Polyester
		Polychlorobutadiene	Styrene (Styrofoam)
	Orlon	Butadiene-acrylonitrile copolymer	Orlon
		Natural rubber	Saran
Polyacrylonitrile		Polyacrilonitrile	
Polyvinyl chloride	*Polyvinyl chloride*	Sulfur	

(Diaz and Felix-Navarro, 2004)

H.3 Triboelectric Series: Part III

Reduction of four published triboelectric series for organic polymer

Ref. [3]	Ref. [4]	Ref. [5]	Ref. [6]
Positive charge			
		Aniline-formol resin	
	Wool	Polyformaldehyde	
		Polymethyl methacrylate	
		Ethyl cellulose	
		Polyamide 11	
Nylon 6,6	Nylon	Polyamide 6-6	Nylon
		Melanime formol	
		Wool, knitted	Wool
		Silk, woven	Silk
Cellulose	Viscose	Polyethylene glycol succinate	
Cellulose acetate		Cellulose acetate	Paper
		Polyethylene glycol adipate	
		Polydiallyl phthalate	
		Cellulose (regenerated) sponge	
	Cotton	Cotton, woven	Cotton
		Polyurethane elastomer	
	Silk	Styrene-acrylonitrile copolymer	
		Styrene-butadiene copolymer	
			Wood
			Hard rubber
	Acetate		Acetate, rayon
Polymethyl methacrylate	Lucite		
	Polyvinyl alcohol		
	Dacron		Polyester
		Polystyrene	Styrene (Styrofoam)
		Polyisobutylene	
		Polyuretane flexible sponge	
Polyacetate			
Polyethylene terephthalate		Polyethylene glycol terephthalate	
		Polyvinyl butyral	
		Formo-phenolique, hardened	
		Epoxide resin	
		Polychlorobutadiene	
		Butadiene-acrylonitrile copolymer	
		Natural rubber	
		Polyacrilonitrile	
Polyacrylonitrile			
	Orlon		Orlon
Polyvinyl chloride	*Polyvinyl chloride*		

(Diaz and Felix-Navarro, 2004)

Appendix I

Weblinks: Additional Information

I.1 Black Electrical Insulation Tape

https://no.rs-online.com/web/p/electrical-insulation-tapes/4823346/

I.2 Double-sided Tape

https://www.bauhaus.no/teppetape-avtagbar-25-m-tesa.html

I.3 Snapshot Sequences Through Forest

http://org.ntnu.no/geoteknikk123/Presentations/Videos/Avalanche/
https://labdata.ibm.ntnu.no:7661/sharing/sDdsj1r9j

I.4 Free Tracker Software

http://physlets.org/tracker/help/frameset.html

I.5 Humidifier

https://www.clasohlson.com/no/Luftfukter/36-6480

Bibliography

Bartelt, P., Bühler, Y., Buser, O., Christen, M., and Meier, L. (2012). Modeling mass-dependent flow regime transitions to predict the stopping and depositional behavior of snow avalanches. *Journal of Geophysical Research-Earth Surface 117*, page 28.

Bartelt, P. and Stockli, V. (2001). The influence of tree and branch fracture, overturning and debris entrainment on snow avalanche flow. *Annals of Glaciology, Vol 32, 2001. K. Hutter. Cambridge, Int Glaciological Soc. 32*, pages 209–216.

Bebi, P., Kienast, F., and Schönenberger, W. (2001). Assessing structures in mountain forests as a basis for investigating the forests' dynamics and protective function. *Forest Ecology and Management 145(1-2)*, pages 3–14.

Bebi, P., Kulakowski, D., and Rixen, C. (2009). Snow avalanche disturbances in forest ecosystems—state of research and implications for management. *Forest Ecology and Management 257*, page 1883–1892.

Bovet, E., Chiaia, B., and Frigo, B. (2011). Modelling and testing of avalanche impact on structures. *20th Associazione Italiana di Meccanica Teorica e Applicata Congress (AIMETA)*, page 200–201.

Bozhinskiy, A. and Sukhanov, L. (1998). Physical modelling of avalanches using an aerosol cloud of powder materials. *Annals of Glaciology,26*, page 242–246.

Brang, P. (2001). Resistance and elasticity: promising concepts for the management of protection forests in the european alps. *Forest Ecology and Management 145(1–2)*, pages 107–119.

Brateng, L. E. (2005). Laboratorieforsøk for utforming av terrengtiltak mot snøskred. *Master's Thesis, NTNU*.

Burgo, T. A. L., Galembeck, F., and Pollack, G. H. (2016). Where is water in the triboelectric series? *Journal of Electrostatics 80*, pages 30–33.

Buser, O. and Bartelt, P. (2009). Production and decay of random kinetic energy in granular snow avalanches. *Annals of Glaciology 55(189)*, page 3–12.

Castellanos, A. (2005). The relationship between attractive interparticle forces and bulk behaviour in dry and uncharged fine powders. *Advances in Physics, vol. 54, no. 4*, page 263–276.

Christen, M., Bartelt, P., and Kowalski, J. (2001). Back calculation of the in den arelen avalanche with ramms: interpretation of model results. *Annals of Glaciology 51(54)*, pages 161–168.

Colorado Avalanche Information Center (2016). From: http://avalanche.org/accidents.php, visited on 2016-12-19.

De Campos, M. M. and Ferreira, M. C. (2013). A comparative analysis of the flow properties between two alumina-based dry powders. *Advances in Materials Science and Engineering*.

Diaz, A. and Felix-Navarro, R. M. (2004). A semi-quantitative tribo-electric series for polymeric materials: the influence of chemical structure and properties. *Journal of Electrostatics 62*, pages 277–290.

Drahun, J. A. and Bridgwater, J. (1983). The mechanisms of free surface segregation. *Powder Technology*, 36(1):39–53.

Feistl, T., Bebi, P., Teich, M., Bühler, Y., Christen, M., Thuro, K., and Bartelt, P. (2014). Observations and modeling of the braking effect of forests on small and medium avalanches. *Journal of Glaciology 60(219)*, pages 124–138.

Frehner, M., Schwitter, P., and Wasser, B. (2005). Nachhaltigkeit und erfolgskontrolle im schutzwald. wegleitung für pflegemaßnahmen in wäldern mit schutzfunktion. *Swiss Agency for the Environment, Forests and Landscape (SAEFL) Bern (in German)*.

Gray, J., Tai, Y. C., and Noelle, S. (2003). Shock waves, dead zones and particle-free regions in rapid granular free-surface flows. *Journal of Fluid Mechanics 491*, pages 161–181.

Grof, Z., Lawrence, C. J., and Stepanek, F. (2008). The strength of liquid bridges in random granular materials. *Journal of Colloid and Interface Science 319*, pages 182–192.

Gruber, U. and Bartelt, P. (2007). Snow avalanche hazard modelling of large areas using shallow water numerical methods and gis. *Environ. Model. Softw.*, page 1472–1481.

Hauksson, S., Pagliardi, M., and Barbolini, M. (2007). Laboratory measurements of impact forces of super critical granular flow against mast-like obstacles. *Cold Regions Science and Technology, 49(1)*, page 54–63.

Herminghaus, S. (2005). Dynamics of wet granular matter. *Advances in Physics 54*, pages 221–261.

Hestnes, E. (n.d). From: https://www.ngi.no/eng/News/NGI-News/Extensive-measures-to-stop-avalanches-in-Iceland, visited on 2016-12-23.

Hákonardóttir, K. M. and Jóhannesson, T. (2001). A laboratory study of the retarding effect of breaking mounds in 3, 6 and 9m long chutes. *Technical Report 01007*.

Issler, D. (2003). Experimental information on the dynamics of dry-snow avalanches. *Found in Hutter,K. and N. Kirchner, eds. Dynamic response of granular and porous materials under large and catastrophic deformations*, pages 109–160.

Issler, D. (2004). Méthodologie d'expertise: les calculs des avalanches. *Lecture Notes, Université européenne d'été,* From: http://snf.ngi.no/reports/uee_2004.mod8.040725.pdf.

Iverson, R. M., Logan, M., and Denlinger, R. P. (2004). Granular avalanches across irregular three-dimensional terrain: 2. experimental tests. *Journal of Geophysical Research 109*.

Jan, S. (2010). Avalanche destruction. From: http://www.swissinfo.ch/eng/avalanche-destruction/8022798, visited on 2016-12-19.

Kahrs, K. (2015). The braking effect of trees on snow avalanches, an experimental study: Master's thesis. *NTNU Trondheim*.

Koos, E. (2013). Liquid bridges for solid matter. *Research for Grand Challenges*.

Kudrolli, A. (2008). Granular matter: Sticky sand. From: http://mx1.hydroscoastal.com/images/sticky_sand%20.pdf, visited on 2018-01-14.

Lavoie, F., Cartilier, L., and Thibert, R. (2002). New methods characterizing avalanche behavior to determine powder flow. *Pharmaceutical Research 19,6*, page 887.

Lee, B. (2009). Triboelectric table. *AlphaLab, Inc*.

Leitinger, G., Höller, P., Tasser, E., Walde, J., and Tappeiner, U. (2008). Development and validation of a spatial snow-glide model. *Ecological Modeling 211*, page 363–374.

Manoharan, V. N., Elsesser, M. T., and Pine, D. J. (2003). Dense packing and symmetry in small clusters of microspheres. *Science*, pages 483–487.

Marty, C., Phillips, M., and Lehning, M. (2007). Klimaänderungen und naturgefahren. *Bündner Wald 60 (3)*, pages 35–42.

Matsusaka, S., Maruyama, H., Matsuyama, T., and Ghadiri, M. (2015). Triboelectric charging of powders: A review. *Chemical Engineering Science 65(22)*, pages 5781–5807.

Matsusaka, S. and Masuda, H. (2003). Electrostatics of particles. *Advanced Powder Technology 14*, pages 143–166.

McClung, D. M. and Schweizer, J. (2006). Fracture toughness of dry snow slab avalanches from field title = measurements. *Journal of Geophysical Research-Earth Surface*, page 111(F4).

Mitarai, N. and Nori, F. (2006). Wet granular materials. *Advances in Physics 55*, page 1.

Mohammed, A. S., Abdullah, E. C., Geldart, D., and Raman, A. A. A. (2011). Measuring powder flowability with a modified warren spring cohesion tester. *Particuology 9, 2*, page 148–154.

Moortgat, J. (2016). Viscous and gravitational fingering in multiphase compositional and compressible flow. *Advances in Water Resources*, 89:53–66.

Motta, R. and Haudemand, J. C. (2000). Protective forests and silvicultural stability - an example of planning in the aosta valley. *Mountain Research and Development 20(2)*, pages 180–187.

n.a. (2010). Permanenter technischer Lawinenschutz, Benennungen und Definitionen sowie statische und dynamische Einwirkungen. *ÖNORM-Regel 24805 2010, Vol. 20, in German*.

Naaim, M., Faug, T., and Naaim-Bouvet, F. (2003). Dry granular flow modelling including erosion and deposition. *Surveys in Geophysics 24(5-6)*, pages 569–585.

Naaim, M., Naaim-Bouvet, F., Faug, T., and Bouchet, A. (2004). Dense snow avalanche modeling: flow, erosion, deposition and obstacle effects. *Cold Regions Science and Technology 39(2-3)*, pages 193–204.

National Avalanche Center (n.d.). From: http://www.fsavalanche.org, visited on 2016-12-19.

Newesely, C., Tasser, E., Spadinger, P., and Cernusca, A. (2000). Effects of land-use changes on snow gliding processes in alpine ecosystems. *Basic and Applied Ecology 1*, page 61–67.

Norem, H., Irgens, F., and Schieldrop, B. (1987). A continuum model for calculating snow avalanche velocities. in avalanche formation, movement and effects. *Proceedings of the Davos Symposium, September 1986*, page 363–379.

Paterson, W. (2009). The physics of glaciers. typical densities of snow and ice. From: http://sciencelearn.org.nz/Contexts/Icy-Ecosystems/Looking-closer/Snow-and-ice-density, visited on 2016-10-11.

Pouliquen, O., Delour, J., and Savage, S. B. (1997). Fingering in granular flows. *Nature*, 386(6627):816–817.

Reardon, B. A., Pederson, G., Caruso, C. J., and Fagre, D. B. (2008). Spatial reconstructions and comparisons of historic snow avalanche frequency and extent using tree rings in glacier national park, montana, usa. *Arctic, Antarctic, and Alpine Research 40(1)*, pages 148–160.

Relweger, I. (2005). St.anton avalanche, austria, 1998. From: http://www.baunat.boku.ac.at/en/ian/forschung/fachbereich-lawine/, visited on 2016-11-19.

Rudolf-Miklau, F., Sauermoser, S., and Mears, A. I., editors (2015). *The technical avalanche protection handbook*. Ernst & Sohn a Wiley brand, Berlin.

Sakals, M. E., Innes, J. L., Wilford, D. J., Sidle, R. C., and Grant, G. E. (2006). The role of forests in reducing hydrogeomorphic hazards. In *Forest, snow and landscape research*, volume 80(1), pages 11–22. Haupt, Berne and Stuttgart and Vienna.

SATSIE (2003). Flateyri avalanche, october 1995. From: http://www.leeds.ac.uk/satsie/flateyri.html, visited on 2016-11-15.

Savage, S. B. and Lun, C. K. K. (1988). Particle size segregation in inclined chute flow of dry cohesionless granular solids. *Journal of Fluid Mechanics*, 189(-1):311.

Schaerer, P. and McClung, D. (2006). *The Avalanche Handbook*. Mountaineers Books, Seattle Wash., 3rd ed. edition.

Schild, A. (2006). From: https://commons.wikimedia.org/w/index.php?curid=1022922, visited on 2016-12-20.

Schneebeli, M. and Meyer-Grass, M. (1993). Avalanche starting zones below the timber line—structure of forest. *Proceedings of the International Snow Science Workshop, Breckenridge, Colorado, 4–8 October 1992,*, page 176–181.

Schönenberger, W. and Brang, P. (2004). Silviculture in mountain forests. *Encyclopedia of forest sciences 3*, pages 1085–1094.

Schönenberger, W., Noack, A., and Thee, P. (2005). Effect of timber removal from windthrow slopes on the risk of snow avalanches and rockfall. *Forest Ecology and Management 213(1-3)*, pages 197–208.

Schweder, J. and Shulze, D. (1990). Measurement of flow properties of bulk solids. *Powder Technology 61*, pages 59–68.

Scoville, E. and Peleg, M. (1981). Evaluation of the effect of liquid bridges on the bulk properties of model powers. *Journal of Food Science 46*, page 174–177.

Sovilla, B., Kern, M., and Schaer, M. (2010). Slow drag in wet-snow avalanche flow. *Journal of Glaciology 56(198)*, pages 587–592.

Takeuchi, Y., Torita, H., Nishimura, K., and Hirashima, H. (2011). Study of a large-scale dry slab avalanche and the extent of damage to a cedar forest in the makunosawa valley, myoko, japan. *Annals of Glaciology 52(58)*, pages 119–128.

Teich, M., Bartelt, P., Grêt-Regamey, A., and Bebi, P. (2012). Snow avalanches in forested terrain: Influence of forest parameters, topography, and avalanche characteristics on runout distance. *Arctic Antarctic and Alpine Research 44(4)*, pages 509–519.

Temper, B. (2014). From: https://snowbrains.com/5-new-avalanche-statistics-need-know/, visited on 2018-01-25.

Van Riemsdijk, L. E., Snoeren, J. P. M., Van der Goot, A. J., Boom, R. M., and Hamer, R. J. (2010). Particle size effects in colloidal gelatin particle suspensions. *Journal of Food Engineering 101*, pages 394–401.

Viglietti, D., Letey, S., Motta, R., Maggioni, M., and Freppaz, M. (2010). Snow avalanche release in forest ecosystems: A case study in the aosta valley region (nw-italy). *Cold Regions Science and Technology 64(2)*, pages 167–173.

Wieland, M., Gray, J., and Hutter, K. (1999). Channelized free-surface flow of cohesionless granular avalanches in a chute with sallow lateral curvature. *Journal of Fluid Mechanics, 392*, pages 73–100.

Xu, Q., Orpe, A. V., and Kudrolli, A. (2007). Lubrication effects on the flow of wet granular materials. *Phys. Rev. E 76*.